PHOTODISSOCIATION OF ION–MOLECULE COMPLEXES STUDIED BY

SELECTED-ION VELOCITY MAP IMAGING

by

JONATHON ANDREW MANER

(Under the Direction of Michael A. Duncan)

ABSTRACT

A new time-of-flight mass spectrometer for velocity map imaging studies of the

photodissociation of mass-selected ions has been constructed. The data provide new insights

into the binding energies and photodissociation dynamics of these systems that are not accessible

by other experimental techniques. While velocity map imaging is a well-established technique

for studying the photodissociation of neutral molecules, it has only been applied to the

photochemistry of ionic systems that can be produced by photoionization. However, the velocity

map imaging experiment is ideally suited for our pulsed laser vaporization and electrical

discharge ion sources, and therefore the incorporation of this technique into our time-of-flight

mass spectrometer opens up new opportunities for studying the photodissociation dynamics of a

variety of ionic systems easily produced in our lab.

INDEX WORDS:

Ions, Photodissociation, Time-of-flight Mass Spectrometry,

Photofragment Imaging, Velocity Map Imaging, Ion Imaging

PHOTODISSOCIATION OF ION–MOLECULE COMPLEXES STUDIED BY SELECTED–ION VELOCITY MAP IMAGING

by

JONATHON ANDREW MANER

BS, Davidson College, 2009

MS, The University of North Carolina at Charlotte, 2011

A Dissertation Submitted to the Graduate Faculty of The University of Georgia in Partial

Fulfillment of the Requirements for the Degree

DOCTOR OF PHILOSOPHY

ATHENS, GEORGIA

2017

© 2017

Jonathon Andrew Maner

All Rights Reserved

PHOTODISSOCIATION OF ION–MOLECULE COMPLEXES STUDIED BY SELECTED–ION VELOCITY MAP IMAGING

by

JONATHON ANDREW MANER

Major Professor: Michael A. Duncan

Committee: Gary E. Douberly

Geoffrey D. Smith

Electronic Version Approved:

Suzanne Barbour Dean of the Graduate School The University of Georgia August 2017

DEDICATION

This dissertation was written as a sort of manual for research at App3. With that in mind, this work is dedicated to the future students and post docs of App3, as well as any other researchers and adventitious engineers who have discovered their own appreciation for novel instrumentation in experimental Physical Chemistry.

ACKNOWLEDGEMENTS

First and foremost, I must thank Mike Duncan for taking me into his lab and trusting me with hundreds of thousands of dollars of equipment. I can be quite difficult at times, but you have always had the patience for it. That being said, I also have to thank the rest of the lab. I am proud to graduate from this lab in this department. I also have to thank my friends and family for all of their support.

TABLE OF CONTENTS

	Page
ACKNOWLEDGEMENTS	v
CHAPTER	
1 INTRODUCTION AND LITERATURE REVIEW	1
References	9
2 EXPERIMENTAL APPARATUS AND IMAGE ANALYSIS	18
Selected-Ion Velocity Map Imaging Spectrometer	18
Ion Optics	21
Image Analysis	24
Ion Sources	26
References	31
3 PHOTODISSOCIATION OF THE ARGON DIMER CATION	34
Introduction	34
Experimental	35
Results and Discussion	35
Conclusion	43
References	44
4 PHOTODISSOCIATION OF THE SILVER–BENZENE CATION	48
Introduction	48
Experimental	51

	Results and Discussion	52
	Conclusion	58
	References	58
5	PHOTODISSOCIATION OF THE HYDRONIUM-ARGON CATION	64
	Introduction	64
	Experimental	66
	Results and Discussion	66
	Conclusion	72
	References	73
APPEND	ICES	
A	CHAPTER 3 SUPPORTING INFORMATION	80
В	CHAPTER 4 SUPPORTING INFORMATION	86

CHAPTER 1

INTRODUCTION AND LITERATURE REVIEW

The photodissociation dynamics of gas-phase ions requires a complete knowledge of the internal energy, velocity, and angular distributions of all products. 1-5 To this end, a variety of techniques have been developed to collect this information.⁶⁻⁷ Early examples include product time-of-flight measurements and translational energy spectroscopies. Both of these are mass spectrometry-based techniques that allow the measurement of the velocities of products and therefore their kinetic energies. However, time-of-flight methods must be constructed with the capability for angle-resolved detection in order to recover the angular distribution of products. 8-17 Translational energy spectroscopic techniques typically employ an electrostatic analyzer which must be scanned over a range of kinetic energies to collect the full distribution. 18-26 It is also possible to take advantage of the Doppler effect to obtain velocity and angular distributions. ²⁷⁻²⁹ Using laser induced fluorescence detection, the Doppler shifted frequency profiles of translationally excited fragments can be measured. However, this technique, like time-of-flight, requires measurements at multiple detection angles to build up the full velocity distribution. These shortcomings were addressed with the introduction of ion imaging techniques, the main advantage of which is the ability to measure product velocity and angular distributions simultaneously. In this work, we describe a new velocity map imaging spectrometer for photodissociation experiments on mass-selected ion-molecule complexes, including Ar₂⁺, $Ag(C_6H_6)$, and H_3O^+Ar .

Photofragment imaging techniques are now standard methods for studying the photodissociation of molecules in the gas phase. The angular and velocity distributions of the fragments are used to determine the nature of the electronic transition leading to photodissociation and the kinetic energy released in the decomposition of the parent molecule. Kinetic energy measurements provide insight into the partitioning of excess energy among the various degrees of freedom of the fragments and may also be used to determine dissociation energies. Thus photofragment imaging is a powerful technique for studying photodissociation dynamics, and great effort has been dedicated to its continued development.

Chandler and Houston used a simple two-electrode set up for the first ion imaging experiments, which focused on the photodissociation of CH₃L.³⁵ Jet-cooled CH₃I was dissociated with 266 nm from a Nd:YAG laser in front of the repeller electrode. A second tunable laser was used to ionize the CH₃ fragments via a 2+1 resonance-enhanced multiphoton ionization (REMPI) process, which were then accelerated toward position-sensitive reticon array detector. Eppink and Parker later improved upon this design with the introduction of velocity map imaging (VMI).³⁶ In this variation, grid electrodes were replaced with open electrostatic lenses and an extraction electrode was included to make a three-electrode assembly resembling a Wiley-McLaren configuration. Thus ion transmission is increased, grid aberrations are eliminated, and focusing is improved with the tunable voltage of the extraction electrode. The authors demonstrated the power of this new method with the photodissociation of O₂, imaging both oxygen atoms and their corresponding photoelectrons. The resolution of VMI was further improved using centroiding methods, which employ a computer program to reduce the spot size of an ion event at the detector to one pixel in the recorded image.

Both the VMI methods of Eppink and Parker and the ion imaging methods of Chandler and Houston record the two dimensional projection of a three-dimensional distribution of photofragments. To recover the three-dimensional distribution, it must be mathematically reconstructed from the two-dimensional image. 32,37-38 There are essentially two general approaches to image reconstruction: inversion methods and forward convolution methods. Inversion methods, such as the inverse Abel transform, are used for three-dimensional velocity distribution cylindrically symmetric about an axis parallel to the face of the detector. The twodimensional projection contains all information necessary for the reconstruction of the threedimensional distribution. This includes most photodissociation and bimolecular scattering experiments. Forward convolution methods are used for experiments that do not have an axis of cylindrical symmetry in the lab frame. These include angular momentum polarization studies in which the photolysis and photoionization lasers have perpendicular linear polarizations. In this case the two-dimensional image is simulated and compared with the experimental image. The parameters of the simulation are iteratively optimized for the most accurate reproduction of the experimental data.

Sliced imaging techniques were introduced as an alternative to mathematical reconstruction. These techniques were designed with the goal of imaging only the central "slice" of an expanding photofragment ion cloud, which contains all angular and kinetic energy information. Thus the need for mathematical reconstruction of the fragment ion velocity distribution from its two-dimensional projection and the resulting artificial noise are eliminated. Strategies for sliced imaging fall into two categories: laser-based slicing techniques and time slicing techniques. For laser slicing techniques, the ionizing laser beam is manipulated in some way to ionize and detect slices of the photofragment distribution. Time slicing techniques

essentially rely on pulsed detection of photofragments with broad arrival time distributions. Kinugawa and Arikawa demonstrating laser slicing by combining Doppler spectroscopy with ion imaging.³⁹ By tuning the ionizing laser to the center of the Doppler profile of a photofragment and aligning the laser parallel to the time-of-flight of an imaging spectrometer, photofragments with zero velocity component parallel to the beam were selectively ionized. Thus only fragments with velocities perpendicular to the laser beam, which correspond to the central slice of the distribution, were detected. In another example, Tonokura and Suzuki used a laser pulse with a sheet-like profile to ionize a thin slice of the spherical photofragment distribution so that only this portion was detected.⁴⁰ The main disadvantage of these methods is that the spatial photon density of the laser beam is not uniform, so fragments in different regions of the image will not be detected with uniform efficiency.³⁴ Generally, this leads to more efficient detection of slow ions. Kitsopoulos and coworkers used an alternative approach that was somewhat analogous to the pulse delay extraction technique of Wiley and McLaren. 41-42 By introducing a delay between the photolysis/ionization laser pulses and a pulsed extraction field, the temporal spread of ions arriving at the detector can be tuned. Following photodissociation, fragments are allowed to expand in a field-free region in front of the repeller electrode, which is grounded. The repeller is then switched to high voltage. This technique was initially employed to optimize

spatial resolution in time-of-flight mass spectrometers. However, it can also be used to spoil resolution at the detector, resulting in a broad arrival time distribution on the order of 100s of nanoseconds. Using a narrow gate (less than 90 ns), an MCP detector can be pulsed on to image only the central slice of the expanding photofragment cloud. A disadvantage of this method is that fine mesh grids are required to create the field-free region, which reduce resolution and ion

transmission. The DC-slice imaging variant of Suits avoids the need for grids and pulsed fields.

Instead, an assembly of electrostatic lenses with static voltages is used to extract ions with no temporal delay.⁴³ By introducing extra lenses in addition to the three-electrode configuration typical of VMI experiments, the field between adjacent electrodes can be reduced. This leads to ion cloud stretching along the time-of-flight axis similar to the pulse delay extraction technique, and permits detection with a narrow gate pulse without sacrificing resolution.

These techniques have been employed to study a variety of other dynamic processes in addition to simple photodissociation.³¹⁻³² For example, velocity map imaging has been used for vector correlation studies on fragments of photodissociation events. These experiments typically employ two counter propagating lasers. One laser is used to dissociate the molecule of interest and the second ionizes a photofragment. The fragments are then accelerated toward an imaging detector under VMI conditions. Because the detection efficiency of the photofragments depends on the alignment of angular momentum vector with the electric field vector of the ionizing laser, the correlation between the velocity vector and the angular momentum vector of the fragments can be observed by rotating the polarization of the ionizing laser relative to the polarization of the dissociating beam. Suits and coworkers applied this idea to the photodissociation of O₃ at 248 nm. 44 The authors concluded that excitation leads to the ${}^{1}B_{2} \leftarrow {}^{1}A_{1}$ transition followed by prompt dissociation along the O–O₂ bond axis, producing $O_2(a^1\Delta_g)$. This is consistent with an impulsive model in which rapid dissociation results in a large degree of rotational excitation in the O_2 fragment with the total angular momentum vector, J, perpendicular to the velocity vector, v. Indeed one might expect this for all bent molecules in which fast dissociation along one coordinate produces a torque between fragments. The conception of DC-slice imaging is partially due to interest in vector correlation studies. 43 By using lasers with perpendicular polarizations, the cylindrical symmetry condition necessary for Abel inversion is violated.

However, the DC-slice technique skirts the issue by avoiding the need for image reconstruction (*vide supra*).

Velocity map imaging has also been used to improve the throughput and sensitivity of photoelectron spectroscopy, leading to the development of slow electron velocity map imaging (SEVI). 45-47 SEVI experiments use velocity map imaging detection to collect photoelectron spectra of mass-selected anions at varying detachment energies. Photoelectrons are extracted at low voltage resulting in high resolution spectra that reflect the electronic and vibrational energy levels of the neutral system. Anions are produced by electron attachment in electron impact or laser vaporization sources. As an example, Neumark and coworkers have recently applied this technique to the tert-butyl peroxide radical. 48 They recorded vibrationally resolved spectra of the $X^2A'' \leftarrow X_1A'$ and $A^2A' \leftarrow X^1A'$ electronic bands of the neutral radical, reporting vibrational frequencies previously unobserved in IR experiments and improved sensitivity compared to other anion photoelectron spectroscopy studies. This experiment demonstrates the power and utility of velocity map imaging as a spectroscopic technique in addition to its many applications in chemical dynamics. The groups of Johnson, Wang, and Gerald, to name a few, have all developed instruments with versatile ion sources and mass selection capabilities for anion photoelectron imaging, demonstrating the high level of interest in these methods. 49-51

Photoelectron imaging techniques have also been developed for photoelectron-photoion coincidence imaging (PEPICO) experiments.⁵² These experiments typically employ a VUV source to ionize a neutral molecule. The photoelectron is extracted and imaged and its arrival time marks the start of the flight time of the photoion. This is somewhat unusual for a photoionization mass spectrometry experiment in which typically an ionizing laser pulse signals the start of the flight time. However, this particular aspect of PEPICO permits the use of

continuous light sources. A recent example of this was reported by Baer and coworkers, in which a synchrotron source was used for dissociative ionization of CH_3I .⁵³ The authors derived values for the heat of formation of CH_3I as well as the C–I bond energy, which clarified the results of a previous PEPICO experiment employing pulsed field ionization that was complicated by the presence of $(CH_3I)_n$ species and clusters with buffer gas molecules.

Imaging has also been used to study scattering in crossed beam experiments. Houston and coworkers studied inelastic scattering in crossed beams of Ar and NO, and they derived state-resolved product differential cross-sections and measured product scattering angles. An immediate advantage of this technique is that it does not require a rotatable mass spectrometer, and all scattering angles can be detected simultaneously. Chandler and coworkers employed crossed beam imaging to study reactive scattering in the prototypical reaction $H + D_2$. The groups of Wester and Farrar have developed crossed beam imaging experiments for reactions of mass-selected ions with neutral molecules, thus demonstrating the application of velocity map imaging techniques to the study of proton exchange, charge transfer, and nucleophilic substitution reactions. $^{57-59}$

With the exception of these crossed beam studies of ion-molecule reactions, most photofragment imaging experiments have focused on neutral systems. Although anion photoelectron spectroscopy involves measurements on anionic systems, their purpose is the elucidation of the electronic structure of the neutral species. Studies of ions are far less common and essentially limited to systems for which photoionization methods are efficient. This is surprising, considering the variety of imaging experiments that have been developed. A more general approach to photodissocation dynamics in ionic systems would be a photofragment imaging experiment incorporating an efficient ion source, and this goal has been pursued by just

a few labs to date. Lepère and coworkers designed an imaging apparatus with an electron impact source for photodissociation of mass-selected ions and simultaneous imaging of neutral and ionic fragments. 66 This instrument employs rudimentary ion imaging techniques with no optics for focusing ions. Instead the beam of ionic fragments is bent away from the time-of-flight axis with an electrostatic analyzer towards one detector while the neutral fragment beam is transmitted along the time-of-axis to another detector. Because the ionic fragments are not accelerated, the images are directly comparable. This is therefore a low resolution instrument by design. Misaizu's group has designed two higher resolution apparatuses for photodissociation massselected ions, both incorporating laser vaporization sources for generating metal-containing ions. The first design is based on a reflectron time-of-flight mass spectrometer where the reflectron grids are replaced with open ring electrodes. 67-69 Ions are dissociated before entering the reflectron. Fragments are focused as they exit, because the field is not confined in the reflectron by a grid. The second design incorporates another reflectron to improve mass resolution. ⁷⁰ The lab of Stuart Mackenzie has also constructed an imaging spectrometer worth mentioning here. This instrument uses VMI techniques for the study of small neutral metal-containing systems. Although REMPI detection is still required, this instrument effectively demonstrates the coupling of a VMI spectrometer to a laser vaporization source, and in some cases they are able to infer properties of ionic systems from the data. 71-74 Mass-selection is achieved by pulsing the imaging detector to overlap with the arrival time of the desired ion. Our lab has designed and constructed a new time-of-flight mass spectrometer for photodissociation and velocity map imaging studies on mass-selected ions. This instrument incorporates laser vaporization and pulsed electrical discharge sources for the production of a broad range of ions and ion-molecule complexes, and thus we can expand the field of photofragment imaging to ionic systems that cannot be generated

with photoionization methods. The following chapters describe our new apparatus for selectedion velocity map imaging and its application to the photodissociation of ${\rm Ar_2}^+$, and the ion-molecule complexes ${\rm Ag}^+({\rm C_6H_6})$ and ${\rm H_3O}^+{\rm Ar}$.

References

- Ashfold, M. N. R.; Baggott, J. E. Molecular Photodissociation Dynamics; Royal Society of Chemistry, London, UK.
- 2. Schinke, R. *Photodissociation Dynamics*; Cambridge University Press, Cambridge, UK 1993.
- 3. Bowers, M. T. Gas Phase Ion Chemistry; Academic Press, Inc., Orlando, FL, USA 1984.
- 4. Lee, Y. P. "State-resolved dynamics of photofragmentation," *Annu. Rev. Phys. Chem.* **2003**, *54*, 215-244.
- Baer, T.; Hase, W. L. *Unimolecular Reaction Dynamics*; Oxford University Press, New York, USA 1996.
- Ervin, K. M. "Experimental techniques in gas-phase ion thermochemistry," *Chem. Rev.* 2001, 101, 391-444.
- 7. Laskin, J.; Lifshitz, C. "Kinetic energy release distributions in mass spectrometry," *J. Mass Spectrom.* **2001**, *36*, 459-478.
- 8. Lee, Y. T.; McDonald, J. D.; LeBreton, P. R.; Herschbach, D. R. "Molecular beam reactive scattering apparatus with electron bombardment detector," *Rev. Sci. Instrum.* **1969**, *40*, 1402-1408.
- 9. Lee, Y. T. "Molecular beam studies of elementary chemical processes," *Science* **1987**, 236, 793-798.

- 10. Yang, X.; Lin, J.; Lee, Y. T.; Blank, D. A.; Suits, A. G.; Wodtke, A. M. "Universal crossed molecular beams apparatus with synchrotron photoionization mass spectrometric product detection," *Rev. Sci. Instrum.* **1997**, *68*, 3317-3326.
- 11. Lin, J. J.; Hwang, D. W.; Harich, S.; Lee, Y. T.; Yang, X. "New low background crossed molecular beam apparatus: Low background detection of H₂," *Rev. Sci. Instrum.* **1998**, 69, 1642-1646.
- Busch, G. E.; Cornelius, J. F.; Mahoney, R. T.; Morse, R. I.; Schlosser, D. W.; Wilson,
 K. R. "Photofragment spectrometer," *Rev. Sci. Instrum.* 1970, 41, 1066-1073.
- 13. Busch, G. E.; Wilson, K. R. "Triatomic photofragment spectra. I. Energy partitioning in NO₂ photodissociation," *J. Chem. Phys.* **1972**, *56*, 3626-3628.
- 14. Busch, G. E.; Wilson, K. R. "Triatomic photofragment spectra. II. Angular distribution from NO₂ photodissociation," *J. Chem. Phys.* **1972**, *56*, 3628-3654.
- 15. Van Deen, G. N. A.; Mohamed, K. A.; Baller, T.; de Vries, A. E. "Photofragmentation of HI in the first continuum," *Chem. Phys.* **1983**, *80*, 113-120.
- 16. Hall, G. E.; Sivakumar, N.; Ogorzalek, R.; Chawla, G.; Haerri, H.-P.; Houston, P. L.; Burak, I.; Hepburn, J. W. "Product correlations in photofragment dynamics," *Disc. Farad. Soc.* 1986, 82, 13-24.
- 17. Ogorzalek, R.; Hall, G. E.; Härri, H.-P.; Houston, P. L. "State-resolved photofragment velocity distributions by pulsed extraction time-of-flight mass spectrometry," *J. Phys. Chem.* **1988**, *92*, 5-8.
- 18. Cooks, R. G.; Beynon, J. H.; Caprioli, R. M.; Lester, G. R. *Metastable Ions*; Elsevier, Amsterdam, NL 1973.

- 19. Huber, B. A.; Miller, T. M.; Cosby, P. C.; Zeman, H. O.; Leon, R. L.; Moseley, J. T.; Peterson, J. R. "Laser–ion coaxial beams spectrometer," *Rev. Sci. Instrum.* **1977**, *48*, 1306-1313.
- 20. Lifshitz, C.; Tzidony, E. "Kinetic energy release distributions for C₃H₆O^{+•} ion dissociations: A further test of the applicability of the energy-randomization hypothesis to unimolecular fragmentations," *Int. J. Mass Spectrom. Ion Phys.* **1981**, *39*, 181-195.
- 21. Illies, A. J.; Jarrold, M. F.; Wagner-Redeker, W.; Bowers, M. T. "Photoinduced intramolecular charge transfer: Photodissociation of CO₂⁺·Ar cluster ions," *J. Am. Chem. Soc.* **1985**, *107*, 2842-2849.
- 22. Kim, H.-S.; Kuo, C.-H.; Bowers, M. T. "Photon driven charge transfer half-collisions: The photodissociation of CO₂·O₂⁺ cluster ions with resolution of the O₂ product vibrational states," *J. Chem. Phys.* **1987**, 87, 2667-2676.
- 23. Snodgrass, J. T.; Dunbar, R. C.; Bowers, M. T. "Photodissociation of the benzene dimer cation in the gas phase," *J. Phys. Chem.* **1990**, *94*, 3648-3651.
- 24. Graul, S. T.; Kim, H.-S.; Bowers, M. T. "The dynamics of photodissociation of the gas phase (N₂O·H₂O)⁺ cluster ion," *Int. J. Mass. Spectrom.* **1992**, *117*, 507-536.
- Brenton, A. G. "Translational Energy Spectroscopy," J. Mass Spectrom. 1995, 30, 657-665.
- Brenton, A. G. "Translational-energy spectroscopy: A personal perspective of its development," *Int. J. Mass Spectrom.* 2000, 200, 403-422.
- 27. Schmiedl, R.; Dugan, H.; Meier, W.; Welge, K. H. "Laser Doppler spectroscopy of atomic hydrogen in the photodissociation of HI," *Z. Phys.* **1982**, *A304*, 137-142.

- 28. Nadler, I.; Mahgerefteh, D.; Reisler, H.; Wittig, C. "The 266 nm photolysis of ICN: Recoil velocity anisotropies and nascent E,V,R,T excitations for the CN + $I(^2P_{3/2})$ and CN + $I(^2P_{1/2})$ channels," *J. Chem. Phys.* **1985**, 82, 3885-3893.
- 29. Houston, P. L. "Vector correlations in photodissociation dynamics," *J. Phys. Chem.* **1987**, *91*, 5388-5397.
- 30. Heck, A. J. R.; Chandler, D. W. "Imaging techniques for the study of chemical reaction dynamics," *Annu. Rev. Phys. Chem.* **1995**, *46*, 335-372.
- 31. Suits, A. G.; Continetti, R. E. *Imaging in Chemical Dynamics*; American Chemical Society, Washington D. C., USA 2001.
- 32. Whitaker, B. *Imaging in Molecular Dynamics: Technology and Applications*, Cambridge University Press, Cambridge, UK, 2003.
- 33. Ashfold, M. N. R.; Nahler, N. H.; Orr-Ewing, A. J.; Vieuxmaire, O. P. J.; Toomes, R. L.; Kitsopoulos, T. N.; Garcia, I. A.; Chestakov, D. A.; Wu, S.-M.; Parker, D. H. "Imaging the dynamics of gas phase reactions," *Phys. Chem. Chem. Phys.* **2006**, *8*, 26-53.
- 34. Chandler, D. W.; Houston, P. L.; Parker, D. H. "Perspective: Advanced particle imaging," *J. Chem. Phys.* **2017**, *147*, 013601.
- 35. Chandler, D. W.; Houston, P. L. "Two-dimensional imaging of state-selected photodissociation products detected by multiphoton ionization," *J. Chem. Phys.* **1987**, 82, 1445-1447.
- 36. Eppink, A. T. J. B.; Parker, D. H. "Velocity map imaging of ions and electrons using electrostatic lenses: Application in photoelectron and photofragment ion imaging of molecular oxygen," *Rev. Sci. Instrum.* **1997**, *68*, 3477-3484.

- Castleman, K. R. *Digital Image Processing*; Prentice-Hall, Englewood Cliffs, NJ, USA 1979.
- 38. Renth, F.; Riedel, J.; Temps, F. "Inversion of velocity map ion images using iterative regularization and cross validation," *Rev. Sci. Instrum.* **2006**, *77*, 033103.
- 39. Kinugawa, T.; Arikawa, T. "Three-dimensional velocity analysis combining ion imaging with Doppler spectroscopy: Application to photodissociation of HBr at 243 nm," *J. Chem. Phys.* **1992**, *96*, 4801-4804.
- 40. Tonokura, K.; Suzuki, T. "Slicing photofragment spatial distribution by laser sheet ionization," *Chem. Phys. Lett.* **1994**, 224, 1-6.
- 41. Gebhardt, C. R.; Rakitzis, T. P.; Samartzis, P. C.; Ladopoulos, V.; Kitsopoulos, T. N. "Slice imaging: A new approach to ion imaging and velocity mapping," *Rev. Sci. Instrum.* **2001**, *72*, 3848-3853.
- 42. Wiley, W. C.; McLaren, I. H. "Time-of-flight mass spectrometer with improved resolution," *Rev. Sci. Instrum.* **1955**, *26*, 1150-1157.
- 43. Townsend, D.; Minitti, M. P.; Suits, A. G. "Direct current slice imaging," *Rev. Sci. Instrum.* **2003**, *74*, 2530-2539.
- 44. Suits, A. G.; Miller, R. L.; Bontuyan, L. S.; Houston, P. L. "Photofragment vector correlations by ion imaging: O₂ [a $^{1}\Delta_{g}(v,J)$] from 248 nm dissociation of ozone," *J. Chem. Soc., Faraday Trans.* **1993**, 89, 1443-1447.
- 45. Neumark, D. M. "Slow electron velocity-map imaging of negative ions: application to spectroscopy and dynamics," *J. Phys. Chem. A* **2008**, *112*, 13287-13301.

- 46. Osterwalder, A.; Nee, M. J.; Zhou, J.; Neumark, D. M. "High resolution photodetachment spectroscopy of negative ions via slow photoelectron imaging," *J. Chem. Phys.* **2004**, *121*, 6317-6322.
- 47. Hock, C.; Kim, J. B.; Weichmann, M. L.; Yacovitch, T. I.; Neumark, D. M. "Slow photoelectron velocity-map imaging spectroscopy of cold negative ions," *J. Chem. Phys.* **2012**, *137*, 244201(1-6).
- 48. DeVine, J. A.; Weichman, M. L.; Babin, M. C.; Neumark, D. M. "Slow photoelectron velocity-map imaging of cold *tert*-butyl peroxide," *J. Chem. Phys.* **2017**, *147*, 013915.
- 49. Gerardi, H. K.; DeBlase, A. F.; Leavitt, C. M.; Su, X.; Jordan, K. D.; McCoy, A. B.; Johnson, M. A. "Structural characterization of electron-induced proton transfer in the formic acid dimer anion, (HCOOH)₂, with vibrational and photoelectron spectroscopies," *J. Chem. Phys.* **2012**, *136*, 134318.
- 50. León, I.; Yang, Z.; Liu, H.-T.; Wang, L.-S. "The design and construction of a high-resolution velocity-map imaging apparatus for photoelectron spectroscopy studies of size-selected clusters," *Rev. Sci. Instrum.* **2014**, *85*, 083106.
- 51. Patros, K. M.; Mann, J. E.; Jarrold, C. C. "Photoelectron Imaging Spectra of O₂-VOC and O₄-VOC Complexes," *J. Phys. Chem. A* **2016**, *120*, 7828-7838.
- 52. Continetti, R. E. "Coincidence spectroscopy," Annu. Rev. Phys. Chem. 2001, 52, 165-192.
- 53. Bodi, A.; Shuman, N. S.; Baer, T. "On the ionization and dissociative photoionization of iodomethane: a definitive experimental enthalpy of formation of CH₃I," *Phys. Chem. Chem. Phys.* **2009**, *11*, 11013-11021.

- 54. Suits, A. G.; Bontuyan, L. S.; Houston, P. L.; Whitaker, B. J. "Differential cross sections for state-selected products by direct imaging: Ar+NO," *J. Chem. Phys.* **1992**, *96*, 8618-8620.
- 55. Lorenz, K. T.; Chandler, D. W.; Barr, J. W.; Chen, W.; Barnes, G. L.; Cline, J. I. "Direct measurement of the preferred sense of NO rotation after collision with argon," *Science* **2001**, *293*, 2063-2066.
- 56. Kitsopoulos, T. N.; Buntine, M. A.; Baldwin, D. P.; Zare, R. N.; Chandler, D. W. "Reaction product imaging: The H + D₂ reaction," *Science* **1993**, *260*, 1605-1610.
- 57. Wester, R. "Velocity map imaging of ion-molecule reactions," *Phys. Chem. Chem. Phys.* **2014**, *16*, 396-405.
- 58. Meyer, J.; Wester, R. "Ion-molecule reaction dynamics," *Annu. Rev. Phys. Chem.* **2017**, 68, 333-353.
- 59. Pei, L; Farrar, J. M. "Imaging ion–molecule reactions: Charge transfer and halide transfer reactions of O⁺ with CH₃Cl, CH₃Br, and CH₃I," *Int. J. Mass Spectrom.* **2015**, *377*, 93-100.
- 60. Beckert, M.; Greaves, S. J.; Ashfold, M. N. R. "High resolution ion imaging studies of the photodissociation of the Br₂⁺ cation," *Phys. Chem. Chem. Phys.* **2003**, *5*, 308-315.
- 61. Vieuxmaire, O. P. J.; Nix, M. G. D.; Fitzpatrick, J. A. J.; Beckert, M.; Dixon, R. N.; Ashfold, M. N. R. "Predissociation of state selected Br₂⁺ cations," *Phys. Chem. Chem. Phys.* **2004**, *6*, 543-554.
- 62. Sage, A. G.; Oliver, T. A. A.; Dixon, R. N.; Ashfold, M. N. R. "Velocity map imaging studies of the photodissociation of H₂O⁺ cations," *Mol. Phys.* **2010**, *108*, 945-955.

- 63. Kim, M. H.; Leskiw, B. D.; Suits, A. G. "Vibrationally mediated photodissociation of ethylene cation by reflectron multimass velocity map imaging," *J. Phys. Chem. A* **2005**, *109*, 7839-7842.
- 64. Kim, M. H.; Leskiw, B. D.; Suits, A. G. "Vibrationally mediated photodissociation of $C_2H_4^+$," *J. Phys. Chem. A* **2007**, *111*, 7472-7480.
- 65. Gichuchi, W. K.; Mebel, A. M.; Suits, A. G. "UV Photodissociation of ethylamine cation: A combined experimental and theoretical investigation," *J. Phys. Chem. A* **2010**, *114*, 13296-13302.
- 66. Lepère, V.; Picard, Y. J.; Barat, M.; Fayeton, J. A.; Lucas, B.; Bèroff, K.
 "Photodissociation dynamics of Ar₂⁺ and Ar₃⁺ excited by 527 nm photons, *J. Chem. Phys.*2009, 130, 194301.
- 67. Hoshino, H.; Yamakita, Y.; Okutsu, K.; Suzuki, Y.; Saito, M.; Koyasu, K.; Ohshimo, K.; Misaizu, F. "Photofragment imaging of mass-selected ions using a reflectron mass spectrometer I. Development of an apparatus and application to Mg⁺-Ar complex," *J. Chem. Phys.* **2015**, *630*, 111-115.
- 68. Okutsu, K.; Ohshimo, K.; Hoshino, H.; Koyasu, K.; Misaizu, F. " Photofragment imaging of mass-selected ions using a reflectron mass spectrometer. II: Formation mechanism of MgF⁺ in the photodissociation of Mg⁺–FCH₃ complex," *Chem. Phys. Lett.* **2015**, *630*, 57-61.
- 69. Okutsu, K.; Yamazaki, K.; Ohshimo, K.; Misaizu, F. "Photofragment ion imaging from mass-selected Mg⁺BrCH₃ complex: Dissociation mechanism following photoinduced charge transfer," *J. Chem. Phys.* **2017**, *146*, 024301.

- 70. Okutsu, K.; Nakashima, Y.; Yamazaki, K.; Fujimoto, K.; Nakano, M.; Ohshimo, K.; Misaizu, F. "Development of a linear-type double reflectron for focused imaging of photofragment ions from mass-selected complex ions," *Rev. Sci. Instrum.* 2017, 88, 053105.
- 71. Hopkins, W. S.; Hamilton, S. M.; McNaughter, P. D.; Mackenzie, S. R. "VUV photodissociation dynamics of diatomic gold, Au₂: A velocity map imaging study at 157 nm," *Chem. Phys. Lett.* 2009, 483, 10-15.
- 72. Parry, I. S.; Hermes, A. C.; Kartouzian, A.; Mackenzie, S. R. "Imaging the photodissociation of neutral metal clusters: copper dimer, Cu₂, and copper oxide, CuO," *Phys. Chem. Chem. Phys.* **2014**, *16*, 458-466.
- 73. Cooper, G. A.; Kartouzian, A.; Gentleman, A. S.; Iskra, A.; van Wijk, R.; Mackenzie, S.
 R. "Dissociation energies of Ag-RG (RG = Ar, Kr, Xe) and AgO molecules from velocity map imaging studies," *J. Chem. Phys.* 2015, *143*, 124302.
- 74. Cooper, G. A.; Gentleman, A. S.; Iskra, A.; Mackenzie, S. R. "Photofragmentation dynamics and dissociation energies of MoO and CrO," *J. Chem. Phys.* **2017**, *147*, 013921.

CHAPTER 2

EXPERIMENTAL APPARATUS AND IMAGE ANALYSIS

Selected-Ion Velocity Map Imaging Spectrometer

A schematic of the selected-ion velocity map imaging apparatus is shown in Figure 1. This instrument was designed as a modification to a pre-existing reflectron time-of-flight mass spectrometer, the details of which have been described previously. I lons produced by either laser vaporization or pulsed electrical discharge in a supersonic expansion are skimmed into a differentially pump chamber, where they are pulse extracted into a Wiley-McLaren time-of-flight mass spectrometer. The ions travel through a field-free region before entering a reflectron where they are reflected back towards an electron multiplier detector. Ions are selected using a mass gate consisting of two parallel plates. High voltage is applied to one plate while the other is held at ground, which results in deflection of all ions. The high voltage is switched to ground with a complement pulse generator (DEI PVM-4210) for 1-3 µs to transmit the desired ion undeflected. Mass-selected ions are dissociated in the turning region of the reflectron, and mass analysis of parent and fragment ions occurs as they are reaccelerated toward the electron multiplier. Stanford DG535 and BNC 8010 pulse generators are used for synchronization of all pulsed components and the experiment runs at a repetition rate of 10 Hz, set by the typical repetition rate of a Nd:YAG laser. This is the standard mode of operation for simple photodissociation experiments and optimization of ion source conditions.

For imaging experiments, the reflectron is grounded and ions are transmitted into the VMI system in line with the first tube of the time-of-flight mass spectrometer. Here, ions are

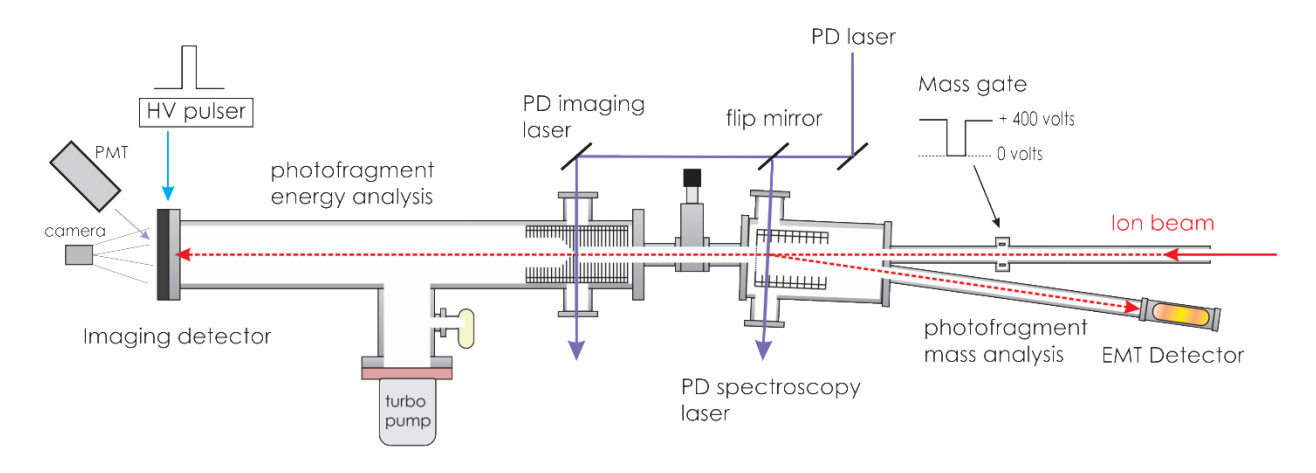


Figure 1. Apparatus for selected-ion velocity map imaging experiments.

decelerated with a field created by a series of electrostatic lenses and a voltage divider.

Decelerated ions are then dissociated with the second or third harmonic of a Nd:YAG laser

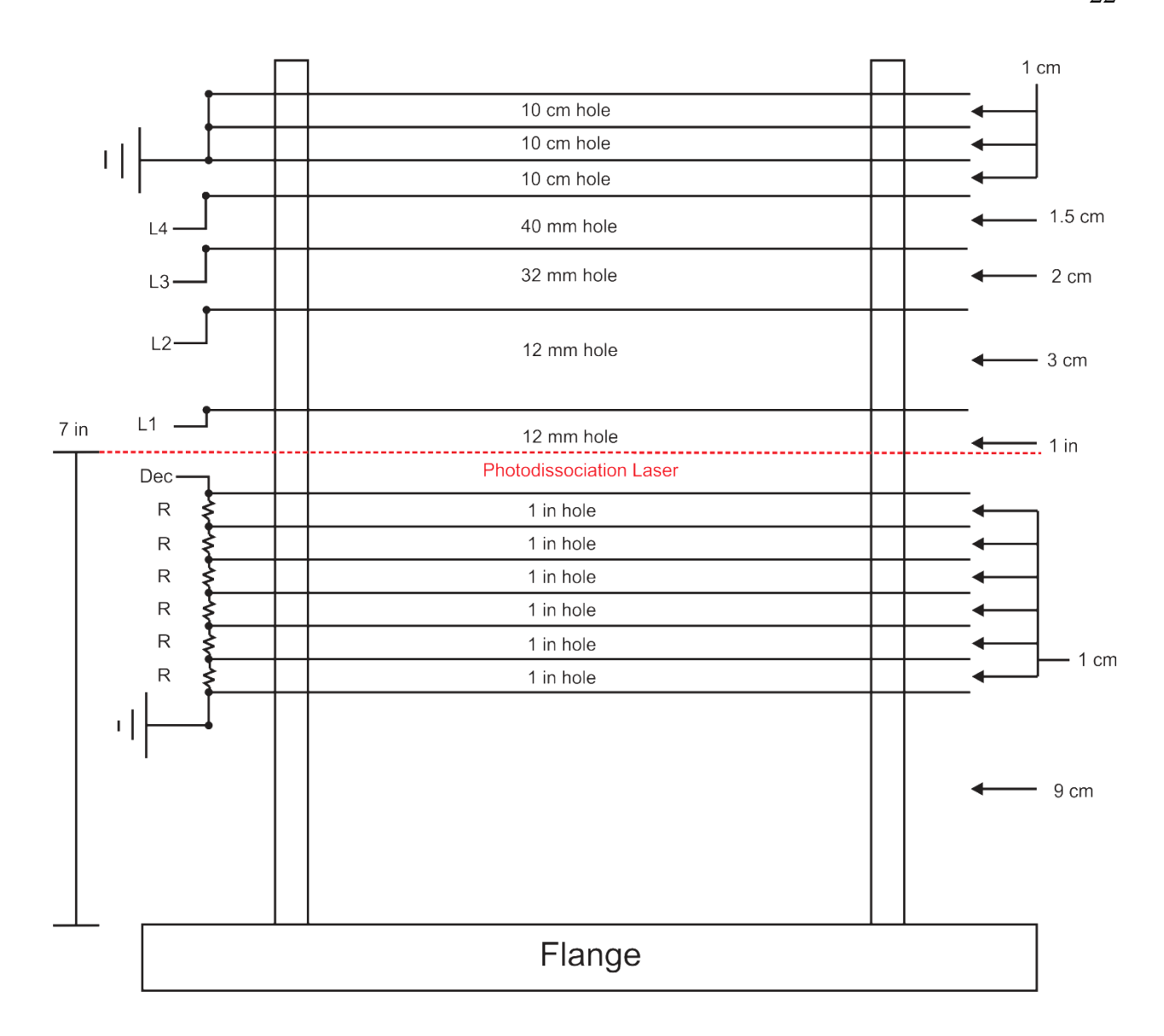
(Continuum SureLite SL-10) or an infrared optical parametric oscillator/optical parametric amplifier system (LaserVision OPO/OPA pumped by Continuum Precision 8010). Fragment and parent ions are reaccelerated into a second field-free region with an assembly of lenses configured for velocity map imaging. This second field-free region was made 1 meter long to increase flight times and energy resolution.

Ions are focused onto a dual MCP/phosphor screen detector (Beam Imaging Solutions BOS-75) at the end of the second flight tube. The detector consists of two chevron microchannel plates and a P47 phosphor screen. The back MCP is gold coated to improve electrical conduction for pulsed operation. The detector may be operated in DC mode, but must be pulsed for DC-slice imaging. The front of the detector is grounded to maintain the field-free conditions of the flight tube. In DC mode, the middle and back electrodes are biased to 1000 V and 2000 V respectively. For sliced imaging experiments, the middle is biased to 1000 V and the back is floated at 1000V. To detect ions, the back plate is pulsed from 1000V to 2000V using a commercial high voltage pulse generator (DEI PVX-4140) and a gate of 140-200 ns.² As a result of the characteristic finite rise and fall times of the MCP detector, a gate of 140 ns leads to an effective on time for the detector of 60 ns. The fluorescence of the phosphor is monitored with a photomultiplier tube and a digital oscilloscope (Lecroy LT342), and mass spectra are acquired using the RedScan software. The P20 phosphor was chosen, because it has a very short fluorescence liftetime of 50 ns. This is similar to the width of an ion arrival time distribution, and so it is possible to record mass spectra with resolution of 1-2 m/z. Images are collected with a CCD camera (Edmund Optics) and the NuAcq acquisition software provided by the Suits

group.³ NuAcq includes a centroiding feature and no additional program is necessary for this process. Images are collected over several hundred thousand laser shots with a repetition rate of 10 Hz.

Ion Optics

A schematic of the VMI electrodes is shown in Figure 2. This design was adapted from Suits' electrode configuration for DC-slice imaging to incorporate a decelerating field prior to the accelerating field created by the VMI lenses.² For ions accelerated to 2500 V in the time-offlight mass spectrometer, the last decelerating electrode is set to 900 V. A potential gradient is created by dividing this voltage over seven lenses. The first lens, L1, is set to 805 V, L2 is 750 V, L3 700 V, and L4 is grounded. The last three lenses provide a ground shield against any stray voltages in this region of the experiment. A SIMION simulation of the photodissociation of Ar₂⁺ at 355 nm shown in Figure 3.4-5 Parent ions with 80 m/z and 2500 V are decelerated as they enter the first stack of lenses. They are then reaccelerated by the field created by the next stack of lenses. A cylindrical distribution of fragment ions with the 40 m/z and the same velocity as the parent ions is created at the center of the dissociation region between the last decelerating lens and L1. A cylindrical distribution was chosen for two reasons. First, the unfocused dissociating laser will irradiate a cylindrical volume of the ion packet. Second, ions leaving the source chamber pass through a 3 mm skimmer. The aperture of the extraction and ground electrodes of the time-of-flight mass spectrometer is 1 in². The extracted ion packet therefore has a cylindrical shape, although it may be distorted by space-charge effects. These ions are also given a kinetic energy of 1 eV in the y direction perpendicular to the flight path, consistent with dissociation at 355 nm. ⁵ The simulation shows that a cylindrical distribution of fragment ions 10 mm long focused to a 5 mm spot at the end of the flight tube.



R = 2 x 200 kΩ Total R = 2.4 MΩ

Figure 2. Ion optics assembly.

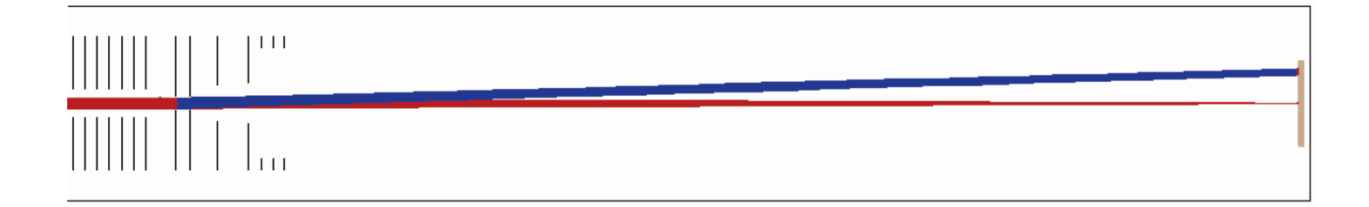


Figure 3. SIMION simulation of Ar_2^+ photodissociation (Red: parent ion beam; Blue: fragment ion beam).

Image Analysis

Image processing including false color, contrast, scaling, addition and subtraction is done with ImageJ(NIH).⁶ Images may be "re-symmetrized" by summing over the horizontal and vertical reflections of the original image.⁷ For analysis of sliced images we use the Finite Slice Analysis program provided by Suits.⁸ Unsliced images are reconstructed with the BASEX program developed by the Reisler group and analyzed in either BASEX or BasisFit, a MatLab based code developed by the Suits group.⁹⁻¹¹ These programs provide integrated angular distributions. They also generate the velocity and kinetic energy distributions, but a velocity calibration factor must be provided. Alternatively, ion velocities can be determined by measuring the radius of the image and the flight time of the ion.

The velocity is related to the kinetic energy by Equation 1, where m and v are the mass and velocity of the ionic fragment.

$$KE = \frac{1}{2}mv^2 \tag{1}$$

The following reaction describes the photodissociation of the ion AB⁺.

$$AB^+ + hv \rightarrow A^+ + B + TKE$$

Here, AB^+ dissociates into A^+ and B with an excess energy of TKE, the total kinetic energy. Assuming that A^+ and B are monoatomic fragments having no electronic excited states with energies less than TKE, this excess energy must go into translation of A^+ and B. The velocity and kinetic energy of A^+ can be measured directly from the image of A^+ using the apparatus described above. Conservation of energy and momentum requires that TKE is the sum of the kinetic energy of A^+ , $KE(A^+)$, and the kinetic energy of B, KE(B) (Equation 2).

$$TKE = KE(A^{+}) + KE(B) \tag{2}$$

 $KE(A^+)$ and KE(B) are related by the following two expressions derived from substitution of Equation 1 into Equation 2:

$$KE(A^{+}) = \left(\frac{m_A}{m_{AB}}\right) TKE \tag{3}$$

$$KE(B) = \left(\frac{m_B}{m_{AB}}\right) TKE \tag{4}$$

Here m_A , m_B , and m_{AB} are the masses of A^+ , B, and AB^+ respectively. From Equations 3 and 4, it is clear that TKE could be determined by measuring $KE(A^+)$ or KE(B), but only $KE(A^+)$, the kinetic energy of the charged particle, is typically measured.

Images also provide angular distributions of photofragments in addition to velocity and kinetic energy distributions. The theory of angular distributions of photofragments has been studied extensively, both from classical and quantum mechanical perspectives. For a one-color photodissociation experiment involving one electronic excited state, the photofragment distribution is given by Equation 5.

$$I = \frac{1}{4\pi} \left[1 + \beta P_2(\cos \theta) \right] \tag{5}$$

I is the ion intensity, $P_2(\cos\theta)$ is the second order Legendre polynomial, and θ is the angle between the electric field vector of the linearly polarized laser and the velocity vector of the ionic fragment. β , the anisotropy parameter, falls between -1 and 2, which corresponds to perpendicular and parallel transitions respectively. Under typical experiment conditions, the electric field vector of the photolysis laser is vertically aligned in the lab frame, parallel to the face of the detector. An ion dissociating via a parallel transition will lead to an image that is peaked at top and bottom, or 0° and 180° , and have $\beta \approx 2$. For perpendicular transitions leading to dissociation, the image will be peaked to the left and right, or 90° and 270° , and have $\beta \approx -1$.

Two more parameters must be introduced to fit the integrated angular distributions provided by the programs mentioned above.

$$I = \frac{A}{4\pi} \left\{ 1 + \frac{\beta}{2} [3\cos^2(\theta - C)] \right\}$$
 (5)

The A parameter allows the amplitude of the equation to change. C takes into account the rotation of an image in the plane of the detector, and therefore corrects, to some extent, for the misalignment of the laser. $P_2(\cos\theta)$ has also been substituted into Equation 5 to provide the exact expression used for fitting the angular distribution data. All data fitting is performed in Origin 8.6.¹⁸

Ion Sources

Laser Vaporization Source

The laser vaporization cluster source has been thoroughly reviewed. ¹⁹ This source generates atomic clusters and ion-molecule complexes in the gas phase, particularly systems that contain metal atoms. A schematic of a laser vaporization source is shown in Figure 4. This is the "offset" configuration of the source, which is designed to promote the formation of ion-molecule complexes. For other source configurations, the interested reader should consult reference 19. A Nd:YAG laser (Spectra Physics INDI) is used to generate 532 nm or 355 nm light. The beam is aligned to strike a rotating and translating metal rod in front of a pulsed nozzle (Parker General Valve Series 9, Parker Iota One Pulse Driver) and focused to a 1 mm spot with a CaF₂ lens. Laser power is attenuated using beam splitters and an adjustable aperture. Ions are entrained in a supersonic expansion and cooled by collisions with the buffer gas. The cooling provided by the expansion can promote condensation reactions between metal atoms and ions and clustering of metal ions with buffer gas atoms. Volatile molecules can be entrained in the buffer gas expansion to generate ion-molecule complexes as well. In some cases, these molecules are ionized in the plasma generated by the laser spark at the surface of the rod. ^{5,20}

Laser power is the most important variable for optimizing the laser vaporization source, although no experimental parameter can be neglected. For metal clusters typical pulse energies are 5-20 mJ/pulse, and vary significantly for different metals. This has been attributed to the variation in absorbance and reflectivity of the metal and the plasma dynamics characteristic of the metal-buffer gas system. For metal ion-molecule complexes and nonmetal systems, the beam is attenuated to 1-5 mJ/pulse. Generally, the laser power must be optimized for every system, while also iteratively optimizing buffer gas pressure, composition, and pulse duration.

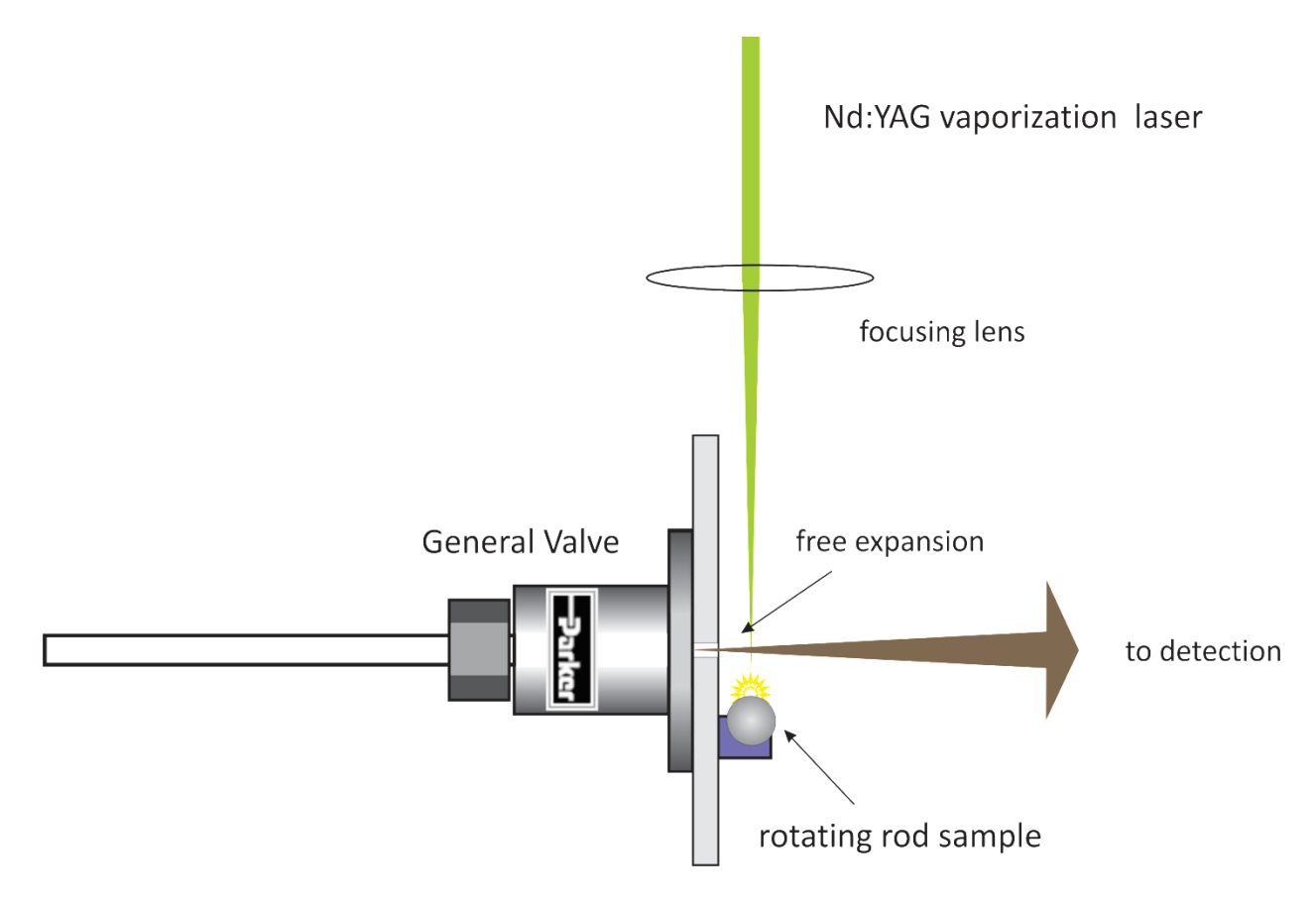


Figure 4. Schematic of the laser vaporization source.

Pulsed Electrical Discharge Source

A pulsed electrical discharge source is used to generate nonmetal ions in the gas phase. This source is ideal for ions that can be produced from volatile precursors. A schematic of the pulsed electrical discharge source is shown in Figure 5. Two sewing needles are mounted 1 mm apart in front of a supersonic expansion provided by a pulsed nozzle (Parker General Valve Series 9, Parker Iota One Pulse Driver). One needle is connected to the output of a high voltage pulser (DEI PVX-4140), and the other is grounded. A high voltage negative pulse, typically 500-1500 V and 5-25 μs wide, is applied to the needle timed in the center of the gas pulse, resulting in electrical discharge through the expanding gas. Typical gas pulse widths are 200-350 μs in duration and backing pressures may be 80-200 psi. To generate protonated species, gas mixtures containing a few percent H₂ are used. Discharges in H₂ create H₃⁺, which is a highly reactive protonating agent. ²²⁻²³

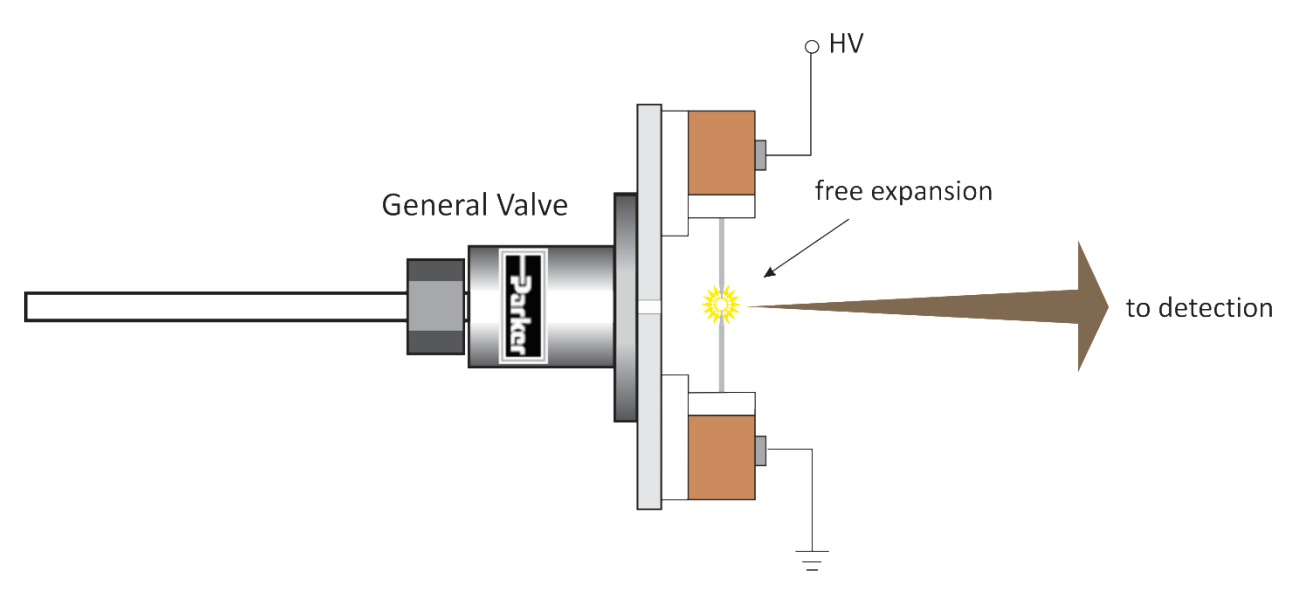


Figure 5. Schematic of the pulsed electrical discharge source.

References

- Cornett, D. S.; Peschke, M.; Laihing, K.; Cheng, P. Y.; Willey, K. F.; Duncan, M. A.
 "Reflectron time-of-flight mass spectrometer for laser photodissociation," *Rev. Sci. Instrum.* 1992, 2177-2186.
- 2. Townsend, D.; Minitti, M. P.; Suits, A. G. "Direct current slice imaging," *Rev. Sci. Instrum.* **2002**, *74*, 2530-2539.
- 3. Li, W.; Chambreau, S. D.; Lahankar, S. A.; Suits, A. G. "Megapixel ion imaging with standard video," *Rev. Sci. Instrum.* **2005**, *76*, 063106. See also NuAcq 0.9 software, Suits, A. G., http://faculty.missouri.edu/suitsa/Technical_Resources.html.
- 4. Daul, D. A. "SIMION for Personal Computer in Reflection," *Int. J. Mass. Spectrom.* **2000**, *200*, 3-25. See also http://simion.com/.
- 5. Maner, J. A.; Mauney, D. T.; Duncan, M. A. "Velocity map ion imaging study of Ar₂⁺ photodissociation," *Chem. Phys. Lett.* **2017**, *671*, 182-185.
- 6. Schneider, C. A.; Rasband, W. S.; Eliceiri, K. W. "NIH Image to ImageJ: 25 years of image analysis," *Nature Methods*, **2012**, *9*, 617-675.
- 7. Suits, A. G.; Miller, R. L.; Bontuyan, L. S.; Houston, P. L. "Photofragment vector correlations by ion imaging: O_2 [a $^1\Delta_g(v,J)$] from 248 nm dissociation of ozone," *J. Chem. Soc., Faraday Trans.* **1993**, 89, 1443-1447.
- 8. Thompson, J. O. F.; Amarasinghe, C.; Foley, C. D.; Suits, A. G. "Finite slice analysis (FINA) A general reconstruction method for velocity mapped and time-sliced ion imaging," *J. Chem. Phys.* **2017**, *147*, 013913. See also Finite Slice Analysis Software, Suits, A. G., http://faculty.missouri.edu/suitsa/Technical_Resources.html.

- 9. Dribinski, V.; Ossadtchi, A.; Mandelshtam, V. A.; Reisler, H. "Reconstruction of Abeltransformable images: the Gaussian Basis-set expansion Abel transform method," *Rev. Sci. Instrum.* **2002**, *73*, 2634-2642.
- 10. Provided by Arthur Suits in a personal communication.
- 11. MATLAB 8.4; MathWorks, Natick, MA, USA 2014.
- 12. Zare, R. N. "Doppler line shape of atomic fluorescence excited by molecular photodissociation," *Proc. IEEE* **1963**, *51*, 173-182.
- 13. Zare, R. N. "Photoejection dynamics," Mol. Photochem. 1972, 4, 1-37.
- 14. Zare, R. N. Angular Momentum; John Wiley & Sons, Inc., New York, NY, USA 1988.
- 15. Rakitzis, T. P.; Zare, R. N.; "Photofragment angular momentum distributions in the molecular frame: Determination and interpretation," *J. Chem. Phys.* **1999**, *110*, 3341-3350.
- 16. Yang, S.-C.; Bersohn, R. "Theory of the angular distribution of molecular photofragments," *J. Chem. Phys.* **1974**, *61*, 4400-4407.
- 17. Siebbeles, L. D. A.; Glass-Maujean, M.; Vasyutinskii, O. S.; Beswick, J. A. "Vector properties in photodissociation: Quantum treatment of the correlation between the spatial anisotropy and the angular momentum polarization of the fragments," *J. Chem. Phys.* **1994**, *100*, 3610-3623.
- 18. Origin 8.6; OriginLab Corporation, Northampton, MA, USA, 2011.
- 19. Duncan, M. A. "Laser vaporization cluster sources," Rev. Sci. Instrum. 2012, 83, 041104.
- 20. Shin, J.-W.; Hammer, N. I.; Diken, E. G.; Johnson, M. A.; Walters, R. S.; Jaeger, T. D.; Duncan, M. A.; Christie, R. A.; Jordan, K. D. "Infrared signature of structures associated with the H⁺(H₂O)_n (n = 6 to 27) clusters," *Science*, **2004**, *304*, 1137-1140.

- 21. Duncan, M. A. "Infrared laser spectroscopy of mass-selected carbocations," *J. Phys. Chem. A* **2012**, *116*, 11477-11491.
- 22. Mosley, J. D.; Young, J. W.; Agarwal, J.; Schaefer, H. F.; Schleyer, P. v. R.; Duncan, M. A. "Structural isomerization of the gas-phase 2-norbornyl cation revealed with infrared spectroscopy and computational chemistry," *Angew. Chem. Int. Ed. Engl.* 2014, 53, 5888-5891.
- 23. McDonald, D. C.; Mauney, D. T.; Leicht, D.; Marks, J. H.; Tan, J. A.; Kuo, J.-L.; Duncan, M. A. "Trapping a proton in argon: Spectroscopy and theory of the proton-bound argon dimer and its solvation," *J. Chem. Phys.* **2016**, *145*, 231101.

CHAPTER 3

PHOTODISSOCIATION OF THE ARGON DIMER CATION

Introduction

Kinetic energy release in the unimolecular decomposition of ion-molecule complexes has been studied extensively using a variety of mass spectrometry-based techniques, including timeof-flight measurements, peak shape analysis, and translational energy spectroscopy. ¹⁻⁵ The argon dimer cation is a prototypical system for these types of experiments. Its simple electronic structure and large absorption cross sections in the UV-visible region make Ar₂⁺ tractable by both theory and experiment. 1,6-22 The binding energy of Ar₂⁺ has been the subject of numerous studies 1,10,15-21 which have been summarized by Weitzel and Mähnert. 21 Moseley and coworkers studied the photodissociation of Ar₂⁺ by measuring translational energy spectra of Ar⁺ in a double focusing reverse geometry instrument, and reported a binding energy of 1.33 ± 0.02 eV. Stace and coworkers employed a similar experiment using ultraviolet excitation, like that employed here. 15 Signorell and Merkt determined a binding energy of 1.3147 ± 0.0008 eV by PFI-ZEKE spectroscopy on Ar₂ and a potential fit of the many cation vibrational levels detected.¹⁹ More recently, Weitzel and Mähnert studied the dissociative ionization of Ar₃ in a TPEPICO experiment and generated a binding energy for Ar_2^+ of 1.29 ± 0.05 eV.²¹ Lepère and coworkers studied Ar₂⁺ in an instrument developed for low-resolution photofragment imaging.²² They reported an angular distribution corresponding to $\beta \approx 1$, indicating a parallel transition, and argued that their results were consistent with a theoretical binding energy of 1.38 eV. In this chapter, we investigate the kinetic energy release and photofragment angular distribution for the

photodissociation of $\mathrm{Ar_2}^+$ at 355 nm using the new SIVMI spectrometer. We derive an independent value for the dissociation energy of this ion, which is consistent with previous results.

Experimental

The SIVMI instrument was described in Chapter 2. Argon clusters are produced in a plasma generated by a pulsed Nd:YAG laser (355 nm, Spectra Physics INDI) focused onto the surface of a tantalum rod in a supersonic expansion of argon (100 psi backing pressure). Ions are photodissociated with the third harmonic of a Nd:YAG laser (355 nm; vertical polarization; Continuum SureLite SL-10). For ion detection, we employ the DC-slice technique.²³ A dual MCP/P-47 phosphor detector (Beam Imaging Solutions BOS-75) is pulsed with a 140-ns gate (DEI PVX-4140), resulting in the detection of only the central ~90 ns of the Ar⁺ arrival time distribution. Images are collected over 200,000 laser shots using a CCD camera (Edmund Optics) and processed using the NuACQ and BasisFit programs of Suits.²⁴⁻²⁵ Images are also reconstructed using the BASEX algorithm of Reisler.²⁶

Results and Discussion

A laser-generated plasma at the surface of a tantalum rod in an argon expansion produces a mass spectrum containing both Ar_n^+ and $Ta(Ar_n)^+$ cluster ions (See Appendix A, Figure 1). Ar_n^+ clusters have been produced with similar laser spark generation using many different metal rods in our lab, but tantalum was chosen to reduce mass spectral congestion in the range of the arrival time of Ar_2^+ and the Ar^+ fragment. Ar_n^+ cluster ions have also been produced in our lab using pulsed electrical discharges with needle or ring electrodes, but this leads to congestion in the lower mass range due to the presence of trace water and hydrocarbon masses. We have noted previously that ions produced by electrical discharges are somewhat warmer than those produced

by the laser spark.²⁷ For example, in previous studies of protonated water clusters, mass spectra generated using the discharge were often skewed toward smaller cluster sizes compared to those produced by the laser spark under similar expansion conditions.²⁸ Ions generated with the spark tend to be cooler, giving sharper linewidths in measured infrared or UV-visible spectra, presumably because the focused output of the laser defines a relatively small ionization volume resulting in minimal heating of the expansion gas. The discharge source has a larger excitation volume, resulting in more extensive ionization and gas heating.

A schematic of the ground and excited state potentials for Ar_2^+ is shown in Figure 1. The excited states of the Ar_2^+ cation have been investigated extensively in previous work.⁷⁻¹⁰ Excitation at 355 nm is expected to cause the $^2\Sigma_g^+ \leftarrow ^2\Sigma_u^+$ transition, with dissociation in the excited state producing Ar^+ ($^2P_{1/2}$) and Ar (1S_0). The ground state binding energy can therefore be related to the kinetic energy release in the excited state via the following energetic cycle:

$$D_0" = hv - KE - SO \tag{1}$$

where KE is the total energy in excess of the dissociation threshold and SO is the spin orbit splitting of Ar^+ (1431.58 cm⁻¹ or 0.177 eV).²⁹ Because we employ a supersonic expansion and the vibrational frequency of Ar_2^+ is small (315 cm⁻¹)¹⁸, it is likely that our Ar_2^+ distribution has cooled efficiently to v'' = 0. Rotational cooling is usually more efficient than vibrational cooling, and therefore we also expect no contribution to our experiment from warm rotations. Additionally, since Ar and Ar^+ do not have low-lying electronic excited states, all of the excess energy must be associated with translation of the neutral and ionic Ar fragments in their ground states.

The photofragment image of Ar⁺ obtained is shown in Figure 2, and the corresponding angular, velocity, and kinetic energy distributions are shown in Figure 3. In a typical VMI

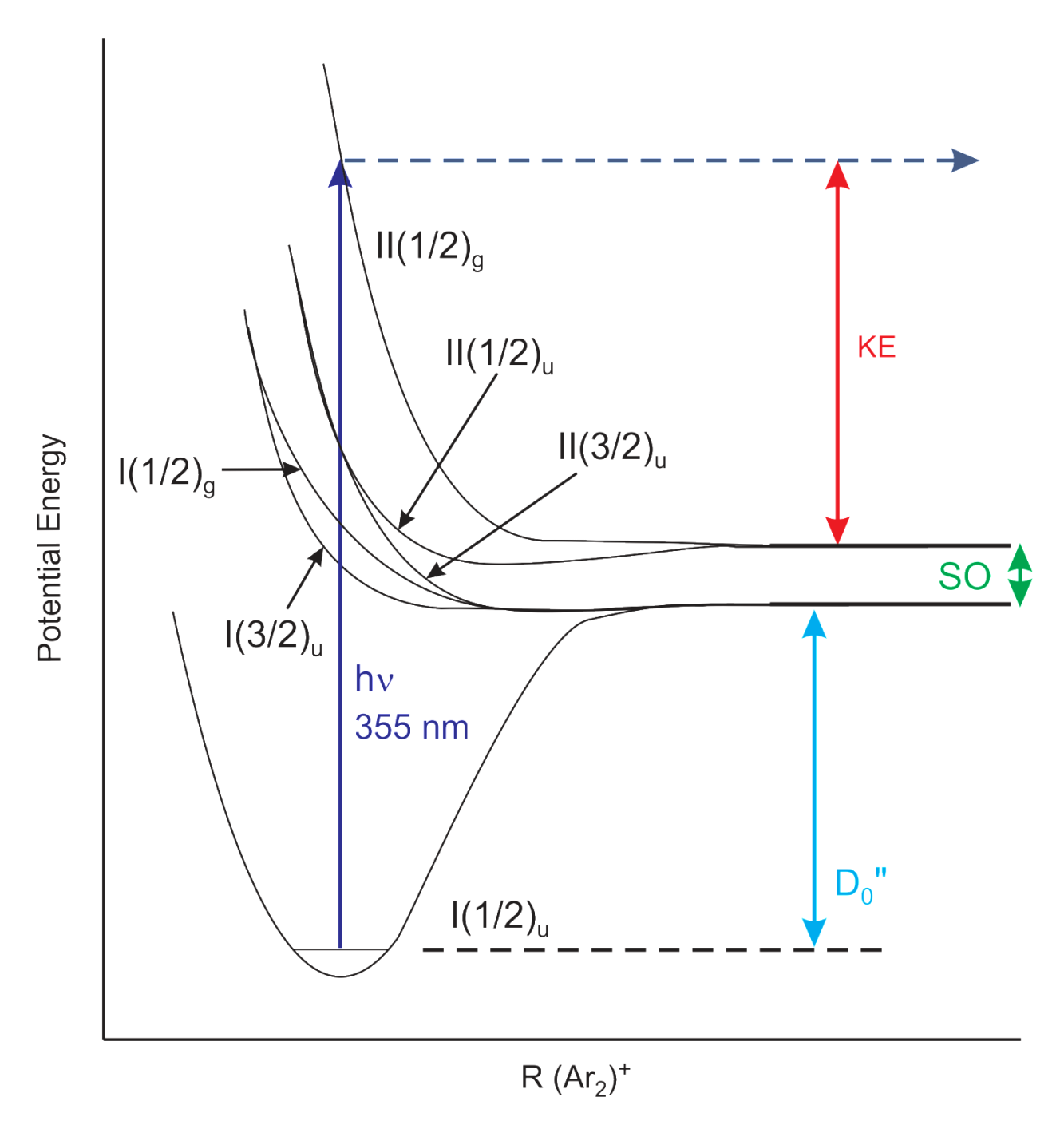


Figure 1. Ground and excited state potentials of $\operatorname{Ar_2}^+$.

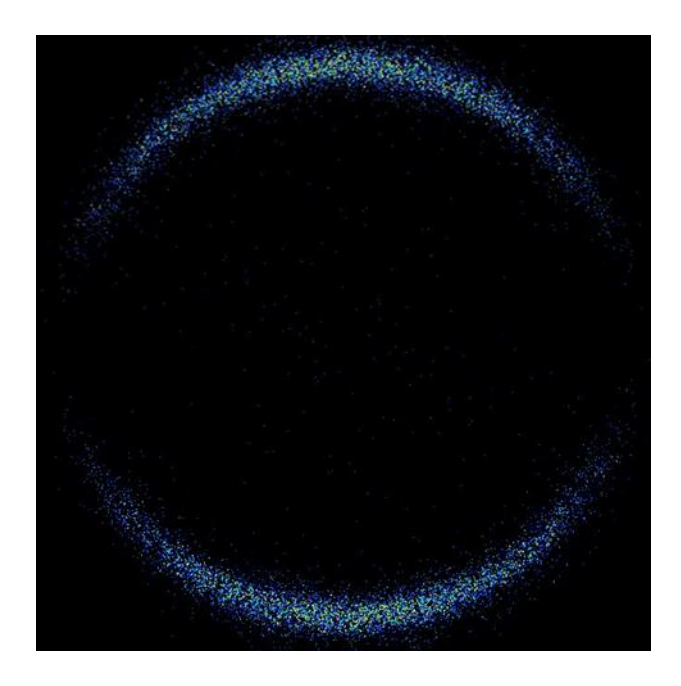


Figure 2. Photofragment ion image of $\mathrm{Ar}^{\scriptscriptstyle +}$ from photodissociation of $\mathrm{Ar_2}^{\scriptscriptstyle +}$ at 355 nm.

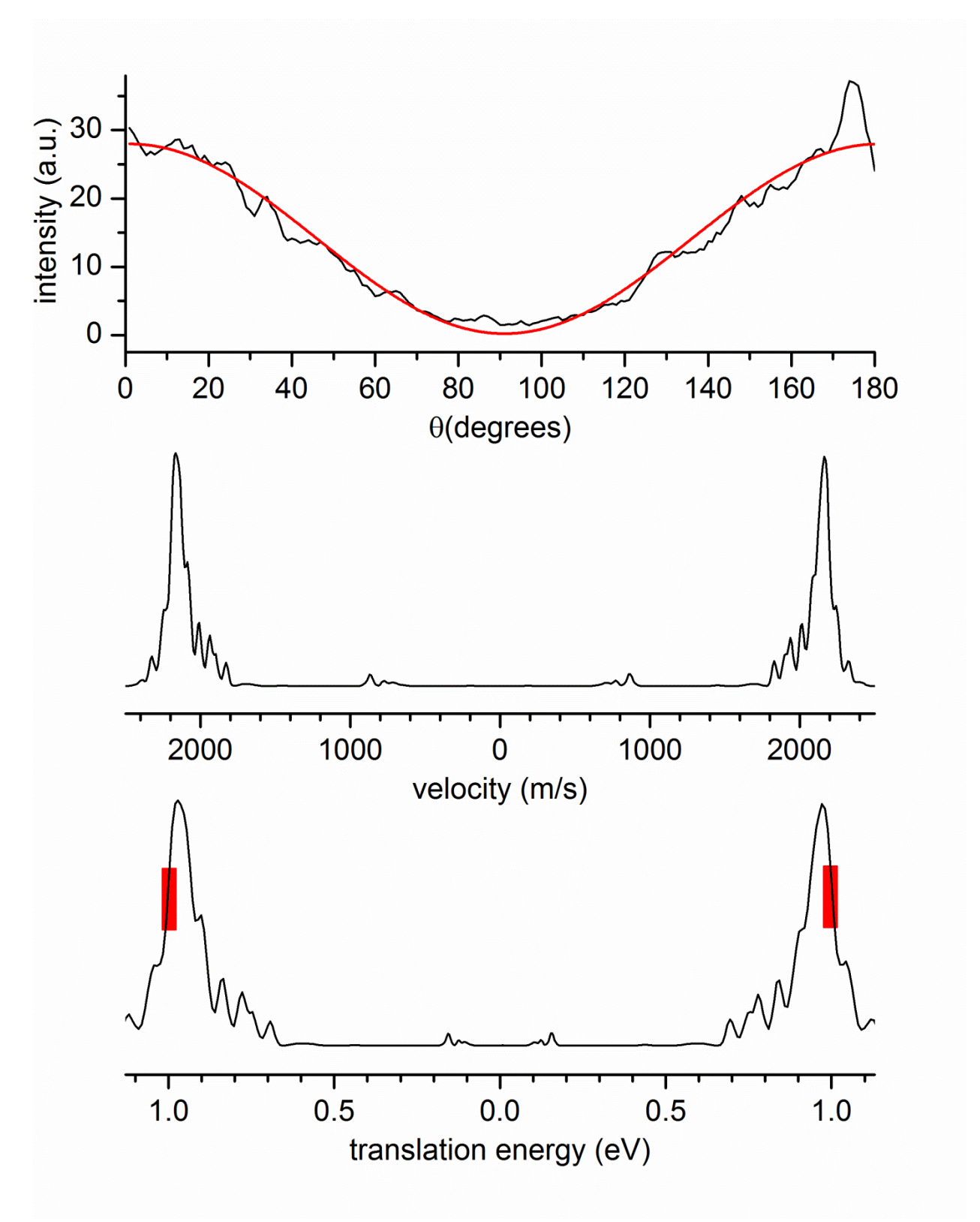


Figure 3. Angular (top), velocity (middle), and kinetic energy (bottom) distributions of Ar^+ from photodissociation of Ar_2^+ at 355 nm.

experiment studying neutral molecules, a velocity calibration is obtained using another system with well-known binding energy. However, there are very few ions with well-known binding energies and spectroscopy accessible under our current conditions. Therefore we use a time-offlight/geometric approach to determine the fragment ion velocities. Using the radius of the Ar⁺ image and the time of flight of the Ar⁺ ions from the excitation point to the front surface of the imaging detector, we calculate the velocity of the Ar⁺ fragment orthogonal to the path of the Ar₂⁺ parent ion beam. This is then directly related to its kinetic energy by ½ my². The diameter of the detector is 75 mm, which corresponds to 1690 pixels and a pixel width of 23 µm. The flight time of Ar⁺ is 13.0 µs, which leads to a calibration factor of 3.41 m/s/pixel. Using this calibration, we plot the intensity profile of the image as a function of velocity as shown in the middle panel of Figure 4. From this velocity distribution, we determine the kinetic energy distribution in the lower panel of Figure 4. Because the edge of the image is noisy, we define the kinetic energy as the midway point between the onset of signal (1.02 eV) and its peak value (0.97 eV). The average of these two energies is 1.00 eV, corresponding to a velocity of 2196 m/s. Using equation 1, we calculate a binding energy of 1.32 +0.03/-0.02 eV. Within this uncertainty, our value for the dissociation energy agrees with other experimental values in the literature (see Table 1). Because of the supersonic expansion used in our source, it is likely that our Ar₂⁺ ions are colder than those studied in some other experiments, which employed electron beam excitation on neutral argon clusters. Such excitation can produce some internally warm Ar₂⁺ ions from the fragmentation of larger clusters. If other experiments had vibrationally or rotationally excited ions, photodissociation would produce a greater excess energy in the fragments, corresponding to lower derived binding energies than our value. The experiment of Signorell and Merkt was quantum-state resolved, and not sensitive to this issue.¹⁹

Table 1. Binding energies for $\operatorname{Ar_2}^+$ from different experiments.

D_0 " (eV)	Method	Reference	
1.33 ± 0.02	MIKES	1	
1.27 ± 0.02	PI	10	
1.24	TPEPICO	14	
1.361	PI	16	
1.32 ± 0.005	PI	17	
1.3147 ± 0.0008	PFI-ZEKE	19	
1.3130 ± 0.0007	PFI-ZEKE	20	
1.29 ± 0.05	TPEPICO	21	
1.32 +0.03/-0.02	SIVMI	This work	

However, the error in our measurement can also arise from the difficulty in defining the edge of the ion image. It is also possible that the gate on the detector is too wide, and that we have not effectively sliced the Ar⁺ temporal distribution. The image was generated from the central 90 ns portion of the total 500 ns distribution, which corresponds to about 20%. This would not change the diameter of the image, but would lead to a widening of the Ar⁺ ring, effectively skewing our results toward higher binding energies. More details about the image processing are provided in Appendix A.

Interestingly, the simple geometric method used here for kinetic energy determination usually cannot be used in VMI studies of neutral photodissociation.³⁰ Under conditions typically employed there, the VMI fields (1–3 kV) are much greater than the initial kinetic energies of the neutral photofragments (typically about 1 eV or less), producing an amplification in the observed image radius. Calibration is then required to determine this amplification factor. In the present work, the initial ion kinetic energy along the ion flight direction is set by deceleration to a value of about 1600 eV, whereas the VMI grids accelerate by an additional 800 eV. Because these two energies are more similar, the image amplification factor should be much smaller. Because we obtained a binding energy in almost perfect agreement with other more accurate experiments, the amplification factor in this ion beam configuration must be very close to 1. This conclusion is consistent with the results of various Simion ion trajectory simulations on our system.

Figures 3 and 4 show the angular distribution of the photofragment signal, which has not been reported previously for this system except at very low resolution.²² The intensity is clearly peaked at 0° and 180°. We fit this distribution to the following equation:

$$I = \frac{1}{4\pi} [1 + \beta P_2(\cos \theta)] \tag{2}$$

where $P_2(\cos\theta)$ is the second order Legendre polynomial and θ is the angle between the electric field vector of the linearly polarized laser and the velocity vector of the ionic fragment.³¹ The β parameter falls between -1 and 2, where -1 indicates a pure perpendicular transition and 2 indicates a pure parallel transition. For $\operatorname{Ar_2}^+$, we determined β values of 1.71–1.95, depending on how the image is processed (see details about the distribution fitting in the Supporting Information). These values are consistent with the excitation of the ${}^2\Sigma_g^+ \leftarrow {}^2\Sigma_u^+$ transition, as expected.

The data presented here show how the imaging of ion photodissociation can be used to derive dissociation energies and to reveal the polarization of the electronic transitions involved for the prototypical argon dimer cation. In the case of the dissociation energy, our imaging result cannot compete with the accuracy obtained with high resolution laser PFI-ZEKE experiments.¹⁹⁻²⁰ However, its uncertainty is perhaps comparable to values obtained by other measurements of kinetic energy release. As noted in other work, measurements of kinetic energy release can also avoid the threshold effects found in collision-induced dissociation measurements.⁴⁻⁵ Because the ions in our experiment are produced in a cold supersonic expansion, uncertainties in their internal energy content are also significantly reduced. It is encouraging that our imaging results, even with their uncertainties, are consistent with the best data obtained for the dissociation energy by these other experiments. Because of this, similar imaging experiments may be useful in future studies to derive energetics for ions or ion-molecule complexes that cannot be studied by other methods.

Conclusion

The photodissociation of the argon dimer cation at 355 nm has been investigated with velocity map imaging. This provides a new and independent probe of the photodissociation

dynamics in this system. The kinetic energy release following dissociation in the excited state is used in an energetic cycle to derive the ground state dissociation energy. Although the imaging method provides lower resolution than spectroscopic methods, the bond energy derived is consistent with previous high resolution results. Additionally, the angular distribution of the Ar⁺ fragment indicates that excitation takes place via a parallel transition, consistent with the $^2\Sigma_g^+\leftarrow$ $^2\Sigma_u^+$ transition expected at this energy. Imaging the products of selected-ion photodissociation provides another method in the toolbox of mass spectrometry applicable to a variety of ions and ion-molecule complexes.

References

- Moseley, J. T.; Saxon, R. P.; Huber, B. A.; Cosby, P. C.; Abouaf, R.; Tadjeddine, M.
 "Photofragment spectroscopy and potential curves of Ar₂⁺," *J. Chem. Phys.* 1977, 67, 1659-1668.
- 2. Illies, A. J.; Jarrold, M. F.; Wagner-Redeker, W.; Bowers, M. T. "Photoinduced intramolecular charge transfer: Photodissociation of CO⁺·Ar cluster ions," *J. Am. Chem. Soc.* **1985**, *107*, 2842-2849.
- 3. Snodgrass, J. T.; Dunbar, R. C.; Bowers, M. T. "Photodissociation of the benzene dimer cation in the gas phase," *J. Phys. Chem.* **1990**, *94*, 3648-3651.
- 4. Laskin, J.; Lifshitz, C. "Kinetic energy release distributions in mass spectrometry," *J. Mass Spectrom.* **2001**, *36*, 459-478.
- Ervin, K. M. "Experimental techniques in gas-phase ion thermochemistry," *Chem. Rev.* 2001, 101, 391-444.
- 6. Stevens, W. J.; Gardner, M.; Karo, A.; Julienne, P. "Theoretical determination of bound–free absorption cross sections in Ar₂⁺," *J. Chem. Phys.* **1977**, *67*, 2860-2867.

- Michels, H. H.; Hobbs, R. H.; Wright, L. A. "Electronic structure of the noble gas dimer ions. I. Potential energy curves and spectroscopic constants," *J. Chem. Phys.* 1978, 69, 5151-5162.
- 8. Vanderhoff, J. A. "Photodissociation cross sections for Ar_2^+ , Kr_2^+ , and Xe_2^+ at 3.0 and 3.05 eV," *J. Chem. Phys.* **1978**, *68*, 3311-3313.
- 9. Wadt, W. R. "The electronic states of Ar₂⁺, Kr₂⁺, and Xe₂⁺. I. Potential curves with and without spin–orbit coupling," *J. Chem. Phys.* **1978**, *68*, 402-414.
- 10. Dehmer, P. M.; Pratt, S. T. "Photoionization of argon clusters," *J. Chem. Phys.* **1982**, *76*, 843-853.
- 11. Castleman, A. W.; Keesee, R. G. "Ionic clusters," Chem. Rev. 1986, 86, 589-618.
- 12. Levinger, N. E.; Ray, D.; Alexander, M. L.; Lineberger, W. C. "Photoabsorption and photofragmentation studies of Ar_n⁺ cluster ions," *J. Chem. Phys.* **1988**, *89*, 5654-5662.
- 13. Deluca, M. J.; Johnson, M. A. "Observation of a UV absorption band in Ar₃⁺ near 300 nm," *Chem. Phys. Lett.* **1989**, *162*, 445-448.
- 14. Norwood, K.; Guo, J.-H.; Ng, C. Y. "A photoion–photoelectron coincidence study of Arn (n=2-4)," *J. Chem. Phys.* **1989**, *90*, 2995-3003.
- 15. Woodward, C. A.; Whitaker, B. J.; Stace, A. J. "Ultraviolet photodissociation of Ar₂⁺ and Ar₃⁺," *J. Chem. Soc. Faraday Trans.* **1990**, *86*, 2069-2070.
- Pradeep, T.; Niu, B.; Shirley, D. A. "Photoelectron spectroscopy of rare gas dimers revisted: Vibrationally resolved photoelectron spectrum of argon dimer," *J. Chem. Phys.* 1993, 98, 5269-5275.

- 17. Hall, R. I.; Lu, Y.; Morioka, Y.; Matsui, T.; Tanaka, T.; Yoshii, H.; Hayaishi, T.; Ito, K.

 "High resolution threshold photoelectron spectroscopy of rare gas dimers," *J. Phys. B: At. Mol. Opt. Phys.* **1995**, 28, 2435-2451.
- 18. Gadea, F. X.; Paidarová, I. "Ab initio calculations for Ar₂⁺, He₂⁺ and He₃⁺, of interest for the modelling of ionic rare-gas clusters," *Chem. Phys.* **1996**, 281-290.
- 19. Merkt, F.; Signorell, R. "The first electronic states of Ar₂⁺ studied by high resolution photoelectron spectroscopy," *J. Chem. Phys.* **1998**, *109*, 9762-9771.
- Onuma, T.; Yoshii, H.; Ishijima, H.; Itou, Y.; Hayaishi, T.; Morioka, Y. "Pulsed-field ionization zero-kinetic-energy photoelectron spectra of Ar₂," *J. Mol. Spec.* 1999, 198, 209-217.
- 21. Weitzel, K.-M.; Mähnert, J. "The binding energies of small Ar, CO and N₂ cluster ions," *Int. J. Mass. Spectrom.* **2002**, *214*, 175-212.
- 22. Lepère, V.; Picard, Y. J.; Barat, M.; Fayeton, J. A.; Lucas, B.; Bèroff, K.
 "Photodissociation dynamics of Ar₂⁺ and Ar₃⁺ excited by 527 nm photons, *J. Chem. Phys.*2009, *130*, 194301.
- 23. Townsend, D.; Minitti, M. P.; Suits, A. G. "Direct current slice imaging," *Rev. Sci. Instrum.* **2003**, *74*, 2530-2539.
- 24. Li, W.; Chambreau, S. D.; Lahankar, S. A.; Suits, A. G. "Megapixel ion imaging with standard video," *Rev. Sci. Instrum.* **2005**, *76*, 063106. See also NuAcq 0.9 software, Suits, A. G., http://faculty.missouri.edu/suitsa/Technical_Resources.html.
- 25. Provided by Arthur Suits in a personal communication.

- 26. Dribinski, V.; Ossadtchi, A.; Mandelshtam, V. A.; Reisler, H. "Reconstruction of Abeltransformable images: the Gaussian Basis-set expansion Abel transform method," *Rev. Sci. Instrum.* **2002**, *73*, 2634-2642.
- 27. Duncan, M. A. "Laser vaporization cluster sources," Rev. Sci. Instrum. 2012, 83, 041101.
- 28. Shin, J.-W.; Hammer, N. I.; Diken, E. G.; Johnson, M. A.; Walters, R. S.; Jaeger, T. D.; Duncan, M. A.; Christie, R. A.; Jordan, K. D. "Infrared signature of structures associated with the H⁺(H₂O)_n (n = 6 to 27) clusters," *Science*, **2004**, *304*, 1137-1140.
- 29. Hansen, J. E.; Persson, W. "Identification of the 3p⁴(¹D)⁵d²S term in Ar II," *J. Phys. B: At. Mol. Phys.* **1982**, *15*, L269-273.
- 30. Eppink, A. T. J. B.; Parker, D. H. "Velocity map imaging of ions and electrons using electrostatic lenses: Application in photoelectron and photofragment ion imaging of molecular oxygen," *Rev. Sci. Instrum.* **1997**, *68*, 3477-3484.
- 31. Rakitzis, T. P.; Zare, R. N.; "Photofragment angular momentum distributions in the molecular frame: Determination and interpretation," *J. Chem. Phys.* **1999**, *110*, 3341-3350.

CHAPTER 4

PHOTODISSOCIATION OF THE SILVER-BENZENE CATION

Introduction

Light-driven charge transfer reactions are essential for the separation of charge and transfer of energy in a variety of photochemical processes. ¹⁻³ Inorganic charge transfer complexes have been thoroughly studied, including in some of the early work by Mulliken. ⁴ Photoinduced charge transfer reactions have also been studied in the gas phase. The Bowers group employed mass-analyzed ion kinetic energy spectroscopy to study dissociative charge transfer process in ion-molecule complexes of small atmospheric molecules. ⁵⁻⁶ The Duncan group observed dissociative charge transfer in several transition metal–benzene complexes. ⁷⁻¹⁰ It was shown that for transition metals with low-lying excited states, photodissociation led to either elimination of neutral benzene or charge transfer producing the benzene cation. For copper and silver complexes, the benzene cation was the exclusive product. ⁷⁻⁹

Metal ion–benzene complexes are an important class of organometallic compounds, and they provide simple models for cation– π interactions in advanced materials such as graphene and fullerenes. Ag⁺– π interactions play an important role in new organometallic materials, and compounds of this type have been thoroughly studied both theoretically and experimentally. The ionization potential of benzene (9.24 eV) is higher than the ionization potentials of most metals. Therefore the charge in a typical metal ion–benzene complex is localized on the metal atom in the ground state. This is consistent with the results of photodissociation experiments and collision-induced dissociation experiments. The photodissociation experiments of the Duncan

group showed that the excited complexes dissociate by charge transfer and ligand elimination, strongly suggesting charge transfer must occur on excited state potential energy surface. In the collision-induced dissociation (CID) experiments of Armentrout, complexes dissociate on the ground state surface and only ligand elimination is observed. Threshold CID studies can also be used to generate binding energies for metal ion-benzene complexes. These typically fall in the range of 40-60 kcal/mol. Armentrout and coworkers determined a binding energy of 37.4 kcal/mol for $Ag^+(C_6H_6)$ using threshold CID. The Duncan group estimated an upper limit on the binding energy of $Ag^+(C_6H_6)$ of 30 kcal/mol based on the observed threshold for photodissociation at 418 nm.

Schematic potentials for the ground and excited states of $Ag^+(C_6H_6)$ are shown in Figure 1. These potentials correlate asymptotically with the atomic states of Ag^+ and the molecular states of benzene. The charge transfer state correlates to neutral Ag atom and $C_6H_6^+$. This state lies higher than the ground state asymptote by the difference in ionization potential between silver and benzene (Ag: 7.572; C_6H_6 : 9.24 eV; Δ IP: 1.668 eV). The first excited state of Ag^+ lies at 4.86 eV, and the charge transfer state is the only low-lying state for $Ag^+(C_6H_6)$.

 $Ag^+(C_6H_6)$ binding in the ground state is dominated by electrostatic interactions, in which the Ag atom resembles a point charge interacting with the polarizable π -cloud of benzene. $^{8,19\text{-}20}$ However, the $Ag-C_6H_6^+$ interaction is less favorable, because the charge is delocalized in the aromatic ring of the benzene molecule and the Ag atom is not effectively polarized. Thus UV excitation of $Ag^+(C_6H_6)$ results in population of the repulsive charge transfer state and subsequent dissociation to Ag and $C_6H_6^+$.

Because UV excitation accesses a repulsive region of the charge transfer surface, photodissociation should result in significant release of kinetic energy (KER). Kinetic energy

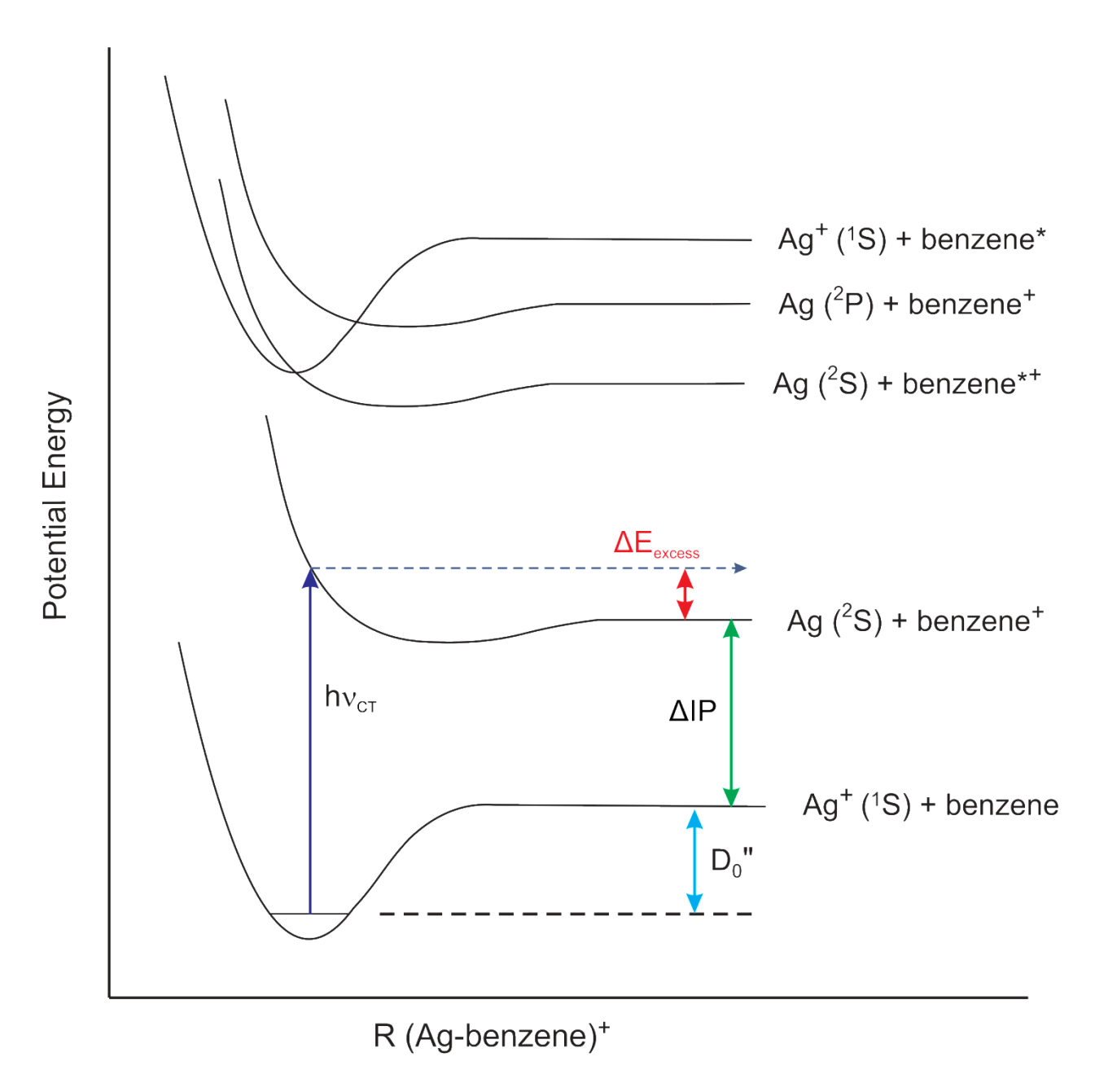


Figure 1. Schematic ground and excited state potential energy surfaces of Ag⁺(C₆H₆).

release measurements using some translational energy spectroscopy technique would therefore provide a new probe for the energetics and dynamics of the dissociative charge transfer process. While there are many approaches to translational energy spectroscopy (see Chapter 1), photofragment imaging techniques represent the state of the art for measuring ion kinetic energies. In this study, we present the application of our new SIVMI instrument to the photodissociation of $Ag^+(C_6H_6)$. There are very few examples of imaging experiments on ionic systems and perhaps even fewer on metal-containing systems (See Chapter 1). Nis work provides a unique example of an imaging experiment incorporating a laser vaporization source for studying the photodissociation dynamics of ion–molecule complexes.

Experimental

The SIVMI instrument was described in Chapter 2. Ag-benzene complexes were generated by laser vaporization (Nd:YAG laser; 355 nm; Spectra-Physics INDI) of a silver rod in an argon expansion (80 psi) seeded with benzene. The mass-selected complexes were dissociated with the unfocused third (355 nm) or fourth (266 nm) harmonics (< 2 mJ) of an Nd:YAG laser (Continuum Surelite SL-10, vertical polarization). The detector was triggered with a 140 ns gate, resulting in the detection of the central 90 ns slice of the 500 ns temporal distributions. Images were collected using a CCD camera (Edmund Optics) and the NuAcq acquisition software. A photomultiplier tube was used to record time-of-flight data and monitor ion intensity at the detector. The instrument was optimized and calibrated based on the Ar₂+ system, which has a favorable cross-section at 355 nm and a well-known binding energy (see Appendix B, Figure 1–3). Computational studies were performed at the DFT/M06-L/Def2-QZVP(Ag)/6-311++g(2d,2p)(C,H) level using the Gaussian09 program package.

Results and Discussion

Photodissociation of $Ag^+(C_6H_6)$ producing $C_6H_6^+$ is efficient at 355 nm, and we have estimated a cross section of 10⁻¹⁶ cm^{2,7-9} The corresponding photofragment image and total kinetic energy distribution are shown in Figure 2. Ion intensities are clearly peaked at the top and bottom of the image. Thus it is apparent upon inspection that the charge transfer process is related to a parallel transition. We have determined a β value of 0.40, which is qualitatively consistent with this observation (See Appendix B, Figure 7). Because product ions are not stateselected as in experiments on neutral systems, the image represents a distribution of all possible product ion states. However, it is clear that the benzene cation is produced with significant translational energy. Still, there is some intensity at the center of the image, indicating that some fraction of C₆H₆⁺ is produced with near-zero translational energy. Therefore, a portion of the kinetic energy released upon dissociation must be converted to internal energy of C₆H₆⁺. If the vertical transition to the charge transfer state leads to direct vibrational excitation, the C₆H₆⁺ product may also be vibrationally excited. $^{5\text{-}6}$ Vibrationally excited $C_6H_6^+$ could also be produced if dissociative charge transfer is a predissociation process with a lifetime long enough to allow vibrational relaxation. ⁵⁻⁶ Rotational excitation of the C₆H₆⁺ is another possibility. The computed structure for Ag⁺(C₆H₆) is asymmetric, and the metal atom is located at the edge of the ring with no preference for η^1 or η^2 binding (See Appendix B, Figure 9-10).²⁰ Dissociation along one coordinate of an asymmetric or bent structure may lead to rotational excitation of the products. This would result in a velocity-rotation correlation in which fast ions are not highly rotationally excited and vice versa.⁴³

The outer edge of the image in Figure 3 corresponds to benzene ions with a velocity of 1316 ± 100 m/s relative to the Ag atom. Accounting for the velocity and kinetic of energy of the

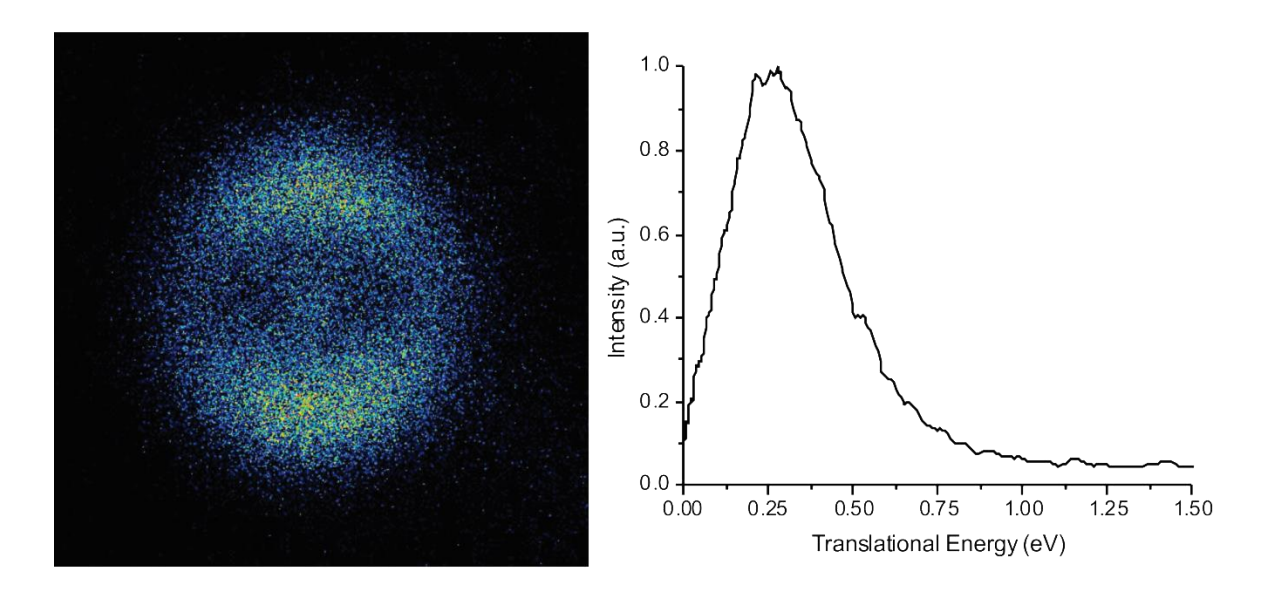


Figure 2. Photofragment image of $C_6H_6^+$ from photodissociation of $Ag^+(C_6H_6)$ at 355 nm and the total kinetic energy distribution.

Ag cofragment leads to a total KER of 0.404 eV. This value corresponds to a lower limit on the exothermicity of the dissociative charge transfer process. The kinetic energy distribution is given in the right frame of Figure 2. Clearly benzene cations are produced with a wide range of kinetic energies, and a portion of the total KER must be partitioned among the internal degrees of freedom of $C_6H_6^+$. It is even possible that all benzene cations are internally excited to some extent. Looking at Figure 1 and the total KER, we can use the following energetic cycle to estimate an upper limit for the binding energy of $Ag^+(C_6H_6)$.

$$D_0" \le h\nu - \Delta IP - KER \tag{1}$$

For dissociation at 355 nm (3.493 eV) and a total KER of 0.404 eV, we obtain D_0 " $\leq 3.493 -$ 1.668 - 0.404 = 1.421 eV (32.8 + 1.4/ -1.5 kcal/mol). This result is higher than our previous estimate of 30.0 kcal/mol.⁸ However, our photodissociation threshold measurements described previously were carried out using a helium expansion. For this study, we have repeated our measurements in several expansion gases and determined that argon expansions result in the coldest ions and smallest image diameter (See Appendix B, Figure 4-6). Our current value is still lower than that of Armentrout (37.4 kcal/mol) determined using threshold CID. 15 We have discussed this issue with Armentrout and he has provided us with a revised value of 35.4 ± 2.3 kcal/mol. 45 This number corresponds to ions at 0 K. We estimate the temperature of our ions to be 50-100 K based on the spectra of other ions generated with similar source conditions, resulting in average internal energies of 0.23-0.60 kcal/mol.⁴⁴ Because we employ a supersonic expansion in our ion source, it is unlikely that all vibrational modes are in equilibrium at any temperature. It is not clear how the internal energy of an ion could be converted to translation energy of the fragments. However, our imaging results in helium and CO₂ expansions suggest that internal excitation can lead to higher translational excitation (See Appendix B, Figure 4-6).

Taking all of this into consideration, we can shift our value upward by the estimated internal energy at 50-100 K, and we are essentially in agreement with the CID results. We can also compare our value with theoretical binding energies (Table 1). Theoretical values range from 34-44 kcal/mol for η^1 or η^2 structures. We have studied this system at the M06-L/Def2-QZVP(Ag)/6-311++g(2d,2p)(C,H) level and calculated a binding energy of 37.3 kcal/mol for the η^2 structure. Al-42

We have also studied the photodissociation $Ag^+(C_6H_6)$ at 266 nm and the relative cross section for production of $C_6H_6^+$ is nearly twice that at 355 nm. $C_6H_6^+$ is the only fragment detected. This confirms that dissociation takes place on the same $Ag(^2S) + C_6H_6^+$ excited state surface, which is the only state expected in this energy region. The image and kinetic energy distribution are shown in Figure 3. This image is nearly isotropic ($\beta = 0.05$) and has significantly more intensity in the middle compared to the image for 355 nm (See Appendix B, Figure 8). The maximum relative velocity is 1684 ± 100 m/s, corresponding to a kinetic energy of 0.663 eV. Using equation 1, we obtain $D_0'' \le 53.8$ kcal/mol. This is not surprising since the image for 266 nm is only slightly larger than that for 355 nm. Apparently, photodissociation at higher energy leads mostly to the production of slow, internally excited fragments.

As was the case with results at 355 nm, the image corresponding to dissociation at 266 nm can be understood in terms of the structure of $Ag^+(C_6H_6)$. Because the Ag^+ is located on the edge of the ring and not centered over the π system, dissociation along the $Ag-C_6H_6$ coordinate results in a torque and rotational excitation of $C_6H_6^+$. This rotational excitation could lead to a more isotropic ion distribution. The β value for 355 nm (0.40) is greater than the value for 266 nm (0.05), but neither are close to 2, the value expected for a purely parallel transition. There are no other electronic states that can be reached with 355 nm or 266 nm excitation, and so these

Table 1. The dissociation energies (kcal/mol) of Ag⁺(benzene) complexes from experiments and theory.

Experiments						
CID	$37.4 \pm 1.7^{a} (35.4 \pm 2.3)$					
TP	30.0^{b}					
VMI	$32.8 + 1.4 / -1.5^{\circ}$					
Theory	C	6v	$C_s(\eta^1)$	$C_s(\eta^2)$		
MCPF/ANO ^d	34	4.6				
MCPF/DZP ^d	30	6.5				
MP2/Stuttgart ^e	43	3.6	43.7	44.2		
CCSD(T)/Stuttgart ^e	39	9.2	39.7	40.0		
M06-L/Def2-QZVP ^c	_		36.8	37.3		

^aArmentrout and coworkers; collision-induced dissociation. ¹⁵ Number in parenthesis indicates new fit of old data. ⁴⁴

^bDuncan and coworkers; threshold photodissociation.⁸

^cpresent work. ^dBauschlicher and coworkers.¹⁹ ^eKoch and coworkers.²⁰

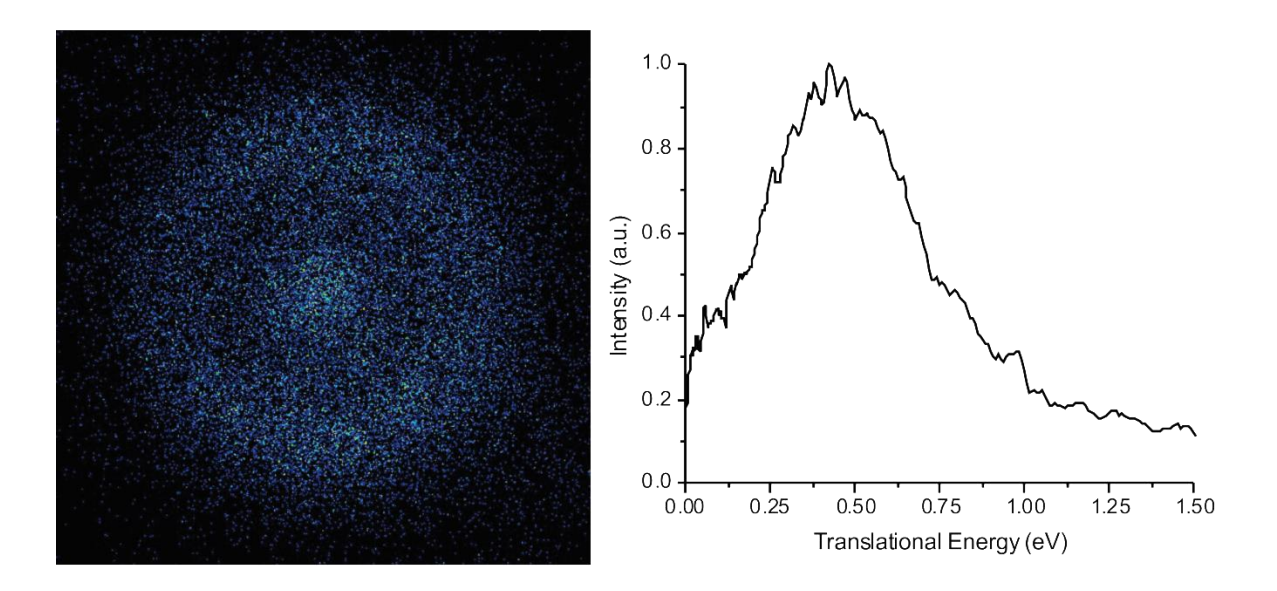


Figure 3. Photofragment image of $C_6H_6^+$ from photodissociation of $Ag^+(C_6H_6)$ at 266 nm and the total kinetic energy distribution.

results could be attributed to recoil dynamics. In this case, excitation at higher energy results in greater torque and a more isotropic image.

We must also consider vibrational excitation of $C_6H_6^+$. The Franck–Condon overlap between ground and excited states will be different for 355 nm and 266 nm excitation, and higher vibrational excitation is expected for higher energies. Ag⁺ binding causes elongation of the C–C bonds, and bonds near the metal atom are longer than those on the opposite side of the ring (See Appendix B, Figure 9-11). In addition, the C–H bonds are bent out of the plane of the benzene ring. The benzene cation is planar with all C–C bonds contracted relative to the $Ag^+(C_6H_6)$ structure. These geometric differences could conceivably lead to vibrational excitation in the excited charge transfer state followed by dissociation to produce vibrationally hot $C_6H_6^+$. If the lifetime of the excited state is longer than a rotational period, any anisotropy would be lost.

Conclusion

The photodissociation of $Ag^+(C_6H_6)$ has been investigated using our new apparatus for selected-ion velocity map imaging. We have generated anisotropy parameters for photodissociation at both 355 nm and 266 nm. Based on the corresponding angular distributions we have concluded that while dissociation at both photon energies proceeds by $Ag^+-C_6H_6$ charge transfer producing $C_6H_6^+$, dissociation at 266 nm leads to significantly greater internal excitation of the benzene cation. We have also estimated an upper limit on the dissociation energy of $Ag^+(C_6H_6)$ of 32.8 + 1.4/-1.5 kcal/mol, which is in agreement with previous experiments.

References

1. Marcus, R. A. "Electron transfer reactions in chemistry: Theory and experiment (Nobel lecture)," *Angew. Chem. Int. Ed.* **1993**, *32*, 1111–1121.

- Barbara, P. F.; Meyer, T. J.; Ratner, M. A. "Contemporary issues in electron transfer Research," J. Phys. Chem. 1996, 100, 13148–13168.
- Adams, D. M.; Brus, L.; Chidsey, C. E. D.; Creager, S.; Creutz, C.; Kagan, C. R.; Kamat, P. V.; Lieberman, M.; Lindsay, S.; Marcus, R. A.; Metzger, R. M.; Michel-Beyerle, M. E.; Miller, J. R.; Newton, M. D.; Rolison, D. R.; Sankey, O.; Schanze, K. S.; Yardley, J.; Zhu, X. "Charge transfer on the nanoscale: Current status," *J. Phys. Chem. B* 2003, *107*, 6668–6697.
- 4. Mulliken, R. S. "Molecular compounds and their spectra. II," *J. Am. Chem. Soc.***1952**, *74*, 811–824.
- 5. Illies, J. I.; Jarrold, M. F.; Wagner-Redeker, W.; Bowers, M. T. "Photoinduced intramolecular charge transfer: Photodissociation of CO₂⁺·Ar cluster ions" *J. Am. Chem. Soc.* **1985**, *107*, 2842–2849.
- 6. Kim, H.-S.; Kuo, C.-H.; Bowers, M. T. "Photon driven charge transfer half-collisions: The photodissociation of CO_2^+ · O_2 cluster ions with resolution of the O_2 product vibrational states," *J. Chem. Phys.* **1987**, 87, 2667–2676.
- 7. Willey, K. F.; Cheng, P. Y.; Pearce, K. D.; Duncan, M. A. "Photoinitiated charge transfer and dissociation in mass-selected metalloorganic complexes," *J. Phys. Chem.* **1990**, *94*, 4769–4772.
- 8. Willey, K. F.; Cheng, P. Y.; Bishop, M. B.; Duncan, M. A. "Charge-transfer Photochemistry in ion-molecule cluster complexes of silver," *J. Am. Chem. Soc.* **1991**, *113*, 4721–4728.

- 9. Willey, K. F.; Cheng, P. Y.; Robbins, D. L.; Duncan, M. A. "Charge transfer in the photodissociation of metal ion-benzene complexes," *J. Phys. Chem.* **1992**, *96*, 9106–9111.
- Jaeger, T. D.; Duncan, M. A. "Photodissociation of M⁺(benzene)_x complexes (M= Ti, V, Ni) at 355 nm," *Int. J. Mass Spectrom.* 2005, 241, 165–171.
- 11. Long, N. J. Metallocenes, Blackwell Sciences, Ltd., Oxford, UK, 1998.
- 12. Mahadevi, A. S.; Sastry, G. N. "Cation-π interaction: Its role and relevance in chemistry, biology, and materials science," *Chem. Rev.* **2013**, *113*, 2100–2138.
- 13. Chebny, V. J.; Rathore, R. "Convergent synthesis of alternating fluorene-*p*-xylene oligomers and delineation of the (silver) cation-induced folding," *J. Am. Chem. Soc.* **2007**, *129*, 8458–8465.
- 14. Omoto, K.; Tashiro, S.; Kuritani, M.; Shionoya, M. "Multipoint recognition of ditopic guest molecules via Ag-π interactions within a dimetal macrocycle," *J. Am. Chem. Soc.*2014, 136, 17946–17949.
- 15. Chen, Y.-M.; Armentrout, P. B. "Collision-induced dissociation of $Ag(C_6H_6)^+$," *Chem. Phys. Lett.* **1993**, *210*, 123–128.
- 16. Meyer, F.; Khan, F. A.; Armentrout, P. B. "Thermochemistry of transition metal benzene complexes: Binding energies of $M(C_6H_6)_x^+$ (x = 1, 2) for M = Ti to Cu," *J. Am. Chem. Soc.* **1995**, *117*, 9740–9748.
- 17. Reddic, J. E.; Robinson, J. C.; Duncan, M. A. "Growth and photodissociation of Ag_x-C₆₀ cation complexes," *Chem. Phys. Lett.* **1997**, *279*, 203–208.
- 18. Buchanan, J. W.; Grieves, G. A.; Flynn, N. D.; Duncan, M. A. "Photodissociation of silver-coronene cluster cations," *Int. J. Mass Spectrom.* **1999**, *185/186/187*, 617–624.

- 19. Bauschlicher, C. W., Jr.; Partridge, H.; Langhoff, S. R. "Theoretical study of transition—metal ions bound to benzene," *J. Phys. Chem.* **1992**, *96*, 3273–3278.
- 20. Dargel, T. K.; Hertwig, R. H.; Koch, W. "How do coinage metal ions bind to benzene?" *Mol. Phys.* **1999**, *96*, 583–591.
- 21. Duncan, M. A. "Structures, energies and spectroscopy of gas phase transition metalbenzene complexes," *Int. J. Mass Spectrom.* **2008**, 272, 99–118.
- 22. Nemeth, G. I.; Selzle, H. L.; Schlag, E. W. "Magnetic ZEKE experiments with mass analysis," *Chem. Phys. Lett.* **1993**, *215*, 151–155.
- 23. Loock, H.-P.; Beaty, L. M.; Simard, B. "Reassessment of the first ionization potentials of copper, silver, and gold," *Phys. Rev. A* **1999**, *59*, 873-875.
- 24. Laskin, J.; Lifshitz, C. "Kinetic energy release distributions in mass spectrometry," *J. Mass. Spectrom.* **2001**, *36*, 459–478.
- Suits, A. G.; Continetti, R. E. *Imaging in Chemical Dynamics*, ACS Symposium Series
 American Chemical Society, Washington, DC, USA 2001.
- 26. Whitaker, B. *Imaging in Molecular Dynamics: Technology and Applications*, Cambridge University Press, UK, 2003.
- 27. Townsend, D.; Li, W.; Lee, S. K.; Gross, R. L.; Suits, A. G. "Universal and state-resolved imaging of chemical dynamics," *J. Phys. Chem. A* **2005**, *109*, 8661–8674.
- 28. Ashfold, M. N. R.; Nahler, N. H.; Orr-Ewing, A. J.; Vieuxmaire, O. P. J.; Toomes, R. L.; Kitsopoulos, T. N.; Garcia, I. A.; Chestakov, D. A.; Wu, S. M.; Parker, D. H. "Imaging the dynamics of gas phase reactions," *Phys. Chem. Chem. Phys.* **2006**, *8*, 26–53.

- 29. Kim, M. H.; Leskiw, B. D.; Suits, A. G. "Vibrationally mediated photodissociation of ethylene cation by reflectron multimass velocity map imaging," *J. Phys. Chem. A* **2005**, *109*, 7839–7842.
- 30. Kim, M. H.; Leskiw, B. D.; Shen, L.; Suits, A. G. "Vibrationally mediated photodissociation of C₂H₄⁺," *J. Phys. Chem. A* **2007**, *111*, 7472–7480.
- 31. Gichuhi, W. K.; Mebel, A. M.; Suits, A. G. "UV photodissociation of ethylamine cation: A combined experimental and theoretical investigation," *J. Phys. Chem. A* **2010**, *114*, 13296–13302.
- 32. Wester, R. "Velocity map imaging of ion-molecule reactions," *Phys. Chem. Chem. Phys.* **2014**, *16*, 396–405.
- 33. Pei, L.; Farrar, J. M. "Imaging ion-molecule reactions: Charge transfer and halide transfer reactions of O⁺ with CH₃Cl, CH₃Br, and CH₃I," *Int. J. Mass Spectrom.* **2015**, *377*, 93–100.
- 34. Hopkins, W. S.; Hamilton, S. M.; McNaughter, P. D.; MacKenzie, S. R. "VUV photodissociation dynamics of diatomic gold, Au₂: A velocity map imaging study at 157 nm," *Chem. Phys. Lett.* **2009**, *483*, 10–15.
- 35. Cooper, G. A.; Kartouzian, A.; Gentleman, A. S.; Iskra, A.; van Wijk, R.; MacKenzie, S. R. "Dissociation energies of Ag-RG (RG = Ar, Kr, Xe) and AgO molecules from velocity map imaging studies," *J. Chem. Phys.* **2015**, *143*, 124302.
- 36. Hoshino, H.; Yamakita, Y.; Okutsu, K.; Suzuki, Y.; Saito, M.; Koyasu, K.; Ohshimo, K.; Misaizu, F. "Photofragment imaging from mass-selected ions using a reflectron mass spectrometer I. Development of an apparatus and application to Mg⁺-Ar," *Chem. Phys. Lett.* **2015**, *630*, 111–115.

- 37. Duncan, M. A. "Laser vaporization cluster sources," Rev. Sci. Inst. 2012, 83, 041101.
- 38. Townsend, D.; Minitti, M. P.; Suits, A. G. "Direct current slice imaging," *Rev. Sci. Inst.* **2003**, *74*, 2530–2539.
- 39. Li, W.; Chambreau, S. D.; Lahankar, S. A.; Suits, A. G. "Megapixel ion imaging with standard video," *Rev. Sci. Instr.* **2005**, *76*, 063106/. See also NuAcq 0.9 software, Suits, A. G., http://chem.wayne.edu/suitsgroup/NuAcq.html.
- 40. Moseley, J. T.; Saxon, R. P.; Huber, B. A.; Cosby, P. C.; Abouaf, R.; Tadjeddine, M. "Photofragment spectroscopy and potential curves of Ar₂⁺," *J. Chem. Phys.* **1977**, *67*, 1659–1668.
- 41. Zhao, Y.; Truhlar, D. G. "A new local density functional for main-group thermochemistry, transition metal bonding, thermochemical kinetics, and noncovalent interactions," *J. Chem. Phys.* **2006**, *125*, 194101.
- 42. Gaussian 09, Revision D.01, M. J. Frisch, et al., Gaussian, Inc., Wallingford, CT, 2009.
- 43. Suits, A. G.; Miller, R. L.; Bontuyan, L. S.; Houston, P. L. "Photofragment vector correlations by ion imaging: O₂ [a $^{1}\Delta_{g}(v,J)$] from 248 nm dissociation of ozone," *J. Chem. Soc., Faraday Trans.* **1993**, 89, 1443-1447.
- 44. Armentrout, P. B., private communication.

CHAPTER 5

PHOTODISSOCIATION OF THE HYDRONIUM-ARGON CATION

Introduction

The solvated proton and proton transfer reactions have been implicated in countless processes in Chemistry and Biology. ¹⁻¹³ Proton transfer is described by the Grotthus mechanism in which protons are thought to be transferred by alternation between Eigen and Zundel states of protonated water in bulk solution. ¹⁰⁻¹³ For this reason, the structure and binding energies of protonated water clusters and their noble gas adducts have been thoroughly investigated. ¹⁴⁻²⁴ The infrared spectra of H₃O⁺Ar and other small clusters are of particular interest as it is possible that a complete understanding of their vibrational couplings may lead to a better understanding of the broad bands observed for aqueous solutions. ²³

Structural studies of gas-phase protonated water clusters typically employed vibrational predissociation spectroscopy and messenger atom tagging techniques. $^{14-15,16-21,23}$ H⁺(H₂O)_nA (A = He, Ar, H₂) clusters were vibrationally excited, leading to elimination of the messenger atom A, and the mass spectral signal corresponding to loss of A was monitored as a function of the photon energy. This data provides relative cross sections for the elimination A, which are analogous to the infrared spectra of the bare H⁺(H₂O)_n clusters.

Experimental binding energies for protonated water clusters are also important.²⁵⁻³¹ Early experiments relied on equilibrium measurements in high pressure mass spectrometers.²⁵⁻²⁷ More modern approaches include monitoring metastable decay by mass-analyzed ion kinetic energy spectroscopy or collision-induced dissociation.²⁸⁻³² In either case, H⁺(H₂O)_n clusters must

fragment as a result of vibrational excitation. Bond breaking and energy transfer in vibrationally excited molecules is governed in part by intramolecular vibrational relaxation, a process by which vibrational energy is redistributed among the vibrational modes of a molecule through their anharmonic couplings. RRKM and phase space theories, as well as other theories of unimolecular reaction rates, usually assume that this redistribution of energy be statistical. Energy is randomized over all degrees of freedom and each mode is sampled ergodically, eventually leading to cleavage of the weakest bond. Indeed, this a fundamental principle of the messenger atom tagging technique discussed previously.

However, there are notable examples in which the assumption of ergodicity does not hold. Crim and coworkers studied the overtone excitation of HOOH or HOOD, which led to cleavage of the O–O bond. 37-38 Laser induced fluorescence detection revealed that the distribution of excess kinetic energy in the rotations of the OH and OD fragments was non-statistical, suggesting that vibrational energy is not completely randomized in the parent molecule before dissociation. Reisler and coworkers have used vibrational predissociation spectroscopy and velocity map imaging techniques to study weakly bound dimers of small molecules. 39-47 In the case of the neutral water dimer, they observed a non-statistical distribution of rotational energy in the monomer fragments following excitation of the intermolecular O–H stretch and dissociation. 44 In addition, they reported that one of the monomers is preferentially produced with one quantum in the bending mode and extensive rotational excitation. This is consistent with the momentum gap law in which fragments are generated in final states with minimal translational excitation. 39,44,48

Here we report similar observations for the infrared dissociation of H_3O^+Ar using selected-ion velocity map imaging. H_3O^+Ar is dissociated by excitation of either the O–H

stretch corresponding to motion of the shared proton (3134 cm $^{-1}$) or the remote O–H stretch localized on the H_3O^+ moiety (3498 cm $^{-1}$). Although the remote O–H stretch is 364 cm $^{-1}$ higher in energy, the diameter of the image of H_3O^+ following excitation to this mode is smaller than that for excitation at lower energy. The possible explanations for this behavior are discussed.

Experimental

The experimental apparatus is described in Chapter 2. $H^+(H_2O)_n$ and $H^+(H_2O)_nAr$ clusters are produced by pulsed electrical discharge in a supersonic expansion (110 psi, 10% H_2 in Ar). The O–H stretch of mass-selected H_3O^+Ar ions is excited with the tunable output of a KTP/KTA OPO/OPA system (LaserVision, 1-10 mJ/pulse, vertical polarization) pumped by an Nd:YAG laser (Continuum Precision 8010). Vibrationally excited H_3O^+Ar dissociates by loss of Ar and the H_3O^+ ion is detected. The arrival time distribution of H_3O^+ (200 ns) is not sufficiently broad for sliced imaging so the entire distribution is collected. The detector is operated with a 250 ns gate to eliminate background ion signals, and images are built up over 100,000 laser shots at each wavelength. The NuAcq software was used for data acquisition and images are processed using BasisFit and ImageJ. Photodissociation of Ar_2^+ at 355 nm is used for calibration of the detector area. 50

Results and Discussion

The image corresponding to photodissociation of H_3O^+Ar at 3134 cm⁻¹ is shown in Figure 1. It is clear upon visual inspection that the angular distribution of H_3O^+ is isotropic ($\beta \approx 0$). This is not surprising considering that the lifetime of the excited vibrational state is likely longer than the rotational period of the parent ion. The total kinetic energy distribution for dissociation at 3134 cm⁻¹ is shown in Figure 2.

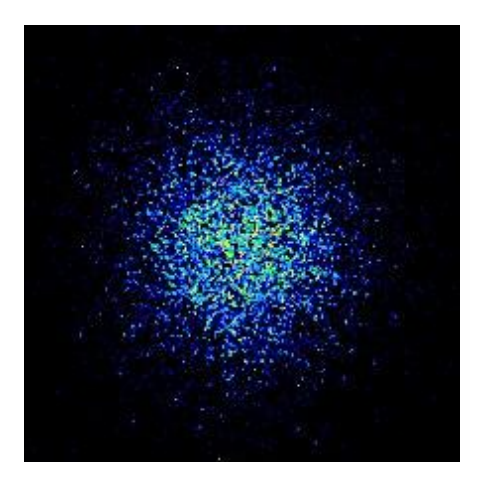


Figure 1. Photofragment image of H_3O^+ corresponding to photodissociation of H_3O^+Ar at 3134 cm⁻¹.

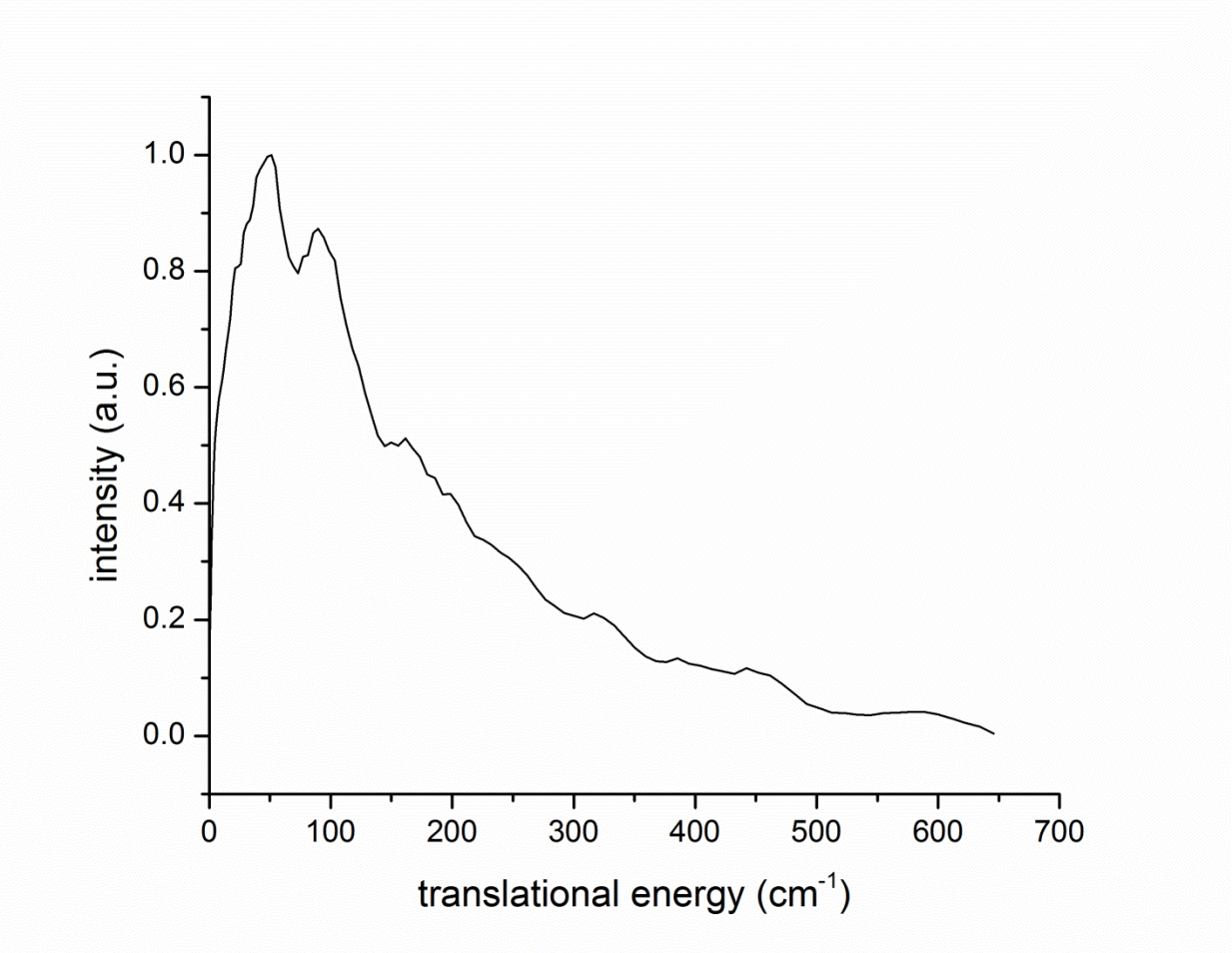


Figure 2. Total kinetic energy distribution for photodissociation of H_3O^+Ar at 3134 cm $^{-1}$.

The apparent maximum kinetic energy is 600 cm⁻¹. The theoretical binding energy of H₃O⁺Ar is $1900 \text{ cm}^{-1.24}$ Assuming this value is accurate, there should be $3134 - 1900 = 1234 \text{ cm}^{-1}$ available for internal excitation of the H₃O⁺ fragment. This is not enough to excite the symmetric (3440 cm⁻¹) or asymmetric (3527 cm⁻¹) O–H stretches of H₃O⁺. ²³ Likewise, there is insufficient energy available for excitation of the bending mode (1632 cm⁻¹). However, there is enough energy left to excite the umbrella vibration of H₃O⁺, analogous to that of NH₃, which has levels at 526 and 954 cm $^{-1}$ due to a large tunneling splitting. ⁵¹ Therefore it is possible that H_3O^+ is produced with one or two quanta in this vibrational mode and the remaining energy is converted into rotational energy. Of course it is also possible that H_3O^+ is not produced in an excited vibrational state and all available energy is converted to rotational excitation. This would be consistent with an impulsive interaction in which the excited H₃O⁺Ar accesses a repulsive region of the potential energy surface and all vibrational energy is converted into rotational and translational energy.⁴³-⁴⁴ In this case, rotational excitation would likely be favored. The structure of H₃O⁺Ar is bent, and dissociation would produce torque with an angular momentum vector perpendicular to the H₂OH⁺-Ar coordinate. Excluding vibrational excitation, this would result in a velocity-rotation correlation.⁵² Therefore, dissociation of H₃O⁺Ar at higher energy should simply lead to a higher degree of rotational excitation in H_3O^+ .

The photofragment image and total kinetic energy distribution corresponding to photodissociation of H_3O^+Ar at 3498 cm⁻¹ are shown in Figure 3 and Figure 4. Again, it is clear upon visual inspection that the angular distribution of H_3O^+ is isotropic ($\beta \approx 0$) as expected. The total kinetic energy distribution for dissociation at 3498 cm⁻¹ is shown in Figure 3. The apparent maximum kinetic energy is 500 cm⁻¹, 100 cm⁻¹ less than that for dissociation at 3134 cm⁻¹.

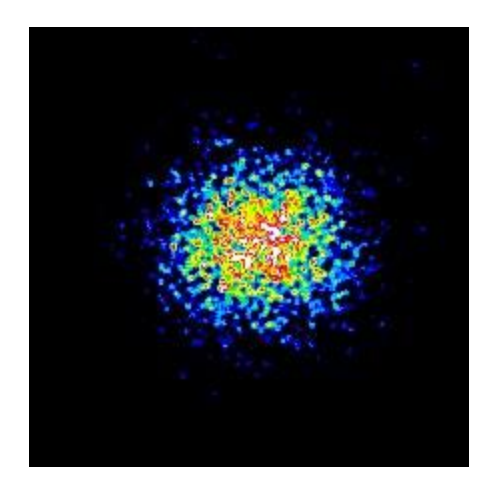


Figure 3. Photofragment image of H_3O^+ corresponding to photodissociation of H_3O^+Ar at 3498 cm⁻¹.

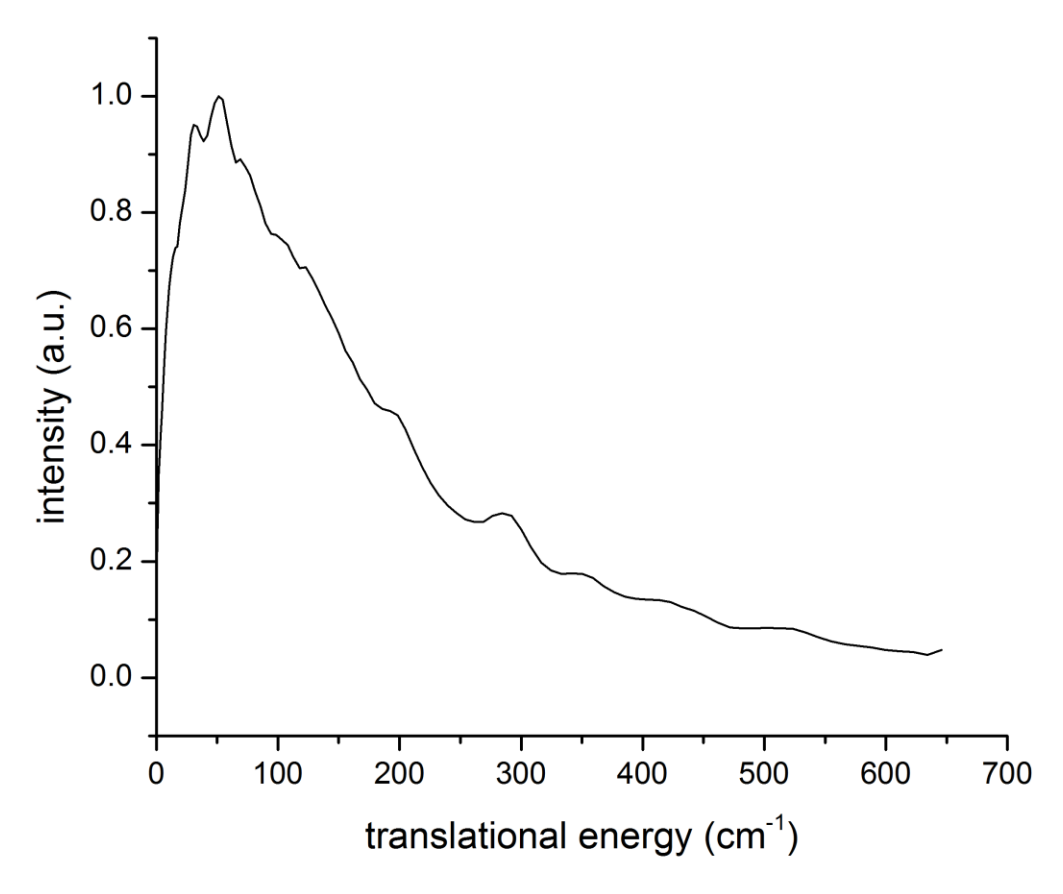


Figure 4. Total kinetic energy distribution for photodissociation of $\mathrm{H_3O^+Ar}$ at 3498 cm⁻¹.

Assuming a binding energy of 1900 cm^{-1} , there should be $3498 - 1900 = 1598 \text{ cm}^{-1}$ available for internal excitation of the H_3O^+ fragment. This is still only enough energy to excite the umbrella vibration of H_3O^+ at 526 and 954 cm^{-1} with the remaining energy going into rotational excitation. The difference between photodissociation energies is only 364 cm^{-1} , far smaller than the energies of the H_3O^+ vibrations. Therefore, the additional excess energy resulting from dissociation at 3498 cm^{-1} can only go into translation or rotation of H_3O^+ . Since the radius of the image for dissociation at 3498 cm^{-1} is smaller than that for 3134 cm^{-1} , this additional energy must be converted into rotational energy. It is still possible that nearly all excess kinetic energy is converted into rotational energy, and we are simply observing higher degrees of rotational excitation for higher vibrational excitation energies. An additional possibility is that dissociation via excitation of the shared proton mode proceeds at a faster rate, and the rate of dissociation via the remote O-H stretch is limited by intramolecular vibrational relaxation. Although our experimental resolution prevents us from distinguishing between these mechanisms, detailed modeling of this system could aid our understanding of these complex dynamics.

Conclusion

The infrared photodissociation of H₃O⁺Ar has been investigated at 3134 and 3498 cm⁻¹. The angular distribution of H₃O⁺ is isotropic for both wavelengths, consistent with indirect dissociation of H₃O⁺Ar. Although, vibrational and rotational excitation of the H₃O⁺ fragment cannot be distinguished at the available resolution, dissociation at higher energy appears to lead to higher degrees of rotational excitation.

References

- 1. Heberle, J.; Riesle, J.; Thiedemann, G.; Oesterhelt, D.; Dencher, N. A. "Proton migration along the membrane surface and retarded surface to bulk transfer," *Nature* **1994**, *370*, 379-382.
- 2. Borgis, D.; Hynes, J. T. "Curve crossing formulation for proton transfer reactions in solution," *J. Phys. Chem.* **1996**, *100*, 1118-1128.
- Stowell, M. H. B.; McPhillips, T. M.; Rees, D. C.; Soltis, S. M.; Abresch, E.; Feher, G.
 "Light-induced structural changes in photosynthetic reaction center: Implications for mechanism of electron-proton transfer," *Science* 1997, 276, 812-816.
- 4. Waldmann, R.; Champigny, G.; Bassilana, F.; Heurteaux, C.; Lazdunski, M. "A protongated cation channel involved in acid-sensing," *Nature* **1997**, *386*, 173-177.
- Luecke, H.; Richter, H.-T.; Lanyi, J. K. "Proton transfer pathways in bacteriorhodopsin at 2.3 Angstrom resolution," *Science* 1998, 280, 1934-1937.
- 6. Chen, K.; Hirst, J.; Camba, R.; Bongagura, C. A.; Stout, C. D.; Burgess, B. K.; Armstrong, F. A. "Atomically defined mechanism for proton transfer to a buried redox centre in a protein," *Nature*, **2000**, *405*, 814-817.
- Stenger, J.; Madsen, D.; Dreyer, J.; Nibbering, E. T. J.; Hamm, P.; Elsaesser, T.
 "Coherent response of hydrogen bonds in liquids probed by ultrafast vibrational spectroscopy," *J. Phys. Chem. A* 2001, 105, 2929-2932.
- 8. Nibbering, E. T. J.; Elsaesser, T. "Ultrafast vibrational dynamics of hydrogen bonds in the condensed phase," *Chem. Rev.* **2004**, *104*, 1887-1914.

- 9. Ashihara, S.; Huse, N.; Espagne, A.; Nibbering, E. T. J.; Elsaesser, T. "Ultrafast structural dynamics of water induced by dissipation of vibrational energy," *J. Phys. Chem. Lett. A* **2007**, *111*, 743-746.
- 10. von Grotthus, C. J. D. "Mémoire sur la decomposition de l'eau et de corps qu'elle tien en dissolution à l'aide de l'électricité galvanique," *Ann. Chim.* **1806**, *58*, 54-74.
- 11. Eigen, M.; de Maeyer, L. "Self-dissociation and protonic charge transport in water and ice," *Proc. R. Soc. London* **1958**, *247*, 505-533.
- 12. Eigen, M. "Proton transfer, acid-base catalysis, and enzymatic hydrolysis. Part I: Elementary processes," *Angew. Chem. Int. Ed. Engl.* **1964**, *3*, 1-19.
- 13. Schuster, P.; Zundel, G.; Sandorfy, C., Eds. *The Hydrogen Bond. Recent Developments in Theory and Experiments*; North-Holland, Amsterdam, NL 1976.
- 14. Okumura, M.; Yeh, L. I.; Myers, J. D.; Lee, Y. T. "Infrared spectra of the cluster ions $H_7O_3^{+\bullet}H_2$ and $H_9O_4^{+\bullet}H_2$," *J. Chem. Phys.* **1986**, *85*, 2328-2329.
- 15. Yeh, L. I.; Okumura, M.; Myers, J. D.; Price, J. M.; Lee, Y. T. "Vibrational spectroscopy of the hydrated hydronium cluster ions $H_3O^{+\bullet}(H_2O)_n$ (n = 1, 2, 3)," *J. Chem. Phys.* **1989**, 91, 7319-7330.
- Asmis, K. R.; Pivonka, N. L.; Santambrogio, G.; Brümmer, M.; Kaposta, C.; Neumark,
 D. M.; Wöste, L. "Gas-phase infrared spectrum of the protonated water dimer," *Science* 2003, 299, 1375-1377.
- 17. Heine, N.; Asmis, K. R. "Cryogenic ion tap vibrational spectroscopy of hydrogen-bonded clusters relevant to atmospheric chemistry," *Int. Rev. Phys. Chem.* **2015**, *34*, 1-34.

- 18. Shin, J.-W.; Hammer, N. I.; Diken, E. G.; Johnson, M. A.; Walters, R. S.; Jaeger, T. D.; Duncan, M. A.; Christie, R. A.; Jordan, K. D. "Infrared signature of structures associated with the H⁺(H₂O)_n (n = 6 to 27) clusters," *Science* **2004**, *304*, 1137-1140.
- 19. Headrick, J. M.; Diken, E. G.; Walters, R. S.; Hammer, N. I.; Christie, R. A.; Cui, J.; Myshakin, E. M.; Duncan, M. A.; Johnson, M. A.; Jordan, K. D. "Spectral signatures of hydrated proton vibrations in water clusters," *Science* 2005, 308, 1765-1769.
- 20. Wolke, C. T.; Fournier, J. A.; Dzugan, L. C.; Fagiani, M. R.; Odbadrakh, T.; Knorke, H.; Jordan, K. D.; McCoy, A. B.; Asmis, K. R.; Johnson, M. A. "Spectroscopic snapshots of the proton-transfer mechanism in water," *Science* **2016**, *354*, 1131-1135.
- 21. Douberly, G. E.; Walters, R. S.; Cui, J.; Jordan, K. D.; Duncan, M. A. "Infrared spectroscopy of small protonated water clusters, H⁺(H₂O)_n (n = 2–5)," *J. Phys. Chem. A* **2010**, *114*, 4570-4579.
- 22. Grandinetti, F. "Gas-phase ion chemistry of the noble gases: Recent advances and future prospectives," *Eur. J. Mass Spectrom.* **2011**, *17*, 423-463.
- 23. Li, J.-W.; Morita, M.; Takahashi, K.; Kuo, J.-L. "Features in vibrational spectra induced by Ar-tagging for $H_3O^+Ar_m$, m = 0-3," *J. Phys. Chem. A* **2015**, *119*, 10887-10892.
- 24. Borocci, S.; Cecchi, P.; Giordani, M.; Grandinetti, F. "Complexes of noble gases with H₃O⁺: A theoretical investigation of Ng(H₃O⁺) (Ng = He–Xe)," *Eur. J. Mass Spectrom.* **2015**, *21*, 171-181.
- 25. Kebarle, P.; Searles, S. K.; Zolla, A.; Scarborough, J.; Arshadi, M. "Solvation of the hydrogen ion by water molecules in the gas phase. Heats and entropies of solvation of individual reactions: H⁺(H₂O)_{n-1} + H₂O → H⁺(H₂O)_n," *J. Am. Chem. Soc.* 1967, 89, 6393-6399.

- 26. Cunningham, A. J.; Payzant, J. D.; Kebarle, P. "Kinetic study of the proton hydrate H⁺(H₂O)_n equilibriums in the gas phase," *J. Am. Chem. Soc.* **1972**, *94*, 7627-7632.
- 27. Lau, Y. K.; Ikuta, S.; Kebarle, P. "Thermodynamics and kinetics of the gas-phase reactions $H_3O^+(H_2O)_{n-1}$ + water = $H_3O^+(H_2O)_n$," *J. Am. Chem. Soc.* **1982**, *104*, 1462-1469.
- 28. Magner, T. F.; David, D. E.; Michl, J. "The first twenty-eight gas-phase proton hydration energies," *Chem. Phys. Lett.* **1991**, *182*, 363-370.
- 29. Dalleska, N. F.; Honma, K.; Armentrout, P. B. "Stepwise solvation enthalpies of protonated water clusters: Collision-induced dissociation as an alternative to equilibrium studies," *J. Am. Chem. Soc.* **1993**, *115*, 12125-12131.
- 30. Engelking, P. C. "Photoinduced evaporation of charged clusters," *J. Chem. Phys.* **1986**, 85, 3103-3110.
- 31. Engelking, P. C. "Determination of cluster binding energy from evaporative lifetime and average kinetic energy release: Application to $(CO_2)_n^+$ and Ar_n^+ clusters," *J. Chem. Phys.* **1987**, 87, 936-940.
- 32. Bruzzi, E.; Parajuli, R.; Stace, A. J. "Binding energies determined from kinetic energy release measurements following the evaporation of single molecules from the molecular clusters H⁺(H₂O)_n, H⁺(NH₃)_n, and H⁺(CH₃OH)_n," *Int. J. Mass. Spectrom.* **2013**, *345/346/347*, 160-166.
- 33. Baer, T.; Hase, W. L. *Unimolecular Reaction Dynamics*; Oxford University Press, New York, USA 1996.

- 34. Atrill, S.; Mouhandes, A.; Winkel, J. F.; Goren, A.; Stace, A. J. "Energy portioning following the IR photofragmentation of SF₆•(NO)⁺ cluster ions," *Faraday Discuss.* **1995**, *102*, 339-351.
- 35. Atrill, S.; Stace, A. J. "Energy partitioning following the infrared photofragmentation of SF₆•(C₆H₆)⁺ cluster ions," *Int. J. Mass Spectrom.* **1998**, *179/180*, 253-260.
- 36. Atrill, S.; Stace, A. J. "Vibrational relaxation in infrared excited SF₆•Ar_n⁺ cluster ions," *J. Chem. Phys.* **1998**, *108*, 1924-1931.
- 37. Rizzo, T. R.; Hayden, C. C.; Crim, F. F. "Product energy partitioning in the decomposition of state-selectively excited HOOH and HOOD," *Faraday Discuss. Chem. Soc.* **1983**, *75*, 223-237.
- 38. Rizzo, T. R.; Hayden, C. C.; Crim, F. F. "State-resolved product detection in the overtone vibration initiated unimolecular decomposition of HOOH(6*v*_{OH})," *J. Chem. Phys.* **1984**, *81*, 4501-4509.
- 39. Pritchard, M.; Parr, J.; Li, G.; Reisler, H.; McCaffery, A. J. "The mechanism of H-bond rupture: the vibrational pre-dissociation of C₂H₂–HCl and C₂H₂–DCl," *Phys. Chem. Chem. Phys.* **2007**, *9*, 6241-6252.
- 40. Mollner, A. K.; Casterline, B. E.; Ch'ng, L. C.; Reisler, H. "Imaging the state-specific vibrational predissociation of the ammonia—water hydrogen-bonded dimer," *J. Phys. Chem. A* **2009**, *113*, 10174-10183.
- 41. Reisler, H. "Photofragment spectroscopy and predissociation dynamics of weakly bound molecules," *Annu. Rev. Phys. Chem.* **2009**, *60*, 39-59.

- 42. Casterline, B. E.; Mollner, A. K.; Ch'ng, L. C.; Reisler, H. "Imaging the state-specific vibrational predissociation of the hydrogen chloride–water hydrogen-bonded dimer," *J. Chem. Phys. A* **2010**, *114*, 9774-9781.
- 43. Rocher-Casterline, B. E.; Mollner, A. K.; Ch'ng, L. C.; Reisler, H. "Imaging H₂O photofragments in the predissociation of the HCl–H₂O hydrogen-bonded dimer," *J. Phys. Chem. A* **2011**, *115*, 6903-6909.
- 44. Ch'ng, L. C.; Samanta, A. K.; Czakó, G.; Bowman, J. M.; Reisler, H. "Experimental and theoretical investigations of energy transfer and hydrogen-bond breaking in the water dimer," *J. Am. Chem. Soc.* **2012**, *134*, 15430-15435.
- 45. Samanta, A. K.; Ch'ng, L. C.; Reisler, H. "Imaging bond breaking and vibrational energy transfer in small water containing clusters," *Chem. Phys. Lett.* **2013**, *575*, 1-11.
- 46. Mancini, J. S.; Samanta, A. K.; Bowman, J. M.; Reisler, H. "Experiment and theory elucidate the multichannel predissociation dynamics of the HCl trimer: Breaking up is hard to do," *J. Phys. Chem. A* **2014**, *118*, 8402-8410.
- 47. Samanta, A. K.; Cazkó, G.; Wang, Y.; Mancini, J. S.; Bowman, J. M. "Experimental and theoretical investigations of energy transfer and hydrogen-bond breaking in small water and HCl clusters," *Acc. Chem. Res.* **2014**, *47*, 2700-2709.
- 48. Ewing, G. E. "Selection rules for vibrational energy transfer: vibrational predissociation of van der Waals molecules," *J. Phys. Chem.* **1987**, *91*, 4662-4671.
- 49. Wagner, J. P.; McDonald, D. C.; Duncan, M. A., manuscript in preparation.
- 50. Moseley, J. T.; Saxon, R. P.; Huber, B. A.; Cosby, P. C.; Abouaf, R.; Tadjeddine, M. "Photofragment spectroscopy and potential curves of Ar₂⁺," *J. Chem. Phys.* **1977**, *67*, 1659-1668.

- 51. Liu, D.-J.; Haese, N. N.; Oka, T. "Infrared spectrum of the v_2 vibration-inversion band of H_3O^+ ," *J. Chem. Phys.* **1985**, 82, 5368-5372.
- 52. Suits, A. G.; Miller, R. L.; Bontuyan, L. S.; Houston, P. L. "Photofragment vector correlations by ion imaging: O₂ [a $^1\Delta_{\rm g}(v,J)$] from 248 nm dissociation of ozone," *J. Chem. Soc., Faraday Trans.* **1993**, 89, 1443-1447.

APPENDIX A CHAPTER 3 SUPPORTING INFORMATION

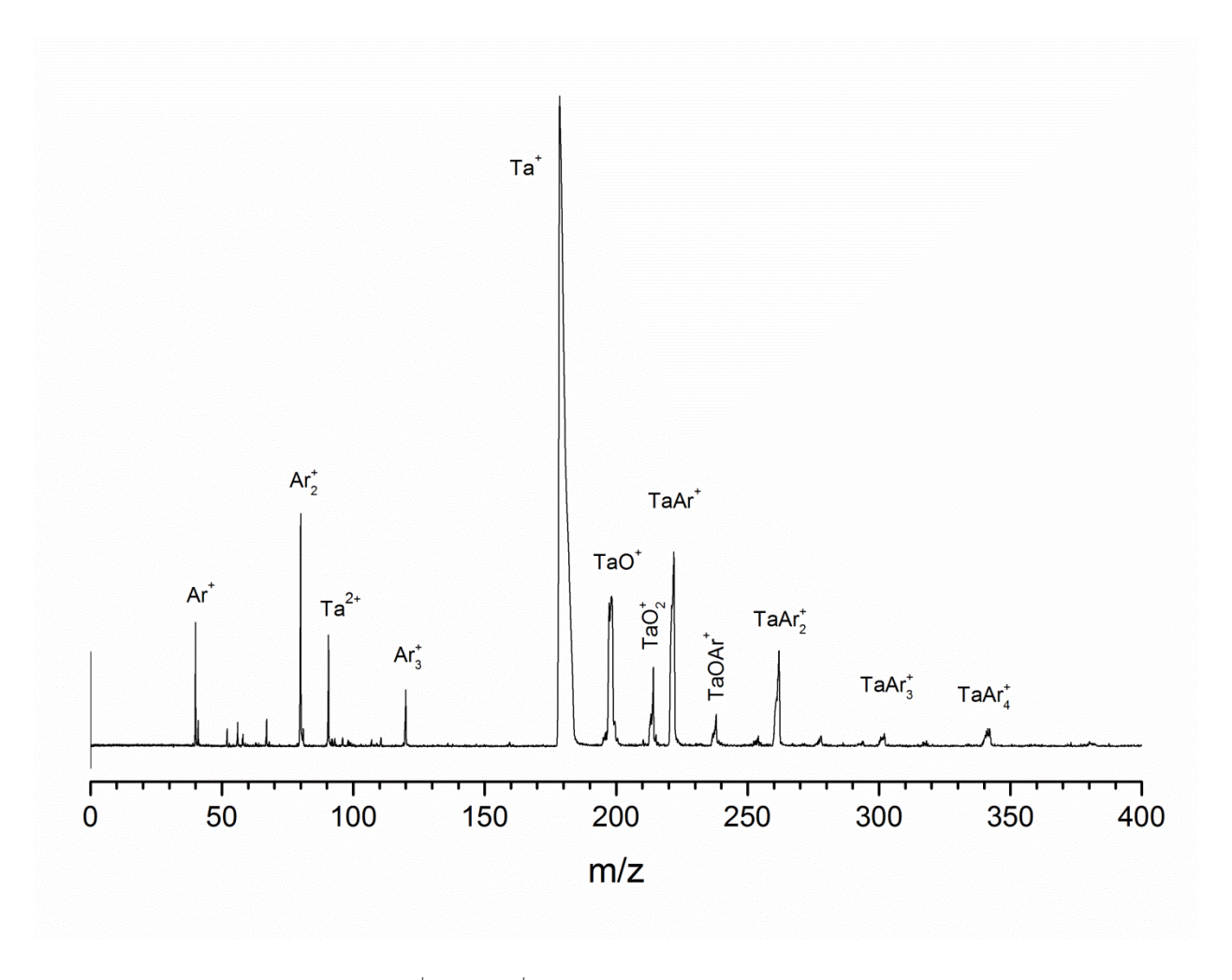


Figure 1. Mass spectrum of Ar_n^+ and $Ta^+(Ar)_n$ produced by laser spark at the surface of Ta rod with the spectrometer focused to low m/z.

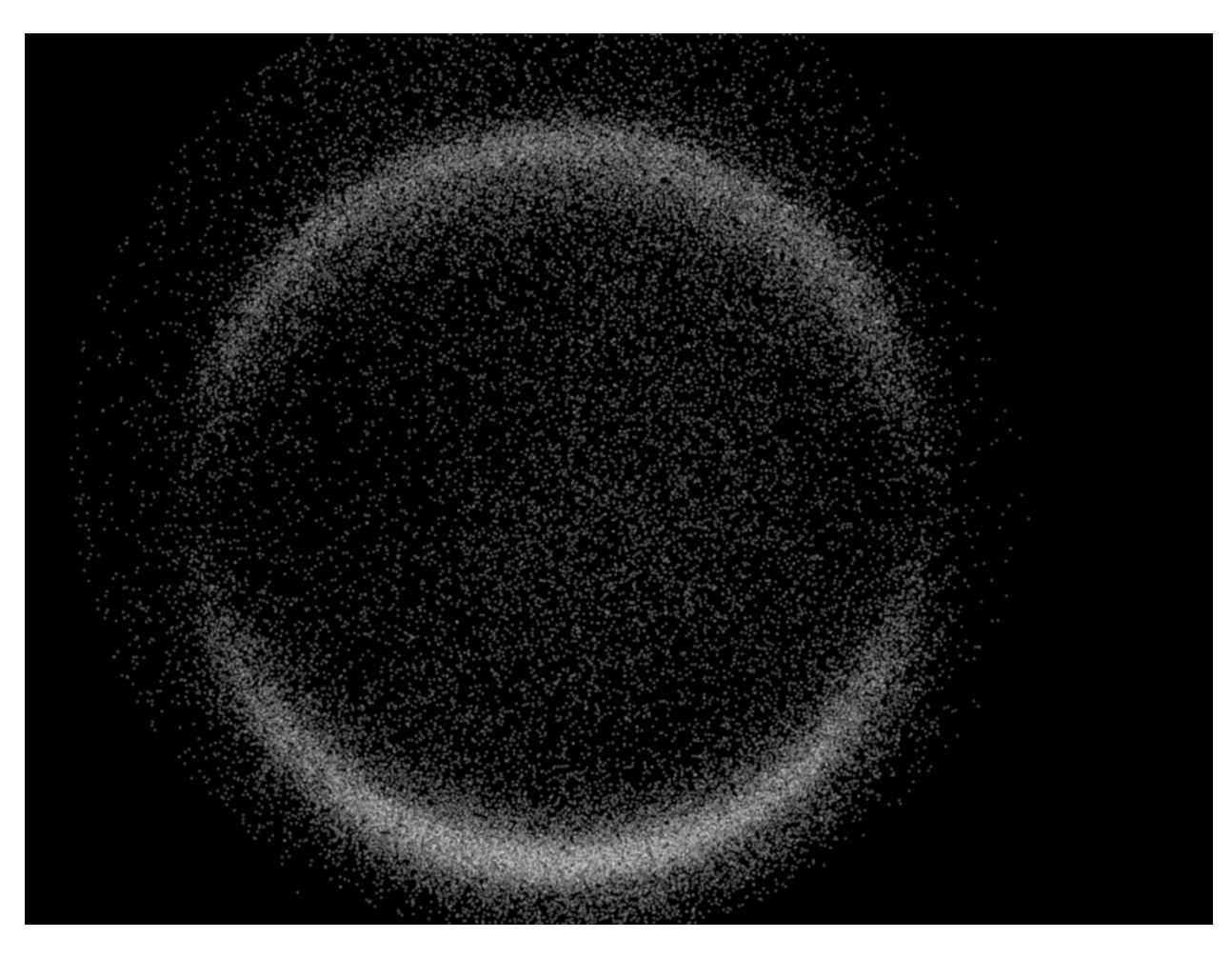


Figure 2. Raw image of Ar^+ from the photodissociation of Ar_2^+ at 355 nm.

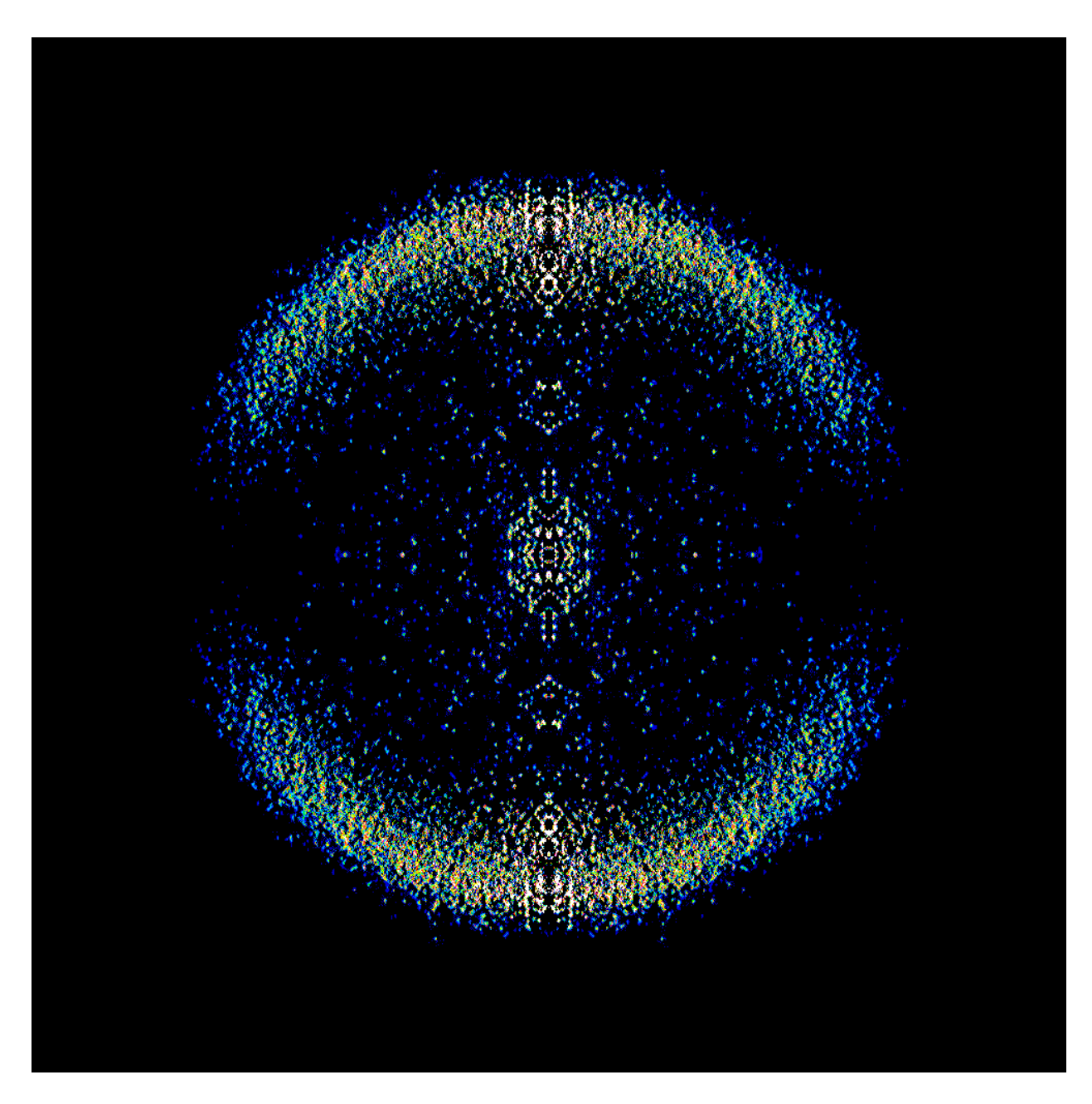


Figure 3. Image of Ar^+ from the photodissociation of Ar_2^+ at 355 nm reconstructed using BASEX.

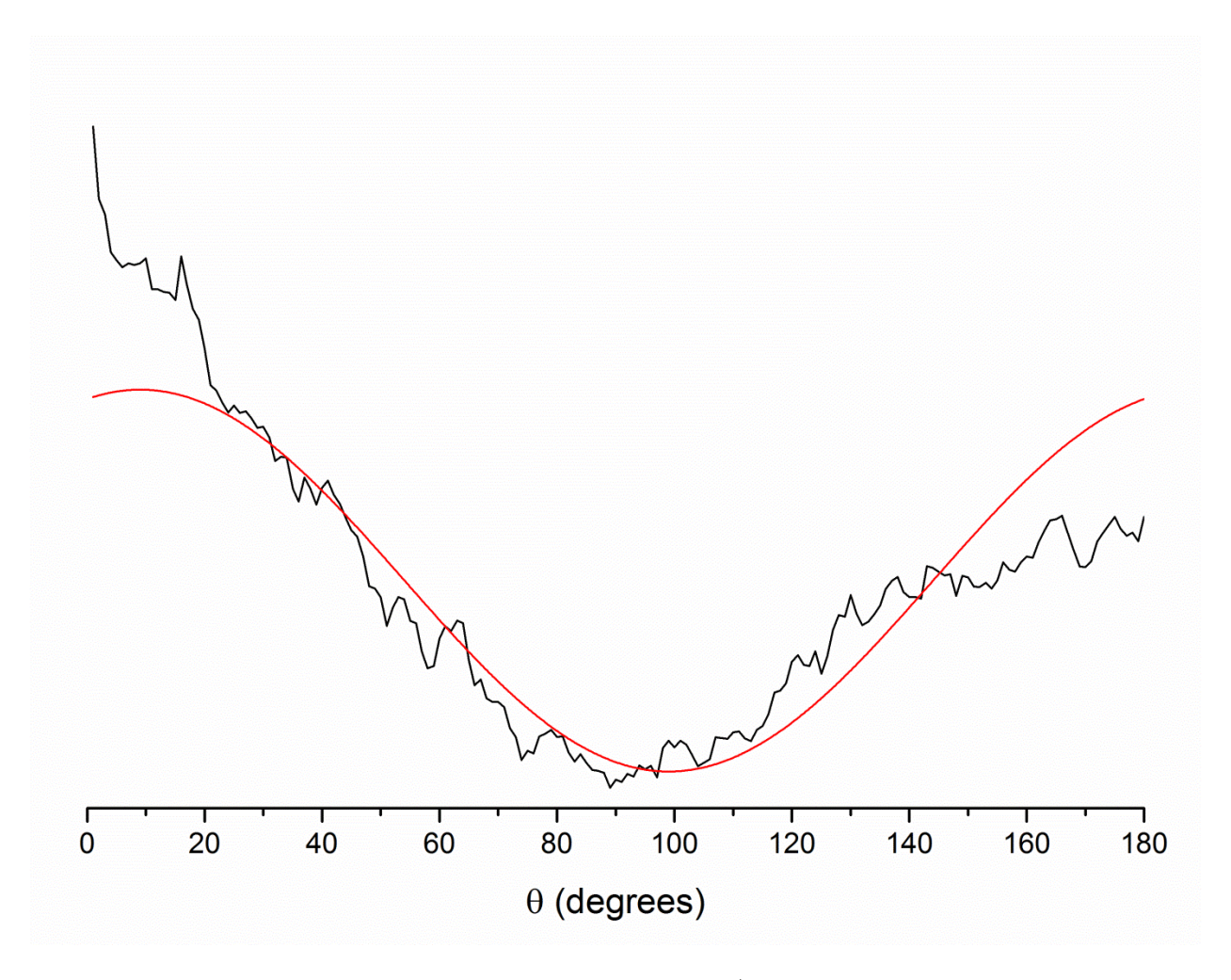


Figure 4. Angular distribution determined from the raw Ar⁺ image in Figure 2. The asymmetry arises because the raw image is more intense on the bottom hemisphere than it is on the top.

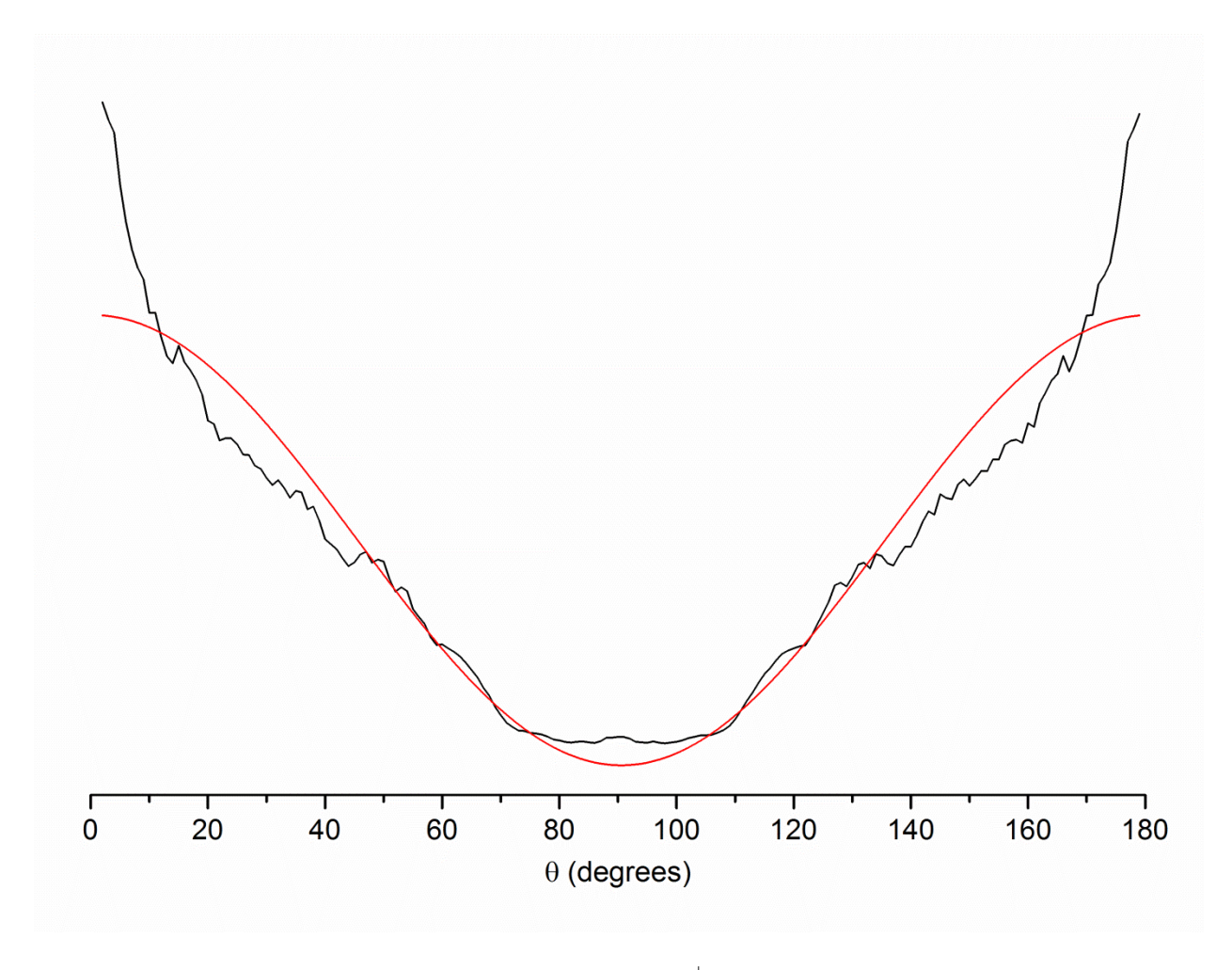


Figure 5. Angular distribution determined from the Ar⁺ image reconstructed using BASEX.

The following equation is used for fitting angular distributions:

$$I = \frac{A}{4\pi} \left\{ 1 + \frac{B}{2} \left[3\cos^2\left(\frac{\theta\pi}{180} - C\right) \right] \right\}$$

I is the signal intensity. The A parameter allows for variation of the amplitude, B is the β parameter, and C is a phase shift parameter correcting for rotation of the image.

Fitting the raw image results in significant asymmetry in the angular distribution, as shown in Figure 4. This arises becasue the image is brighter on its lower hemisphere than it is on its upper hemisphere. As shown in Table 1, this results in a β value of 0.56.

Table 1. Parameters for fitting the angular distribution of the raw Ar⁺ image.

A	A(error)	В	B(error)	C	C(error)	R^2
1.1763	0.013857	0.55724	0.023648	0.15798	0.018028	0.811

If the image is reconstructed with the BASEX program, cylindrical symmetry is imposed and this balances the intensities in the two hemispheres of the image, as shown in Figure 5. Fitting this image gives a β value of 1.71, as shown in Table 2.

Table 2. Parameters for fitting the angular distribution of the Ar⁺ image reconstructed using BASEX.

A	A(error)	В	B(error)	C	C(error)	R^2
639.33	12.554	1.7131	0.056695	0.010628	0.0097752	0.978

Another approach to balance the intensities of the two hemispheres of the image without changing the angular dependence is to reflect the image, using the reflection of one hemisphere to replace the other. This was done to produce the image in Figure 2 of Chapter 3. If this is done, fitting produces a β value of 1.95, as shown in Table 3.

Table 3. Parameters for fitting the angular distribution of the Ar^+ image generated by reflection of the upper portion of the raw Ar^+ image.

A	A(error)	В	B(error)	C	C(error)	R^2
119.09523	2.12321	1.95178	0.05512	0.01873	0.00779	0.958

APPENDIX B CHAPTER 4 SUPPORTING INFORMATION

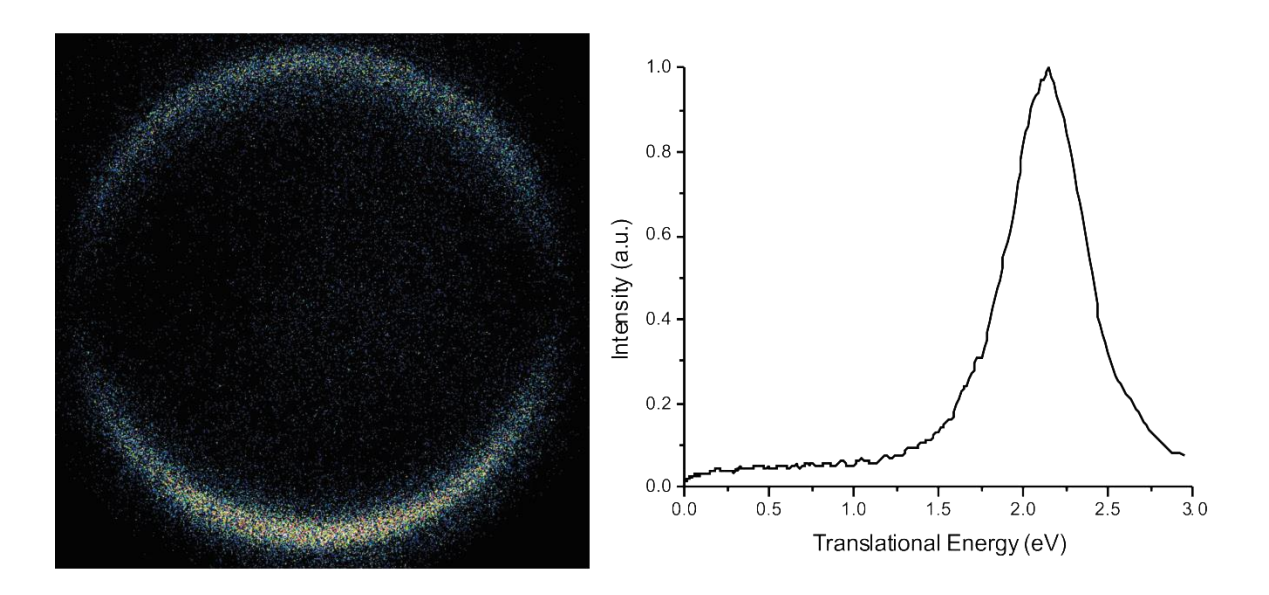


Figure 1. The image of Ar^+ from photodissociation of Ar_2^+ at 355 nm is shown on the left. The total kinetic energy distribution is shown on the right. The velocity and kinetic energy of Ar^+ based on D_0 "(Ar_2^+) = 1.33 eV (Chapter 4, Reference 41) is used to determine a velocity calibration factor for measuring the velocity of benzene⁺.

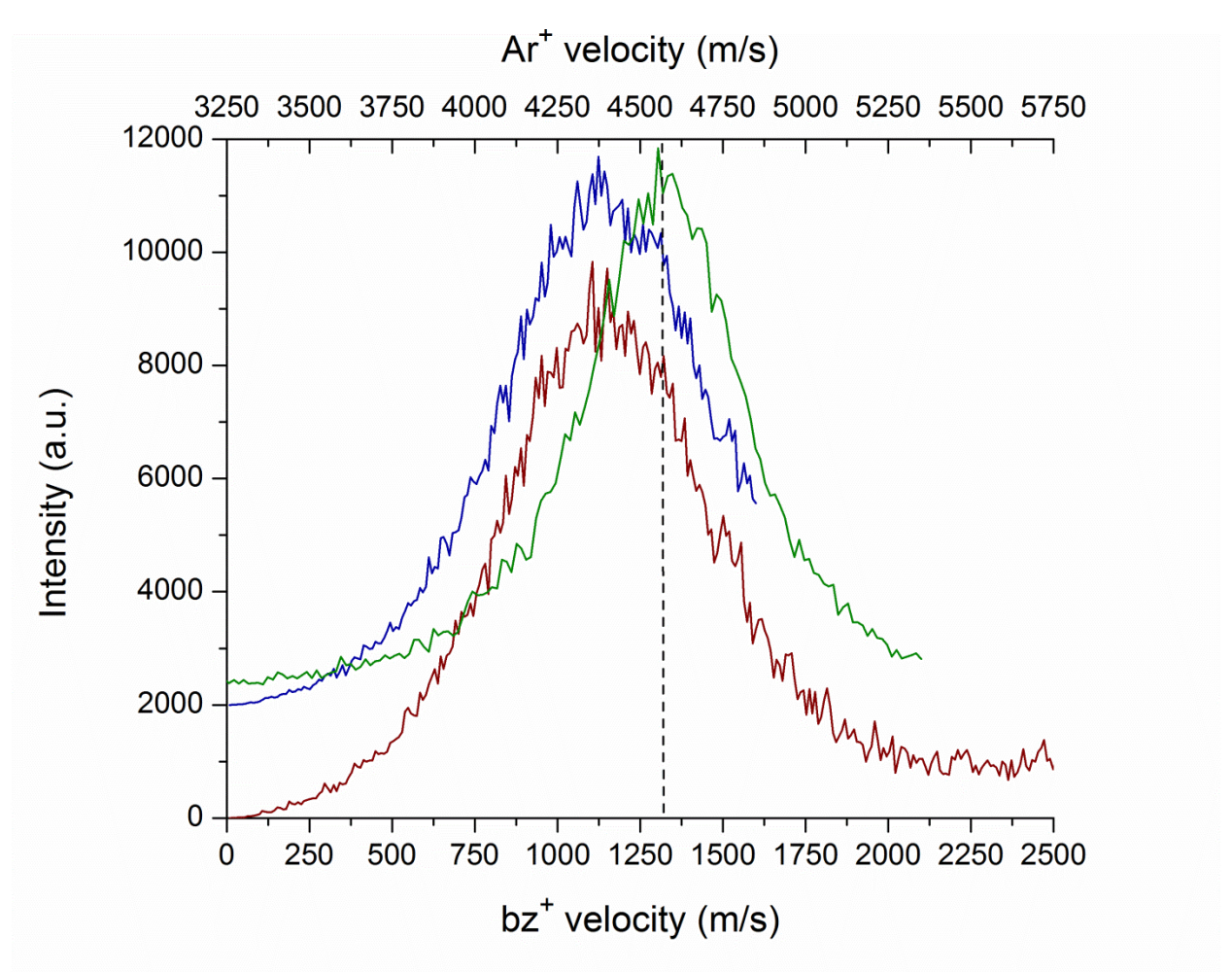


Figure 2. Velocity calibration for benzene $^+$ versus Ar^+ at 355 nm. The red curve represents the entire velocity distribution integrated to the edge of the detector. The blue curve is the same velocity distribution excluding background signal. The green curve is the velocity distribution of Ar^+ from photodissociation of Ar_2^+ at 355 nm. The width of the Ar^+ peak provides an upper limit on the velocity resolution of the instrument, and the half width can be used to determine the maximum velocity of benzene $^+$. The estimated uncertainty in velocity is 100 m/s based on the width of the Ar^+ velocity distribution. The benzene $^+$ velocity is 1315 \pm 100 m/s, and is indicated by the dashed line.

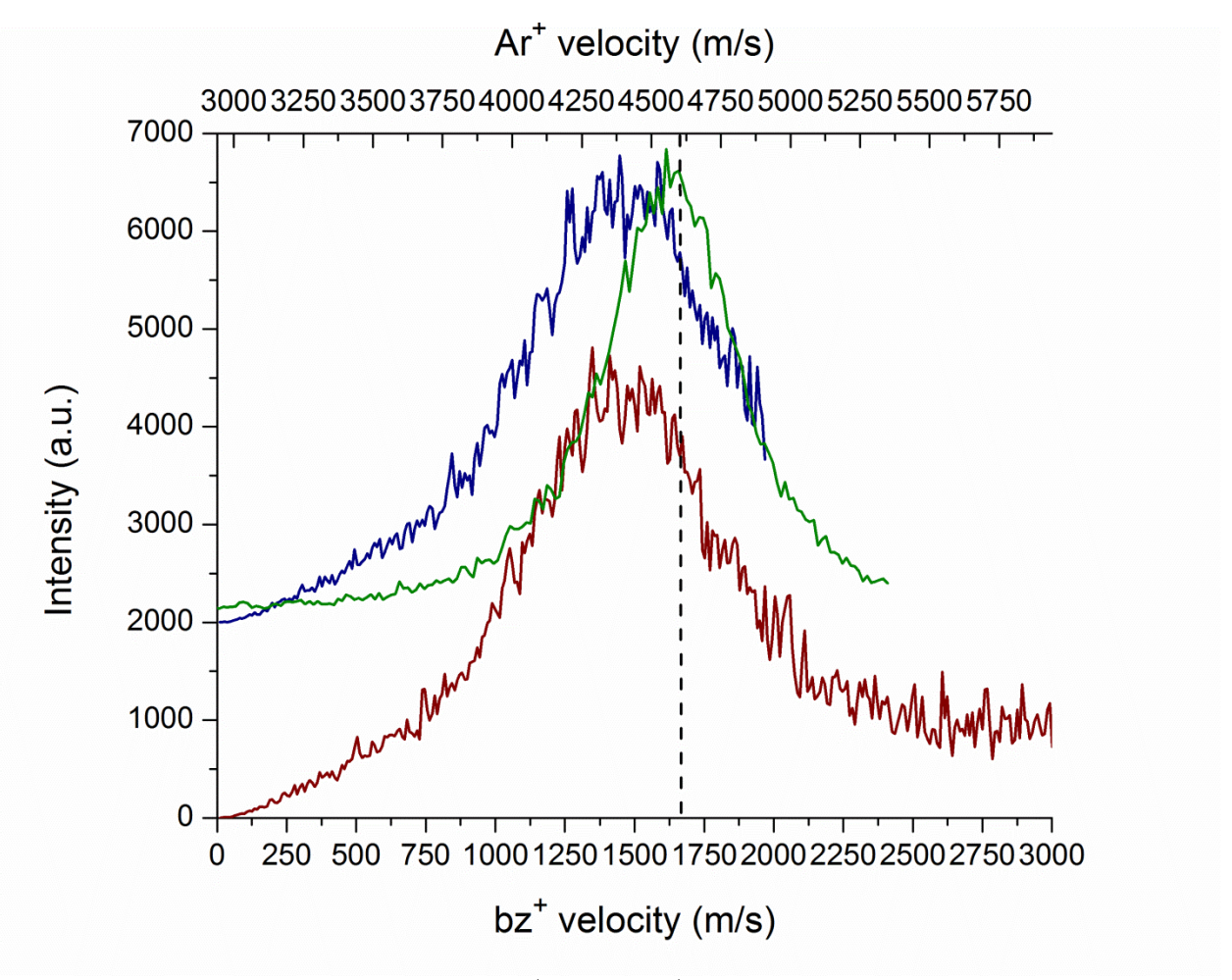


Figure 3. Velocity calibration for benzene $^+$ versus Ar^+ at 266 nm. The red curve represents the entire velocity distribution integrated to the edge of the detector. The blue curve is the same velocity distribution excluding background signal. The green curve is the velocity distribution of Ar^+ from photodissociation of Ar_2^+ at 355 nm. The width of the Ar^+ peak provides an upper limit on the velocity resolution of the instrument, and the half width can be used to determine the maximum velocity of benzene $^+$. The estimated uncertainty in velocity is 100 m/s based on the width of the Ar^+ velocity distribution. The benzene $^+$ velocity is 1684 \pm 100 m/s, and is indicated by the dashed line.

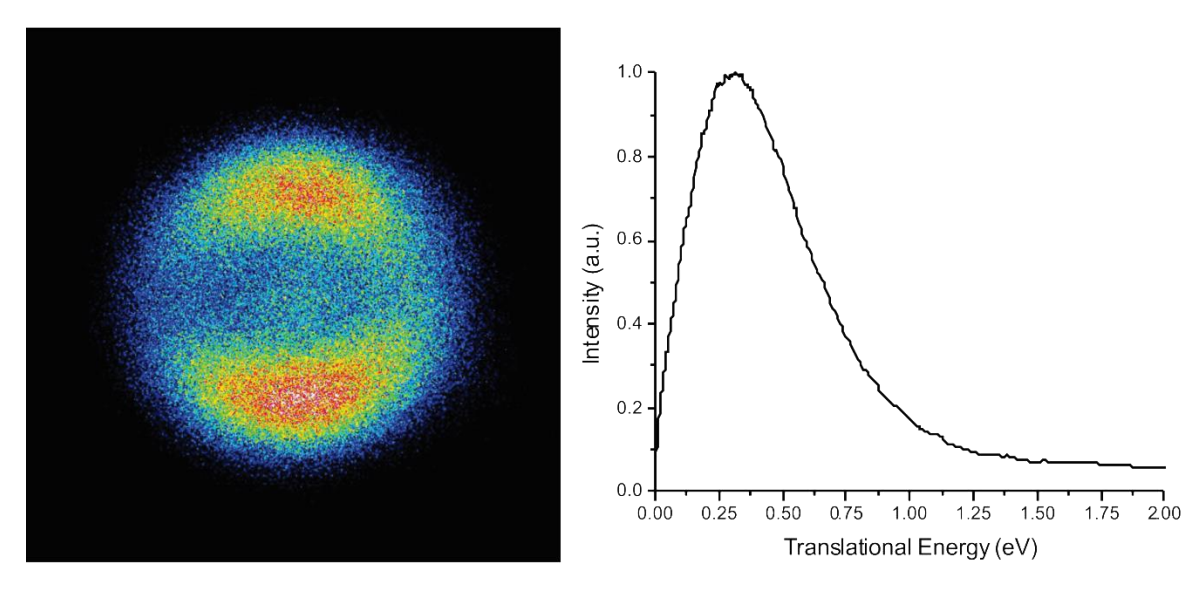


Figure 4. The image of benzene⁺ from photodissociation of Ag⁺(benzene) at 355 nm, generated in a helium expansion, is shown on the left. The total kinetic energy distribution is shown on the right. The image and energy distribution obtained under these conditions is much broader than the data obtained using an argon expansion, indicating that colder parent ions are generated using argon as a buffer gas.

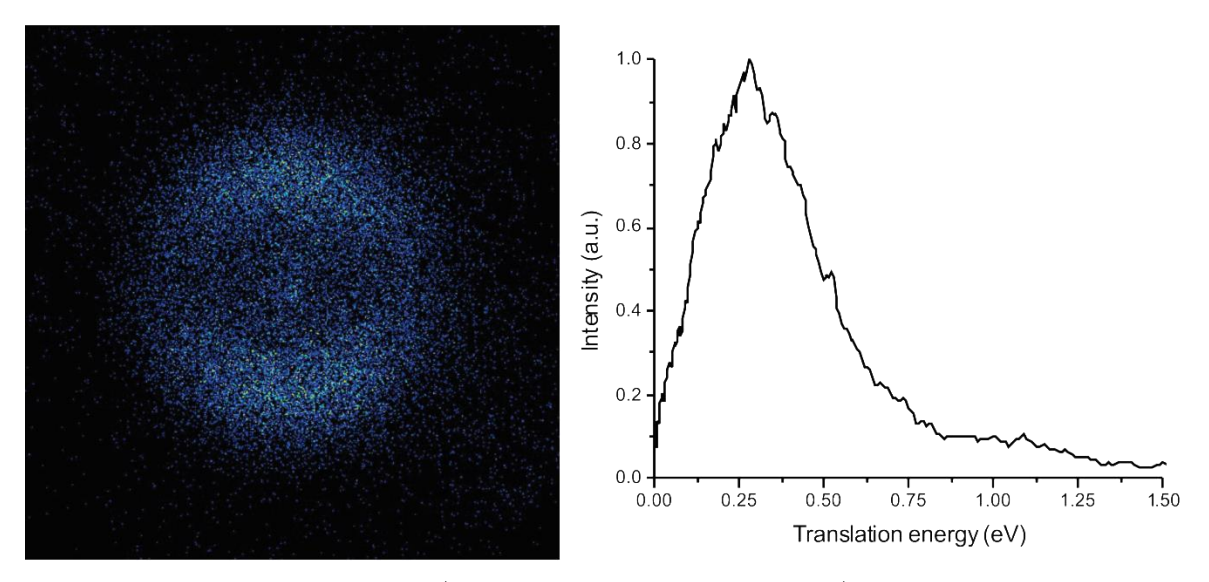


Figure 5. The image of benzene⁺ from photodissociation of Ag⁺(benzene) at 355 nm, generated in a carbon dioxide expansion, is shown on the left. The total kinetic energy distribution is shown on the right. The image and energy distribution obtained under these conditions is much broader than the data obtained using an argon expansion, indicating that colder parent ions are generated using argon as a buffer gas.

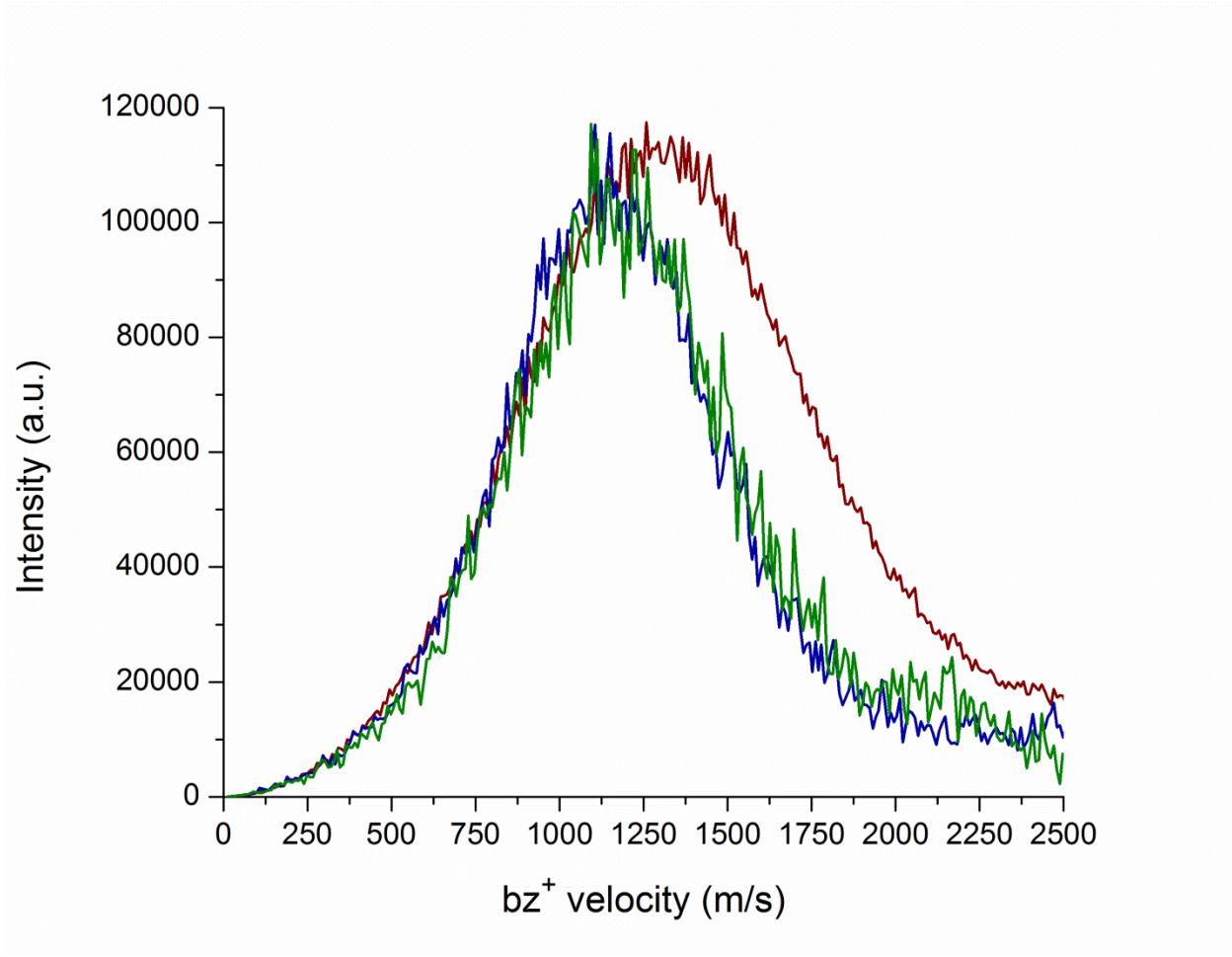


Figure 6. Velocity distributions of benzene⁺ from Ag⁺(benzene) generated in a helium expansion (red), a carbon dioxide expansion (green), and an argon expansion (blue). The velocity distribution obtained using the argon expansion is relatively narrow and shifted to lower velocity compared to the distribution obtained using a helium expansion, indicating that colder parent ions are generated using argon as a buffer gas.

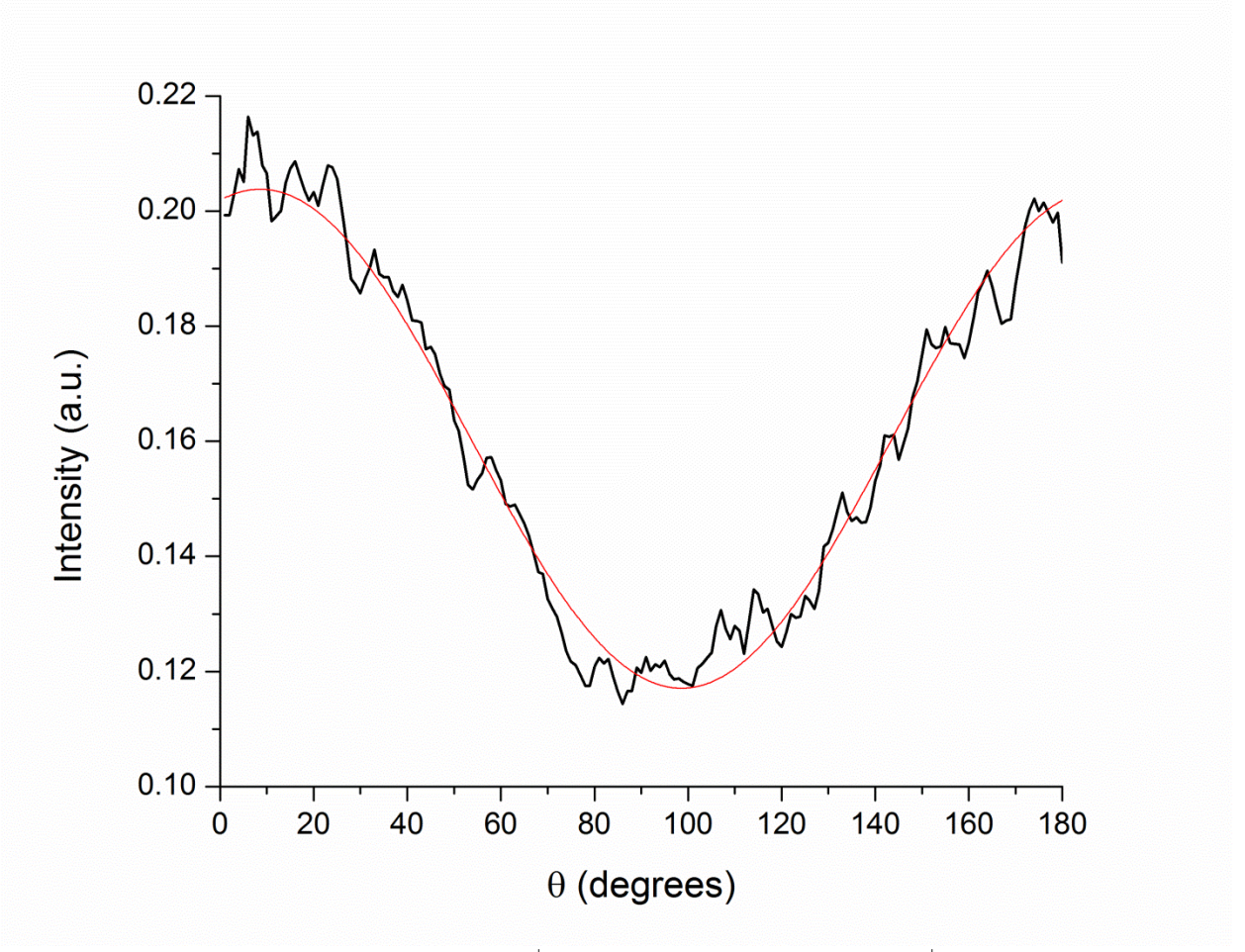


Figure 7. Angular distribution of benzene⁺ from photodissociation of Ag^+ (benzene) at 355 nm. The data was fit with the function below with amplitude *A* and phase shift *C*. β is the anisotropy parameter.

$$I(\theta) = \frac{A}{4\pi} [1 + \beta P_2(\cos(\theta - C))]$$

$$P_2(\cos(\theta - C)) = \frac{1}{2} [3\cos^2(\theta - C) - 1]$$

A = 1.8346

 $\beta = 0.39596$

C = 0.14983

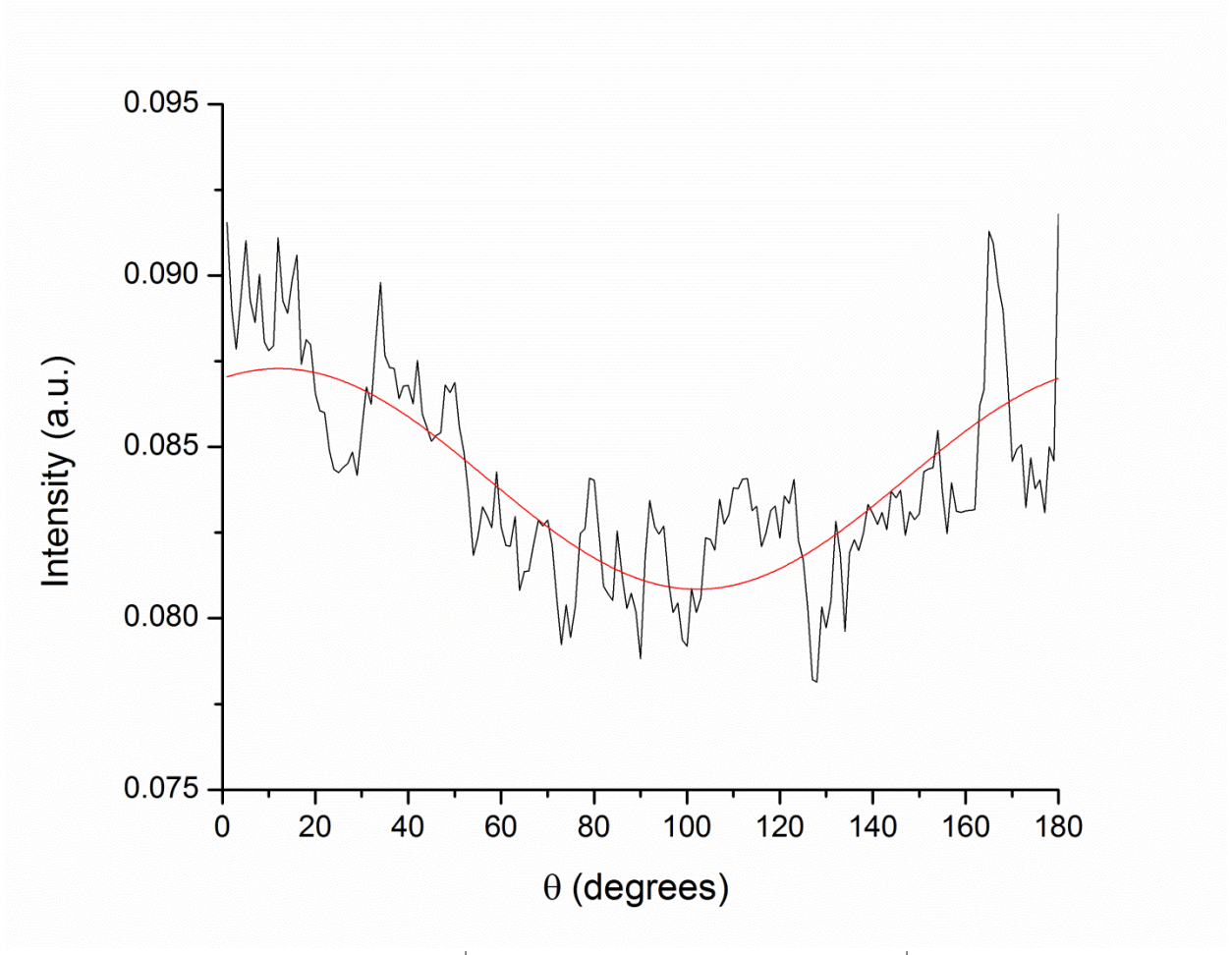


Figure 8. Angular distribution of bz^+ from photodissociation of $Ag(bz)^+$ 266 nm. The data was fit with the function below with amplitude *A* and phase shift *C*. β is the anisotropy parameter.

$$I(\theta) = \frac{A}{4\pi} [1 + \beta P_2(\cos(\theta - C))]$$

$$P_2(\cos(\theta - C)) = \frac{1}{2} [3\cos^2(\theta - C) - 1]$$

A = 1.0429

 $\beta = 0.051716$

C = 0.21235

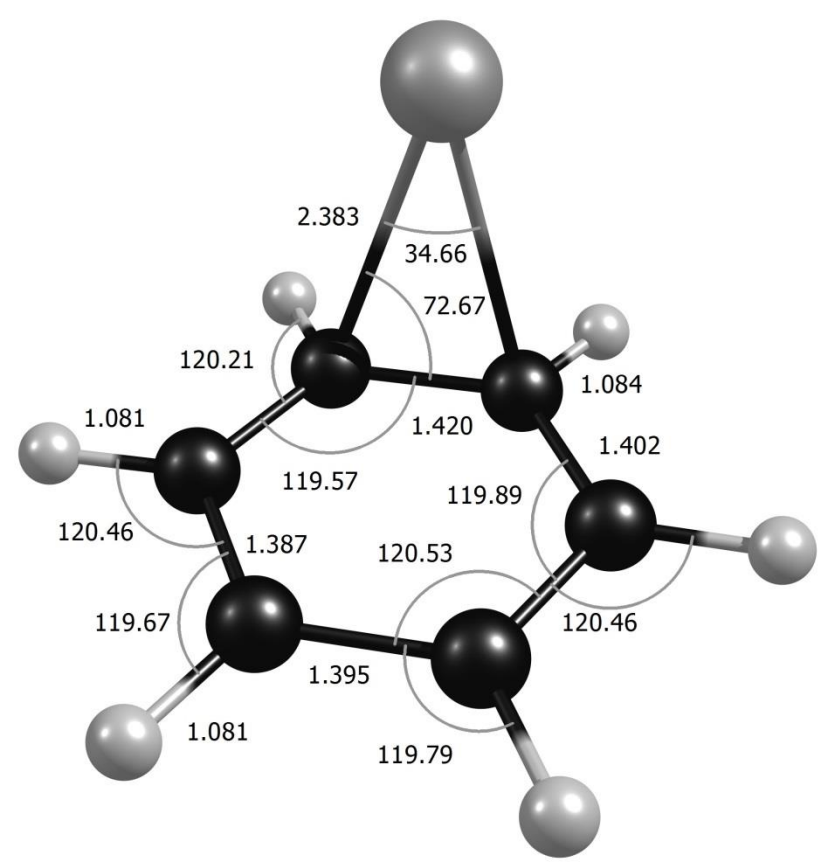


Figure 9. The optimized geometry of Ag^+ (benzene) calculated using M06-L/Def2-QZVP(Ag)/6-311++G(2d,2p)(C,H) with Gaussian 09. Bond lengths are in Angstroms and bond angles are in degrees.

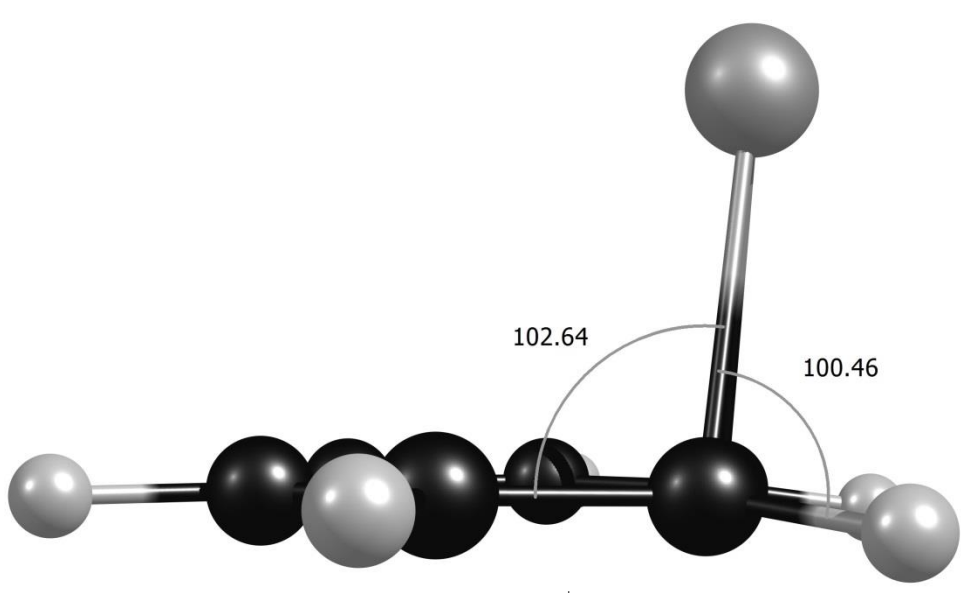


Figure 10. Side view of the optimized geometry of Ag^+ (benzene) calculated using M06-L/Def2-QZVP(Ag)/6-311++G(2d,2p)(C,H) with Gaussian 09. Bond lengths are in Angstroms and bond angles are in degrees.

The structure in Cartestion coordinates of Ag^+ (benzene) calculated using M06-L/Def2-QZVP(Ag)/6-311++G(2d,2p)(C,H) with Gaussian 09. Units are in Angstroms.

```
1
     1.182074000
                    -2.912403000
                                    1.234566000
1
     1.182074000
                    -2.912403000
                                   -1.234566000
     1.191476000
                    -0.780472000
                                   -2.483205000
1
     1.339891000
                    1.369910000
                                   -1.248752000
1
1
     1.339891000
                    1.369910000
                                   1.248752000
1
     1.191476000
                    -0.780472000
                                   2.483205000
6
     1.199221000
                    0.440209000
                                   0.709891000
6
     1.199221000
                    0.440209000
                                   -0.709891000
     1.170968000
                    -0.779177000
6
                                   1.401921000
     1.170968000
                    -0.779177000
                                   -1.401921000
6
6
     1.170968000
                    -1.973988000
                                   0.697252000
6
     1.170968000
                    -1.973988000
                                   -0.697252000
47
     -1.062144000
                     0.689391000
                                    0.000000000
```

The harmonic vibrational frequencies (unscaled, cm⁻¹) and intensities (km/mol) of Ag⁺(benzene) calculated using M06-L/Def2-QZVP(Ag)/6-311++G(2d,2p)(C,H) with Gaussian 09.

46.3 (0.1), 65.8 (0.0), 218.4 (2.9), 411.4 (0.2), 415.1 (0.3), 611.8 (0.4), 612.8 (0.1), 706.3 (0.8), 728.2 (92.7), 880.6 (1.1), 901.8 (6.5), 979.8 (3.2), 988.6 (12.0), 1003.4 (0.6), 1026.6 (0.3), 1035.5 (0.3), 1046.5 (3.4), 1055.9 (1.8), 1173.3 (0.4), 1198.6 (0.2), 1199.7 (0.0), 1363.9 (3.5), 1375.8 (0.1), 1497.8 (11.9), 1499.5 (13.1), 1603.9 (9.6), 1615.5 (4.0), 3160.5 (0.4), 3172.1 (0.8), 3180.2 (0.1), 3187.0 (0.2), 3193.4 (0.0), 3200.5 (0.0)

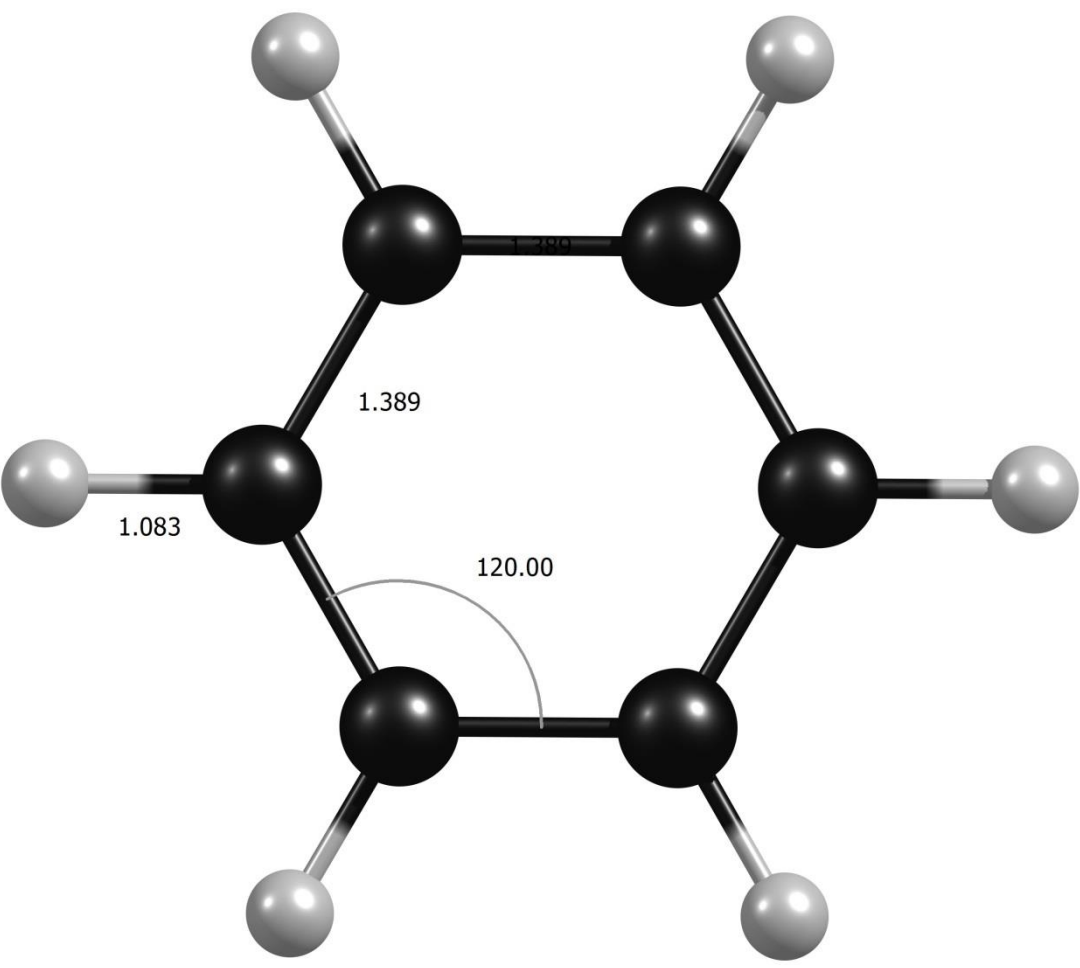


Figure 11. The optimized geometry of neutral benzene calculated using M06-L/6-311++G(2d,2p) with Gaussian 09. Bond lengths are in Angstroms and bond angles are in degrees.

The structure in Cartestion coordinates of neutral benzene calculated using M06-L/6-311++G(2d,2p) with Gaussian 09. Units are in Angstroms.

```
6
     1.374210000
                    0.203661000
                                  -0.000019000
6
     0.510756000
                    1.291815000
                                   -0.000016000
     0.863387000
                   -1.088279000
                                   -0.00005000
6
6
    -0.863388000
                    1.088278000
                                   -0.000001000
6
    -0.510756000
                    -1.291815000
                                   0.000007000
    -1.374210000
                    -0.203661000
                                   0.000008000
6
    -0.908650000
                    -2.298626000
                                   0.000049000
1
    -2.445099000
                    -0.362258000
1
                                   0.000052000
    -1.536427000
                    1.936198000
                                   0.000031000
1
1
     0.908651000
                    2.298626000
                                   0.00005000
1
     2.445099000
                    0.362259000
                                   0.00001000
1
     1.536431000
                   -1.936195000
                                   0.000023000
```

The harmonic vibrational frequencies (unscaled, cm⁻¹) and intensities (km/mol) of neutral benzene calculated using M06-L/6-311++G(2d,2p) with Gaussian 09.

409.0 (0.0), 411.9 (0.0), 619.6 (0.0), 622.3 (0.0), 685.0 (101.5), 723.2 (0.0), 859.3 (0.0), 869.7 (0.0), 985.6 (0.1), 991.2 (0.0), 1011.7 (0.0), 1013.9 (0.0), 1032.8 (0.0), 1057.3 (5.3), 1059.5 (5.0), 1169.6 (0.0), 1194.3 (0.0), 1196.8 (0.0), 1355.0 (0.0), 1377.0 (0.0), 1510.6 (4.3), 1511.9 (4.4), 1630.8 (0.0), 1635.5 (0.0), 3159.5 (0.2), 3168.5 (0.0), 3170.6 (0.0), 3184.5 (36.4), 3185.6 (35.3), 3195.1 (0.0)